



2017 | Faculty of Sciences

DOCTORAL DISSERTATION

# Low temperature deposition and characterisation of high quality nanocrystalline diamond films for the fabrication of highly sensitive pressure sensing membranes.

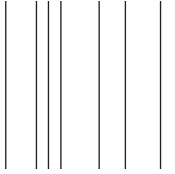
Doctoral dissertation submitted to obtain the degree of  
Doctor of Sciences: Physics, to be defended by

**Sien Drijkoningen**

Promoter: Prof. Dr Ken Haenen | UHasselt

Co-promoters: Prof. Dr Miloš Nesládek | UHasselt

Dr Stoffel Janssens | Okinawa Institute of Science and  
Technology Graduate University



D/2016/2451/56

# Dankwoord - Acknowledgements

Ik zou graag een aantal mensen bedanken die rechtstreeks en onrechtstreeks hebben bijgedragen tot het voltooiën van dit werk.

Als eerste wil ik Ken, mijn promotor, bedanken voor de kans om mijn doctoraat in zijn onderzoeksgroep te doen, maar ook voor de vele discussies en ondersteuning. Bovendien zou ik hem graag bedanken voor alle kansen die ik kreeg tijdens mijn doctoraat, o.a. als secretaresse van de Diamond Workshop SBDD, een taak die ik met veel plezier heb uitgevoerd en waaruit ik veel heb geleerd, en voor alle conferenties waar ik naartoe mocht gaan.

De volgende persoon die ik wil bedanken is zeer bepalend geweest voor het goed volbrengen van mijn doctoraat. Stoffel, bedankt om me met zoveel kunde en geduld alle kneepjes van het vak te leren. Je hebt me zoveel bijgebracht en stond altijd klaar voor een (wetenschappelijke) discussie. Succes nog met alles wat je onderneemt in Japan!

Een welgemeende bedankt is gericht aan Miloš Nesládek voor zijn expertise over het lineair antenne systeem en zijn kennis over diamantgroei en plasmakarakteristieken.

Bart Ruttens en Prof. Dr. Jan D'Haen ben ik zeer dankbaar voor de XRD-metingen en hun expertise, geduld en tips i.v.m. het gebruik van SEM.

Then I would like to thank the internal and external jury members for their efforts and input to evaluate and finalise this manuscript. In addition I

would like to thank Dr. Stuart Turner and his group, in particular Svetlana Korneychuk, at EMAT for their assistance with transmission electron microscopy measurements.

I would also like to thank Michael Liehr for all the technical and scientific support regarding the installation, use and improvements of the linear antenna system.

Furthermore I would like to thank all my non-diamond colleagues: Glen, Steven and Jeroen S. for the fun but short times in office 1.06. Evelien, Lien, Inge, Tim for always being up for some fun and/or ice cream. Ilaria, grazie mille for your efforts as my Italian "teacher". I'm also very grateful to my present and former WBGGM colleagues, Elena, Pieter, Quang, Christopher, Sankaran, Shannon, Rozita for the numerous (non)-scientific discussions and for creating and sustaining a nice working atmosphere at IMO. Paulius, thank you very much for always replying so fast to you emails, for the countless problems you helped me solve and your much appreciated expertise in optical set-ups. In addition, thanks for the numerous Raman measurements. Also a warm thanks to Giedrius and Aleksandr for the even more numerous Raman measurements. Farnoosh, thanks for always being in such a good mood and the lovely coffee breaks we had. Wim, een welgemeende dankjewel voor de leuke sfeer tijdens de eerste 2 jaren van mijn doctoraat en om altijd paraat te staan voor praktische hulp in het labo. Het ga je goed in Duitsland! Wiebke, jou bedank ik duizendmaal (en in het Nederlands ;- ) ) omdat je altijd goed gezind was, me zo vaak geholpen en tips gegeven hebt voor (niet)-wetenschappelijke kwesties. Dankjewel ook voor de vele klim- en eetavonden, de koffiepauzes en de voorbije en nog komende short-term België-Duitsland uitwisselprojecten. Voor de technische assistentie bedank ik Johan Soogen en Koen Daniëls voor hun preciezwewerk in de workshop en het helpen zoeken naar oplossingen. Dat brengt me tot misschien wel de meest geapprecieerde en de meest nodige dankjewel. Johnny, merci om altijd paraat te staan om het zoveelste euvel aan het lineair antenne systeem op te lossen en voor je immer creatieve oplossingen. Vervolgens een welgemeende bedankt Hilde

Pellaers en Christel Willems voor hun hulp in het labo, Jan Mertens voor zijn labview expertise, Lieven De Winter voor het oplossen van technische problemen en Erik Thoonen voor de PC-assistentie.

Een speciale en zeer dankbare merci is gericht aan het IMO-secretariaat voor hun hulp met de administratieve rompslomp en het verzenden van het zoveelste pakketje. Ellen, bedankt voor je hulp met de organisatie van de Diamond Workshop - SBDD en je altijd aanwezige lach!

Tot slot zou ik graag enkele mensen bedanken die me zeer dierbaar zijn. Als eerste, een dankjewel aan mijn "middelbaar"-vrienden (Natacha & Maikel, Daniëlle & Yves, Bart, Bjorn & Thomas, Pieter & Fran, Geert en vooral Karmen & Roland), voor de altijd leuke sfeer en de hulp indien nodig!

Vervolgens dankjewel aan Jeroen, mijn broer, om altijd met veel geduld klaar te staan om mijn zoveelste PC-probleem op te lossen en voor de wetenschappelijke discussies en je steun tout-court!

Mama en papa, dankjewel voor jullie onvoorwaardelijke steun en geloof in mij! Zonder jullie was dit allemaal nooit gelukt.

Lieve Stefan, dankjewel om er zo voor me zijn en me zo te steunen de laatste maanden! Ik weet dat het niet altijd even eenvoudig was!



# Publications and Conference contributions

## Publications in journals

1. T. Clukers, **S. Drijkoningen**, M. Daenen, K. Haenen, "Highly conductive boron doped nanocrystalline diamond meander structure for thermal applications", to be submitted (2017).
2. K.J. Sankaran, C.J. Yeh, **S. Drijkoningen**, P. Pobedinskas, M.K. Van Bael, K.C. Leou, I.N. Lin, K. Haenen, "Enhancement of plasma illumination characteristics of few-layer graphene-diamond nanorods hybrid", accepted Nanotechnology (2017).
3. **S. Drijkoningen**, P. Pobedinskas, Y. Balasubramaniam, S. Korneychuk, A. Momot, A. Hardy, M.K. Van Bael, S. Turner, J. Verbeeck, M. Nesládek, K. Haenen, "On the origin of diamond plates deposited at low temperature", submitted (2017).
4. D.Q. Hoang, S. Korneychuk, K.J. Sankaran, P. Pobedinskas, **S. Drijkoningen**, S. Turner, M.K. Van Bael, J. Verbeeck, S.S. Nicley, K. Haenen, "Direct nucleation of hexagonal boron nitride on diamond: Crystalline properties of hBN nanowalls", submitted Acta Materialia (2016).

5. K.J. Sankaran, D.Q. Hoang, S. Korneychuk, K. Srinivasu, J.P. Thomas, P. Pobedinskas, **S. Drijkoningen**, M.K. Van Bael, J. D'Haen, J. Verbeeck, K.C. Leou, K.T. Leung, I.N. Lin, K. Haenen, "Fabrication of hierarchical hexagonal boron nitride nanoflakes-diamond nanorods heterostructures and their enhanced field electron emission performances", RSC Advances, **6** (2016), 90338-90346.
6. K.J. Sankaran, D.Q. Hoang, K. Srinivasu, S. Korneychuk, S. Turner, **S. Drijkoningen**, P. Pobedinskas, J. Verbeeck, K.C. Leou, I.N. Lin, K. Haenen, "Engineering the interface characteristics on the enhancement of field electron emission properties of vertically aligned hexagonal boron nitride nanowalls", Physica Status Solidi (a), **213/10** (2016), 2654-2661).
7. **S. Drijkoningen**, S.D. Janssens, P. Pobedinskas, S. Koizumi, M.K. Van Bael, K. Haenen, "The pressure sensitivity of wrinkled B-doped nanocrystalline diamond membranes", Scientific Reports **6** (2016), 35667.
8. K.J. Sankaran, T.H. Chang, S.K. Bikkarolla, S.S. Roy, P. Papakonstantinou, **S. Drijkoningen**, P. Pobedinskas, M.K. Van Bael, N.H. Tai, I.N. Lin, K. Haenen, "Growth, structural and plasma illumination properties of nanocrystalline diamond decorated graphene nanoflakes", RSC Advances **6** (2016), 63178-63184.

9. K.J. Sankaran, D.Q. Hoang, S. Kunuku, S. Korneychuk, S. Turner, P. Pobedinskas, **S. Drijkoningen**, M.K. Van Bael, J. D'Haen, J. Verbeeck, K.C. Leou, I.N. Lin, K. Haenen, "Enhanced optoelectronic performances of vertically aligned hexagonal boron nitride nanowalls-nanocrystalline diamond heterostructures", *Scientific Reports* **6** (2016), 29444.
10. Z. Vlčková Živcová, O. Frank, **S. Drijkoningen**, K. Haenen, V. Mortet, L. Kavan, "n-Type phosphorus-doped nanocrystalline diamond: Electrochemical and in-situ Raman spectroelectrochemical study", *RSC Advances* **6** (2016), 51387-51393.
11. G. Degutis, P. Pobedinskas, H.-G. Boyen, W. Dexters, W. Janssen, **S. Drijkoningen**, A. Hardy, K. Haenen, M.K. Van Bael, "Improved nanodiamond seeding on chromium by surface plasma pretreatment", *Chemical Physics Letters* **640** (2015), 50-54.
12. R.L. Harniman, O.J. Fox, W. Janssen, **S. Drijkoningen**, K. Haenen, P.W. May, "Direct observation of electron emission from grain boundaries in CVD diamond by PeakForce-controlled tunnelling atomic force microscopy", *Carbon* **94** (2015), 386-395.
13. S.D. Janssens, **S. Drijkoningen**, K. Haenen, "Large time-dependent anomalous piezoresistive effect in surface conductive nanocrystalline diamond", *Applied Physics Letters* **105/11** (2014), 101601.



14. P. Cornelis, T. Vandenryt, G. Wackers, E. Kellens, P. Losada-Pérez, R. Thoelen, W. De Ceuninck, K. Eersels, **S. Drijkoningen**, K. Haenen, M. Peeters, B. van Grinsven, P. Wagner, "Heat transfer resistance as a tool to quantify hybridization efficiency of DNA on a nanocrystalline diamond surface", *Diamond and Related Materials* **48** (2014), 32-36.
15. S.D. Janssens, **S. Drijkoningen**, K. Haenen, "Ultra-thin nanocrystalline diamond membranes as pressure sensors for harsh/biological environments", *Applied Physics Letters* **104/7** (2014), 073107.
16. S.D. Janssens, **S. Drijkoningen**, M. Saitner, H.-G. Boyen, P. Wagner, K. Larsson, K. Haenen, "Phase separation of ethanol-water solutions at a hydrogen terminated nanocrystalline diamond surface", *Journal of Chemical Physics* **137/4** (2012), 044702.

#### **Publications in proceedings**

17. S.D. Janssens, **S. Drijkoningen**, M. Saitner, H.-G. Boyen, K. Haenen, P. Wagner, "The diamond-solution interface: the surface energy of hydrogen terminated nanocrystalline CVD diamond derived from contact angle measurements", *MRS Online Proceedings Library* **1362** (2011), MRSS11-1362-QQ9-47, DOI: 10.1557/opl.2011.1019.

## Awards

1. *Gold Award Winner "Young Scholar Award"* **S. Drijkoningen\***, P. Pobedinskas, M. Ficek, R. Bogdanowicz, M. Nesládek, K. Haenen, "Ultralow temperature large area diamond deposition using pulsed microwave linear antenna technology", 26th International Conference on Diamond and Carbon Materials, Maritim Hotel Bad Homburg, Bad Homburg, Germany, September 6-10, 2015.
2. *Brilliant Poster Award* **S. Drijkoningen\***, P. Pobedinskas, S. Korneychuk, S. Turner, J. Verbeeck, M. Nesládek, K. Haenen, "Low temperature deposition of diamond platelets", Hasselt Diamond Workshop 2016 - SBDD XXI, cultuurcentrum Hasselt, Hasselt, Belgium, March 9-11, 2016.
3. *Best Poster Award* **S. Drijkoningen\***, M. Nesládek, P. Pobedinskas, K. Haenen, "Ultralow temperature diamond growth with high frequency pulsed microwave linear antenna technology", 9th International Conference on New Diamond and Nano Carbons (NDNC2015), Shizuoka GRANSHIP, Shizuoka, Japan, May 24-28, 2015.

**Oral presentations**

1. **S. Drijkoningen\***, P. Pobedinskas, S. Korneychuk, S. Turner, J. D'Haen, J. Verbeeck, M. Nesládek, K. Haenen, "Low temperature deposition of diamond plates", 2016 MRS Fall Meeting, Hynes Convention Center & Sheraton Boston Hotel, Boston, MA, USA, November 27-December 2, 2016.
2. **S. Drijkoningen\***, S.D. Janssens, P. Pobedinskas, S. Koizumi, M.K. Van Bael, K. Haenen, "Piezoresistivity in Ultra-Thin Boron-Doped Diamond Membranes ", 2016 MRS Fall Meeting, Hynes Convention Center & Sheraton Boston Hotel, Boston, MA, USA, November 27-December 2, 2016.
3. *Participation on invitation:* **S. Drijkoningen\***, P. Pobedinskas, S. Korneychuk, S. Turner, J. Verbeeck, M. Nesládek, K. Haenen, "Low temperature deposition of diamond platelets", 67th Diamond Conference, University of Warwick, Warwick, UK, July 11-14, 2016.
4. **S. Drijkoningen**, S.D. Janssens, K. Haenen\*, "Piezoresistivity in ultra-thin nanocrystalline diamond membranes", 2015 MRS Fall Meeting, Hynes Convention Center & Sheraton Boston Hotel, Boston, MA, USA, November 29-December 4, 2015.
5. **S. Drijkoningen\***, P. Pobedinskas, M. Ficek, R. Bogdanowicz, M. Nesládek, K. Haenen, "Ultralow temperature large area diamond deposition using pulsed microwave linear antenna technology", 26th International Conference on Diamond and Carbon Materials, Maritim Hotel Bad Homburg, Bad Homburg, Germany, September 6-10, 2015.

6. **S. Drijkoningen\***, S.D. Janssens, K. Haenen, "Piezoresistivity in ultra-thin boron-doped and surface conductive undoped nanocrystalline diamond membranes", 9th International Conference on New Diamond and Nano Carbons (NDNC2015), Shizuoka GRANSHIP, Shizuoka, Japan, May 24-28, 2015.

**Poster presentations**

1. **S. Drijkoningen\***, P. Pobedinskas, S. Korneychuk, S. Turner, J. Verbeeck, M. Nesládek, K. Haenen, "Low temperature deposition of diamond platelets", Hasselt Diamond Workshop 2016 - SBDD XXI, cultuurcentrum Hasselt, Hasselt, Belgium, March 9-11, 2016.
2. **S. Drijkoningen\***, P. Pobedinskas, M. Ficek, R. Bogdanowicz, M. Nesládek, K. Haenen, "Ultralow temperature large area diamond deposition using pulsed microwave linear antenna technology", 26th International Conference on Diamond and Carbon Materials, Maritim Hotel Bad Homburg, Bad Homburg, Germany, September 6-10, 2015.
3. **S. Drijkoningen\***, M. Nesládek, P. Pobedinskas, K. Haenen, "Ultralow temperature diamond growth with high frequency pulsed microwave linear antenna technology", 9th International Conference on New Diamond and Nano Carbons (NDNC2015), Shizuoka GRANSHIP, Shizuoka, Japan, May 24-28, 2015.
4. **S. Drijkoningen\***, S.D. Janssens, K. Haenen, "Wrinkled B:NCD pressure sensing membranes: a mismatch in thermal expansion coefficients determines the sensitivity", Hasselt Diamond Workshop 2015 - SBDD XX, cultuurcentrum Hasselt, Hasselt, Belgium, February 25-27, 2015.
5. **S. Drijkoningen\***, M. Nesládek, P. Pobedinskas, K. Haenen, "Ultralow temperature diamond growth with high frequency pulsed microwave linear antenna technology", Hasselt Diamond Workshop 2015 - SBDD XX, cultuurcentrum Hasselt, Hasselt, Belgium, February 25-27, 2015.

# Contents

<b>Dankwoord - Acknowledgements</b>	<b>i</b>
<b>Publications and Conference contributions</b>	<b>iv</b>
<b>Glossary</b>	<b>xvii</b>
<b>Nederlandse samenvatting</b>	<b>1</b>
<b>Preface</b>	<b>5</b>
<b>I Basics</b>	<b>9</b>
<b>1 Diamond - a general introduction</b>	<b>11</b>
1.1 Diamond . . . . .	11
1.1.1 A carbon allotrope . . . . .	12
1.1.2 Diamond's properties . . . . .	15
1.2 Synthetic diamond . . . . .	15
1.2.1 HPHT . . . . .	15
1.2.2 CVD . . . . .	16
1.2.3 Detonation nanodiamond . . . . .	17
1.3 Classification of diamond . . . . .	17
1.3.1 Single crystal diamond . . . . .	17
1.3.2 Polycrystalline diamond . . . . .	19
1.4 Doping of diamond . . . . .	21

1.4.1	Surface conductivity of diamond . . . . .	21
1.4.2	p-type doping . . . . .	21
1.4.3	n-type doping . . . . .	22
<b>2</b>	<b>Diamond growth</b>	<b>27</b>
2.1	Substrate pretreatment . . . . .	27
2.1.1	Substrate cleaning . . . . .	27
2.1.2	Nanodiamond seeding . . . . .	28
2.1.3	Mechanical abrasion seeding . . . . .	28
2.1.4	Ultrasonic seeding . . . . .	29
2.1.5	Bias Enhanced Nucleation . . . . .	29
2.2	Chemical vapour deposition of diamond . . . . .	29
2.3	Resonance cavity plasma enhanced microwave systems . . . . .	33
2.4	Plasma enhanced linear antenna microwave systems . . . . .	34
2.4.1	Memory effect . . . . .	38
2.4.2	Continuous microwave mode . . . . .	39
2.4.3	Pulsed microwave mode . . . . .	41
<b>3</b>	<b>Characterisation and experimental techniques</b>	<b>47</b>
3.1	In-situ laser interferometry . . . . .	47
3.2	Optical Emission Spectroscopy . . . . .	48
3.3	Scanning Electron Microscopy . . . . .	49
3.4	Transmission Electron Microscopy . . . . .	50
3.5	X-ray Diffraction . . . . .	54
3.6	Raman Spectroscopy . . . . .	56
3.7	Surface curvature measurements . . . . .	59
<b>4</b>	<b>Diamond plates</b>	<b>61</b>
4.1	Re-entrant groove model . . . . .	63
4.2	Sub-step model . . . . .	65
4.2.1	Simulations . . . . .	68
4.3	Occurrence of stacking faults . . . . .	69

<b>II Results and discussion: Membranes</b>	<b>71</b>
<b>5 Diamond membranes on glass</b>	<b>73</b>
5.1 Fabrication of NCD membranes on glass . . . . .	74
5.2 Piezoresistive effect of NCD membranes . . . . .	76
5.2.1 Piezoresistivity of NCD:H membranes . . . . .	78
5.2.2 Piezoresistivity of B:doped NCD membranes . . . . .	83
5.3 Pressure sensitivity of wrinkled B-doped NCD membranes . .	85
5.3.1 Pressure sensitivity . . . . .	86
5.3.2 Characterisation . . . . .	95
5.4 Conclusion . . . . .	103
<b>III Results and discussion: Diamond growth based on linear antenna technology</b>	<b>105</b>
<b>6 Low temperature diamond deposition</b>	<b>107</b>
6.1 Continuous wave mode . . . . .	108
6.1.1 Influence of pressure . . . . .	109
6.1.2 Influence of gas composition . . . . .	113
6.1.3 Influence of the distance to the antennas . . . . .	117
6.1.4 Influence of power . . . . .	121
6.1.5 Influence of substrate temperature . . . . .	123
6.2 Pulsed wave mode . . . . .	127
6.3 Diamond membranes . . . . .	135
6.3.1 Stress dependence of the morphology . . . . .	138
6.4 Conclusion . . . . .	141
<b>7 Co-deposition of diamond plates and octahedral grains</b>	<b>145</b>
7.1 Characterisation . . . . .	146
7.2 Proposed mechanism for the initial stages of the development of plates . . . . .	154
7.2.1 Impurity induced formation of stacking faults . . . . .	154



7.2.2 Impurity induced blocking layer for the growth of a crystal facet . . . . .	159
7.2.3 Impurity enhanced etching of a crystal facet . . . . .	160
7.3 Conclusion . . . . .	161
<b>Conclusion and future perspectives</b>	<b>163</b>
<b>Bibliography</b>	<b>167</b>

# Glossary

a-C:H	hydrogenated amorphous carbon
AC	alternating current
AIST	National Institute of Advanced Industrial Science and Technology
B <sub>2</sub> H <sub>6</sub>	diborane
B:NCD	boron doped nanocrystalline diamond
BEN	bias enhanced nucleation
BSE	back scattered electrons
CCD	charge coupled device
CE2000	Corning Eagle 2000 glass
CH <sub>4</sub>	methane
CO <sub>2</sub>	carbon dioxide
CVD	chemical vapour deposition
CW	continuous wave
DC	direct current
DLC	diamond-like carbon
EDX	energy dispersive X-ray spectroscopy
EELS	electron energy loss spectroscopy
GeMac	Groupe d'étude de la matière condensée
H <sub>2</sub>	molecular hydrogen
HPHT	high pressure high temperature
HRTEM	high-resolution transmission electron microscopy
IMO	Institute for Materials Research
LAMWPECVD	linear antenna microwave (assisted) plasma enhanced chemical vapour deposition

MCD	microcrystalline diamond
MW	microwaves
MWPECVD	microwave (assisted) plasma enhanced chemical vapour deposition
NCD	nanocrystalline diamond
NCD-H	hydrogen terminated nanocrystalline diamond
NIMS	National Institute for Materials Science
OES	optical emission spectroscopy
OPD	optical path difference
P:NCD	phosphorus doped nanocrystalline diamond
PCD	polycrystalline diamond
PECVD	plasma enhanced chemical vapour deposition
PH <sub>3</sub>	phosphine
RCA	Radio Corporation of America
RDX	1,3,5-trinitroperhydro-1,3,5-triazine
S-AF45	Schott AF45 glass
SAD	selected area diffraction
SAED	selected area electron diffraction
SCD:H	hydrogen-terminated single crystal diamond
SEM	scanning electron microscopy
SiC	silicon carbide
SIMS	secondary ion mass spectroscopy
STEM	scanning transmission electron microscopy
TBP	tert-butylphosphine
TEM	transmission electron microscopy
TMB	trimethylboron
TMP	trimethylphosphine
TNT	trinitrotoluene
UNCD	ultrananocrystalline diamond
XRD	X-ray diffraction

# Nederlandse samenvatting

Voor het maken van werkende toestellen is er vaak een combinatie van meerdere materialen nodig. Het afzetten van een materiaal bovenop eender welk ander materiaal vereist goede adhesie, maar ook een lage stress in de afgezette laag om barsten en delaminatie te voorkomen. Het substraat is altijd verantwoordelijk voor een bepaalde hoeveelheid stress in de afgezette laag. Bij nanokristallijne diamantfilms is de meeste stress thermisch geïnduceerd door het depositieproces bij hoge temperaturen gevolgd door het afkoelen van het substraat en de diamantlaag tot kamertemperatuur. Aangezien beide materialen een verschillende thermische expansiecoëfficiënt hebben krimpt één materiaal meer dan het andere tijdens het afkoelen. Daarom kan een slimme keuze van het substraatmateriaal en afzetting bij lage temperatuur de stress in de diamantlagen minimaliseren. Bovendien worden er een aantal nieuwe toepassingen mogelijk door het afzetten van diamantfilms bij lage temperaturen ( $T < 410 \text{ }^\circ\text{C}$ ) zoals flat panel displays, plastics, etc. Om deze lage temperatuur te bereiken is een hoge plasmadichtheid nodig bij een lage gasdruk, zodat gevoelige substraten beperkt thermisch belast worden. De meest gebruikt 'resonance cavity' (lett. resonantieholt) plasma systemen werken niet binnen dit bereik van druk en plasmadichtheid, maar lineaire antenne microgolf depositiesystemen kunnen wel gebruikt worden voor afzettingen bij drukken onder 1 mbar, en op grote oppervlakken

tot 30 cm in diameter. Overigens, zou een 'bottom-up' aanpak die controle toelaat over de verkregen morfologie een pluspunt zijn voor het ontwikkelen van nanodiamant objecten of apparatuur, aangezien sommige eigenschappen van nanokristallijn diamant sterk beïnvloed worden door de kristaloriëntatie, vooral indien de stress in de afgezette laag kan gereguleerd worden door de specifieke morfologie.

Deze thesis kan in twee delen opgesplitst worden, d.w.z. het maken van hoog-sensitieve druksensors op basis van membranen enerzijds en de groei van diamantlagen van zeer hoge kwaliteit met technologie gebaseerd op lineaire antennes anderzijds.

Na een algemene inleiding tot diamant in hoofdstuk 1, worden in hoofdstuk 2 de depositietechnieken beschreven met de nadruk op de technologie gebaseerd op lineaire antennes.

In hoofdstuk 3 volgt een beschrijving van de karakterisatietechnieken (In-situ laser interferometrie, optische emissie spectroscopie, scanning and transmissie electron microscopie, X-ray diffractie, electron energy loss spectroscopie, Raman spectroscopie en oppervlaktekrommingsmetingen) gebruikt voor deze thesis.

In hoofdstuk 4 ligt de focus op een literatuurstudie met betrekking tot de diamantplaatjesstructuren.

Het piezoresistieve effect van boor-gedoteerde en oppervlakte-geleidende diamantfilms wordt beschreven in hoofdstuk 5, samen met een studie naar de gevoeligheid van druksensoren op basis van diamantmembranen. Intrinsieke laageigenschappen zoals korrelgrootte, doteerniveau en specifieke morfologie hebben een invloed op de afgezette laag. Bovendien kan er voor nanokristallijne diamantfilms een groot deel van de stress toegeschreven worden aan de mismatch in thermische expansiecoëfficiënt tussen het substraat en de diamantlaag. Het substraat induceert een bepaalde hoeveelheid stress die relaxeert door het ontstaan van rimpels wanneer het substraat gedeeltelijk wordt weggeëet. De oorspronkelijke hoeveelheid stress heeft een duidelijke impact op het aantal en de lengte

van de rimpels.

Hoofdstuk 6 focust op de optimalisatie van de depositieparameters voor de groei van kwaliteitsdiamant met behulp van lineaire antenne technologie. De invloed van de druk, gassamenstelling, afstand tot de antennes, vermogen en substraattemperatuur wordt besproken. Hoewel het pulsen van de microgolven theoretisch gezien veel potentiëel heeft, is er op experimenteel vlak nog optimalisatie nodig.

Tot slot wordt in hoofdstuk 7 de bijzondere morfologie, d.w.z. co-depositie van plaatjes en octahedrische korrels, verkregen voor lagen met hoge kwaliteit in detail geanalyseerd en een groeimodel wordt voorgesteld op basis van aanwezige vreemde materialen.



# Preface

For the realization of working devices, often a stack of material layers is necessary. The deposition of any material on top of any other material requires good adhesion, but also a low amount of stress in the deposited layer to avoid cracking and delamination. The substrate always causes a certain amount of stress in any layer deposited on top. For the deposition of nanocrystalline diamond layers, most of the stress is thermal stress due to the growth at elevated temperatures and cooling the substrate and the diamond layer down to room temperature. Because both materials have a different thermal expansion coefficient, one material will shrink more upon cooling down. Therefore a clever choice of the substrate material and deposition at low temperatures can minimize the stress in the diamond layers. In addition, the preparation of diamond thin films at low temperatures ( $T < 410\text{ }^{\circ}\text{C}$ ) enables a wide range of novel applications, including deposition on flat panel displays, plastics, etc. To reach these conditions, high plasma densities are necessary at low gas pressures, which leads to a low thermal load onto sensitive substrate materials. The common resonance cavity plasma systems are not operable in these conditions. Linear antenna microwave delivery systems, however, can be used for depositions at pressures below 1 mbar, and on large surfaces up to 30 cm in diameter. Moreover, for the development of nanodiamond structures or devices, a bottom-up approach that allows control over the obtained morphology would be highly valuable since for nanocrystalline diamond, some properties are influenced tremendously by the crystallographic orientation. Es-



pecially, in the case where the specific morphology provides more control over the stress in the deposited layer.

This thesis can be divided into two major parts, i.e. the fabrication of highly sensitive pressure sensing membranes and the growth of high quality diamond layers with linear antenna based technology.

After a general introduction about diamond in chapter 1, chapter 2 summarises the fabrication methods with an emphasis on chemical vapour deposition systems, and in particular, technology based on linear antenna microwave applicators.

In chapter 3, the characterisation techniques, including In-situ laser interferometry, optical emission spectroscopy, scanning and transmission electron microscopy, X-ray diffraction, electron energy loss spectroscopy, Raman spectroscopy and surface curvature measurements, used in this thesis are described.

Chapter 4 focuses on literature reports concerning the diamond plate structure.

The piezoresistive effect of boron-doped and surface conductive hydrogen-terminated diamond films is described in chapter 5, together with a study on the sensitivity of fabricated pressure sensing membranes. Intrinsic layer properties such as grain size, dopant level and morphology have an influence on the stress in the deposited layer. In addition, for nanocrystalline diamond films a great deal of the stress can be attributed to a mismatch in thermal expansion coefficients between the substrate and the diamond layer. The substrate material induces a certain amount of stress, which is released by the emergence of wrinkles when the substrate is etched to form a membrane. The initial amount of stress has a clear impact on the number and length of the wrinkles.

Chapter 6 focuses on the optimisation of the deposition parameters for high quality diamond growth with linear antenna technology. The influence of pressure, gas composition, the distance to the antennas, power and substrate temperature is discussed. Although pulsing of the microwaves

is very promising theoretically, experimentally optimisation is still necessary.

Finally in chapter 7, the growth film morphology, i.e. co-deposition of plates and octahedral grains, obtained for high quality layers is analysed in detail and a growth model, based on the presence of foreign material, is proposed.



# **Part I**

# **Basics**



# Chapter 1

## Diamond - a general introduction

*Diamonds are forever - Bond movie (1971)*

### 1.1 Diamond

Most natural diamonds are formed inside the earth at high temperatures and pressures, leading to very strong covalent bonds in a tetrahedral arrangement of atoms. This crystal structure ensures diamond is the hardest natural material, a property already known by the ancient Greeks and responsible for its name 'adámas', meaning unbreakable, indestructible. However, contrary to what the Bond movie title suggests, diamond is actually a metastable allotrope of carbon. The rareness and brilliance of diamond, due to its transparency, high refractive index and large colour dispersion, are responsible for its reputation of being 'a girl's best friend' as a precious gem stone.

### 1.1.1 A carbon allotrope

Carbon is present in a seemingly infinite number of molecular compounds due to its valency and abundance. All possible carbon bonds, however can be divided into three categories based on their hybridisation,  $sp^3$  (e.g. methane),  $sp^2$  (e.g. ethene) and  $sp$  (e.g. carbon dioxide). In the ground state, the electron configuration of carbon is  $1s^2 2s^2 2p^2$ . This means that in the outer shell the s-orbital (2s) is completely filled, while the  $p_x$  and  $p_y$  orbitals both contain one electron and the  $p_z$  orbital is empty. Upon bonding these atomic orbitals mix to form molecular orbitals, a process that is called hybridisation. This hybridisation is described in figure 1.1. For  $sp^2$  orbitals for instance, two of the three available p orbitals combine with the s orbital to form three  $sp^2$  orbitals, while the third p orbital remains unhybridised. The combination of three  $sp^2$  orbitals and one p orbital is summarised as  $sp^2$  hybridisation. In this configuration the  $sp^2$  orbitals form  $\sigma$  bonds leading to bonding angles of  $120^\circ$ , while the p orbitals form  $\pi$  bonds (double bonds).

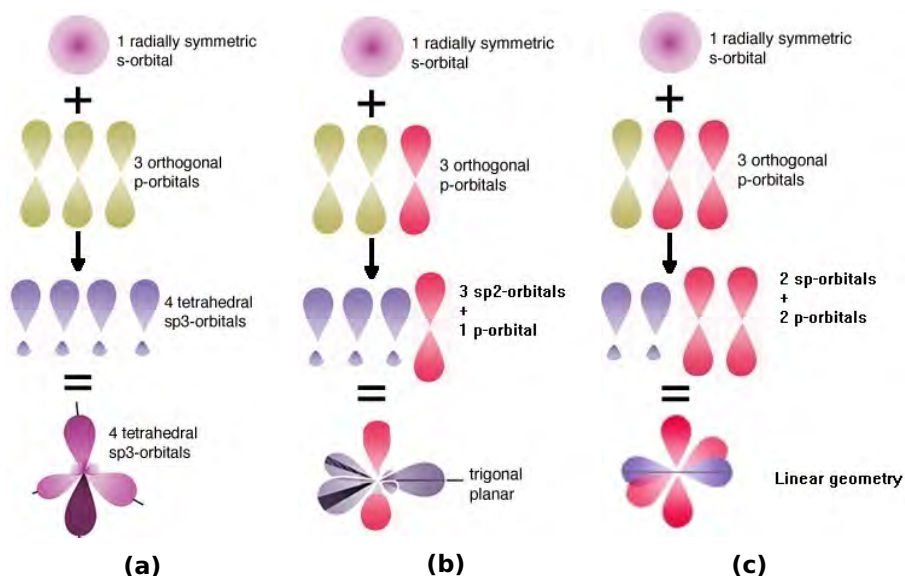


**Figure 1.1:** a)  $sp^3$ , b)  $sp^2$  and c)  $sp$  hybridisation.<sup>[1]</sup>

For carbon allotropes, there are many possibilities, since carbon is a Group IV element, i.e. containing four valence electrons. Potential  $sp$  allotropes are limited to the linear acetylenic carbon family  $(-C\equiv C-)_n$ , with  $n$  between 1 and infinity. A selection of commonly known carbon allotropes with  $sp^3$  and  $sp^2$  hybridised atomic configurations is depicted in figure 1.3.

Diamond and lonsdaleite are the only fully  $sp^3$  hybridised carbon allotropes. In diamond the bonding angle is  $109^\circ 28'$ , i.e. the carbon atoms have a tetrahedral arrangement with a bond length of 0.154 nm and a lattice constant of 0.356 nm. The density of carbon atoms is  $1.763 \cdot 10^{23} \text{ cm}^{-3}$ . In lonsdaleite, or hexagonal diamond, the carbon atoms are arranged in a hexagonal lattice, as compared to a cubic lattice for diamond. This means that in lonsdaleite some of the six-membered rings are in the boat-conformation, whereas for cubic diamond all rings are in the chair conformation (figure 1.2).

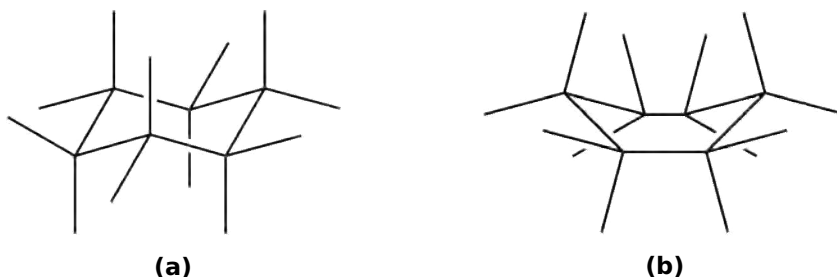


**Figure 1.2:** a) Chair conformation and b) boat conformation. The chair conformation is energetically more favourable and thus more likely to be formed.

The cubic structure is dominant, since the chair conformation is energetically slightly more favourable in the temperature and pressure regime in which diamond forms in the Earth. For  $sp^2$  hybridisation there are plenty of possibilities. The easiest way to discuss all  $sp^2$  allotropes is to start from graphene as a building block. Graphene is single sheet of  $sp^2$  hybridised carbon atoms each containing three  $\sigma$  and one  $\pi$  bond, which leads to a planar hexagonal lattice. When these graphene sheets are stacked with a interplanar distance of 0.335 nm it forms graphite. If a sheet of graphene is rolled and two of its edges bond, a singled walled carbon nanotube



is formed. If graphene bonds to form a closed hollow sphere or tube, a fullerene is created. Amorphous carbon is an allotrope in which both  $sp^3$  and  $sp^2$  hybridisation takes place. Amorphous carbon with a substantial amount of  $sp^3$  bonding is called diamond-like carbon (DLC).

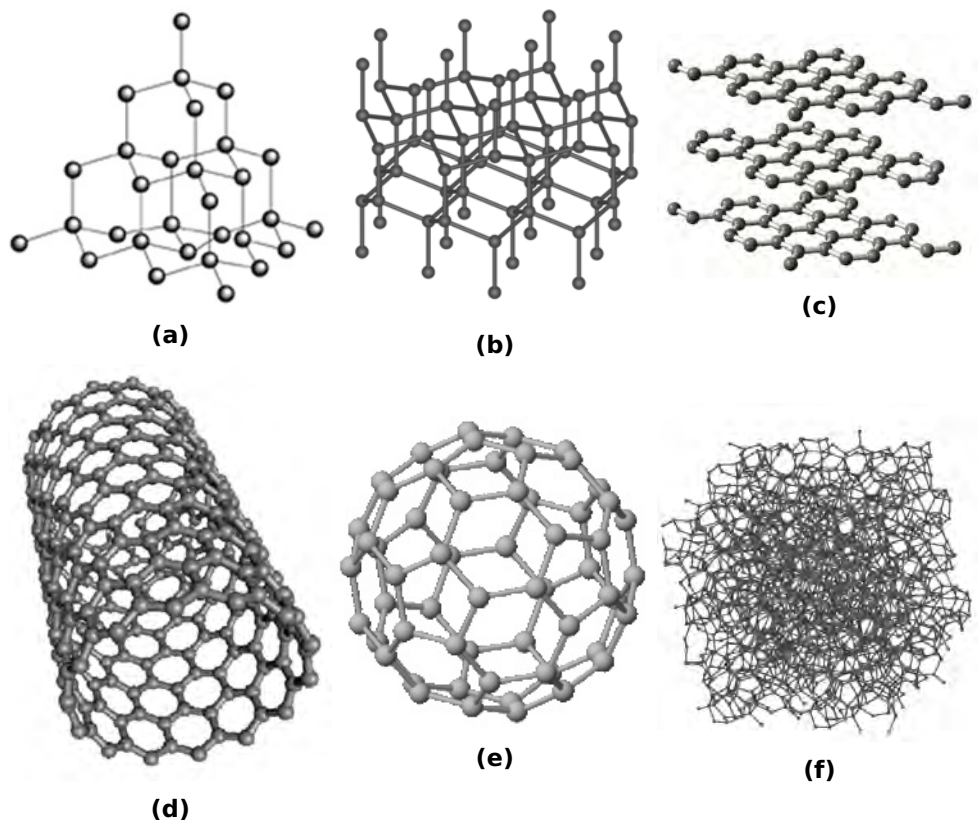


**Figure 1.3:** Atomic representation of a selection of carbon allotropes. a) Diamond<sup>[2]</sup>, b) lonsdaleite<sup>[3]</sup>, c) graphite<sup>[4]</sup>, d) carbon nanotube<sup>[5]</sup>, e) fullerene ( $C_{60}$ )<sup>[6]</sup>, f) amorphous carbon<sup>[7]</sup>.

## 1.1.2 Diamond's properties

**Table 1.1:** Overview of some properties of diamond.<sup>[8-10]</sup>

Properties	Approximate value at 300K
Hardness (GPa)	98
Density ( $\text{g} \cdot \text{cm}^{-3}$ )	3.52
Linear thermal expansion coefficient ( $10^{-6} \cdot ^\circ\text{C}^{-1}$ )	1.1
Band gap (eV)	5.45
Resistivity ( $10^{18} \Omega \cdot \text{m}$ )	1.0
Refractive index	2.44
Thermal conductivity ( $\text{W} \cdot \text{cm}^{-1} \cdot \text{K}^{-1}$ )	20

## 1.2 Synthetic diamond

### 1.2.1 HPHT

Since natural diamond is known as a rare and precious material, there has been, and still is, an interest in artificial diamond. After Lavoisier and Tennant showed that diamond was composed out of only carbon, many attempts to make diamond were carried out in the beginning of the 20<sup>th</sup> century, by pressurising graphite or other carbon sources at high temperatures.<sup>[11]</sup> The first actual report of reproducible synthetic diamond was made in 1955 by the General Electric Company in New York.<sup>[12]</sup> By heating carbon to maximum temperatures of 3000 °C at estimated maximum pressures of 98 kbar (=9.8 GPa), diamond crystals were formed reproducibly. This technique was later named "high pressure high temperature" (HPHT). HPHT diamond synthesis is typically carried out in presence of a catalyst, such as Fe, Co, Ni or a Fe-alloy, and at temperatures and pressures of about of 1400 °C and 55 kbar (= 5.5 GPa) since at these conditions diamond is thermodynamically the most stable form. Most HPHT diamonds are yellow because of nitrogen impurities, and contain other impurities inherent to the fabrication process. Therefore, another popular technique that has been developed for diamond synthesis is chemical

vapour deposition (CVD), which allows the growth of very pure diamond crystals. Additionally, this technique allows growth at lower pressures and temperatures than those required for HPHT synthesis. Bundy was the first to report the phase diagram of carbon, which shows the different conditions under which diamond can be formed, i.e. HPHT vs. CVD, as shown in figure 1.4.<sup>[13]</sup> Moreover the diagram clearly shows that under ambient conditions, diamond is a metastable form while graphite is thermodynamically stable.

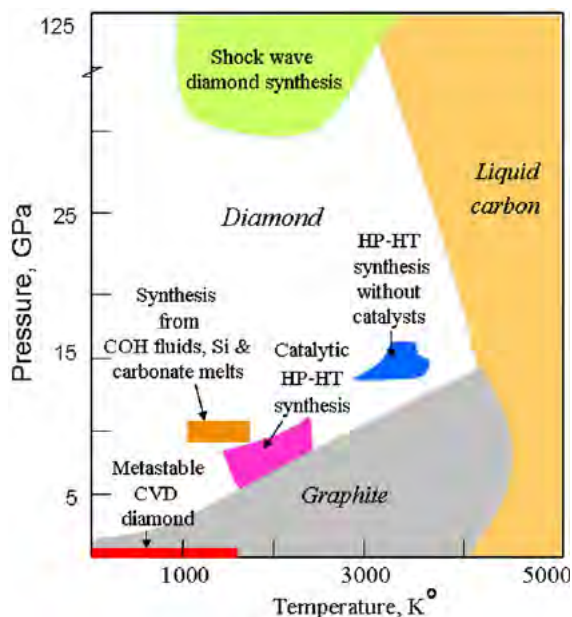


**Figure 1.4:** The phase diagram of carbon published first by Bundy and adapted by an additional field of diamond synthesis from C-O-H fluids and Si and carbonate melts (data adopted from<sup>[14-25]</sup>) [copied from<sup>[26]</sup>.]

### 1.2.2 CVD

In 1952 and 1968 the first CVD diamond was produced by William Eversole and Derjaguin et al respectively.<sup>[27,28]</sup> The growth rate in these experiments was low, however, and graphite was being co-deposited. As a consequence, preferential etching of graphitic phases, compared to diamond, by the presence of atomic hydrogen was a major breakthrough.<sup>[29]</sup>

Russian scientists later showed the CVD process was useful for diamond growth on non-diamond substrates.<sup>[30]</sup> In the eighties the Japanese National Institute for Research in Inorganic Materials (NIRIM), now known as National Institute for Materials Science (NIMS), further optimised the CVD growth by the design of both a hot filament reactor and a microwave plasma reactor.<sup>[31-34]</sup> The chemical vapour deposition process for the production of synthetic diamond is explained in detail in chapter 2.

### **1.2.3 Detonation nanodiamond**

Detonation nanodiamond is created when an oxygen deficient mixture containing two explosives, i.e. 1,3,5-Trinitroperhydro-1,3,5-triazine (RDX) and Trinitrotoluene (TNT), is detonated in a closed chamber. During this process high pressures and temperatures mimic the conditions under which natural diamond is formed. After synthesis the soot is removed by oxidative treatment and the diamond particles are bead milled to de-aggregate them into separate particles with grain sizes as small as 5 nm. The detonation diamond powder is commercially available and is often used for the seeding of non-diamond surfaces in the form of a suspension. (More details on the seeding procedure can be found in section 2.1.2.) The surface of the diamond particles is oxygen terminated, e.g. carboxylic and alcohol groups, due to the nature of the fabrication process, which ensures a stable suspension in water with a zeta potential of  $(45 \pm 5)$  mV.

## **1.3 Classification of diamond**

### **1.3.1 Single crystal diamond**

Diamond can be categorised into class I and class II, based on its impurity level. Class I contains detectable levels of nitrogen, by infrared transmission spectroscopy, and class II does not. But the classification has to be considered with care since multiple types can coexist within a single dia-

mond stone.

Class I is the most common class of natural diamonds and it can be divided into type Ia and Ib. In type Ia (about 98% of all natural diamonds) the nitrogen atoms are clustered, while in type Ib the nitrogen impurities are interstitial and more diffuse. While type Ib is rare in nature, most HPHT diamonds can be categorised in this type. Because of the nitrogen content, diamonds of class I are yellow.

Class II diamonds were formed under extremely high pressure for longer time periods and they don't contain any measurable level of nitrogen impurities. Type IIa is the most pure form of diamond due to the absence of impurities by infrared spectroscopy. Type IIa diamonds can still be coloured however, due to crystal imperfections. These imperfections can be repaired via a HPHT treatment, which can make them transparent. Although type IIa is the most pure form, type IIb is considered to be more valuable. Type IIb diamond is very rare, only 0.1% of all natural diamonds. Even though no nitrogen impurities are present, it contains boron impurities, leading to a blue colour. The most famous rock of this type is the Hope diamond (figure 1.5).



**Figure 1.5:** The Hope diamond. Its natural blue colour originates from boron impurities.<sup>[35]</sup>

In CVD, single crystal diamonds are either formed homoepitaxially on a single crystal diamond substrate, or heteroepitaxially on a substrate with a similar lattice constant as diamond, e.g. Iridium with a lattice constant of 0.384 nm.<sup>[36]</sup> For heteroepitaxial diamond deposition a nucleation step is required and the resulting quality is considerably less than that of homoepitaxial diamond.

### **1.3.2 Polycrystalline diamond**

CVD diamond deposition on non-diamond substrates with very different lattice constants typically leads to polycrystalline diamond films. This is the generic term for all types of diamond that consist of multiple grains connected via grain boundaries. The diamond grains consist of  $sp^3$ -bonded carbon, as discussed before, but the grain boundaries are a mixture of  $sp^2$ -containing allotropes, i.e. graphitic layers and amorphous carbon. By careful selection of the growth parameters, both the orientation, determined by the alpha parameter (see chapter 4 for more details), and the size of the grains can be tuned. Depending on the size of the individual diamond grains and the resulting amount of grain boundaries, polycrystalline films are often divided into three categories. In literature these terms are often intermixed, but for this thesis we will use the following definitions, as shown in figure 1.6.<sup>[37,38]</sup>

#### **Microcrystalline diamond**

Microcrystalline diamond (MCD) is a polycrystalline diamond form with grain sizes typically larger than 500 nm, as shown in figure 1.6a.<sup>[37]</sup> MCD is usually formed in hydrogen-rich environments with low methane concentrations.

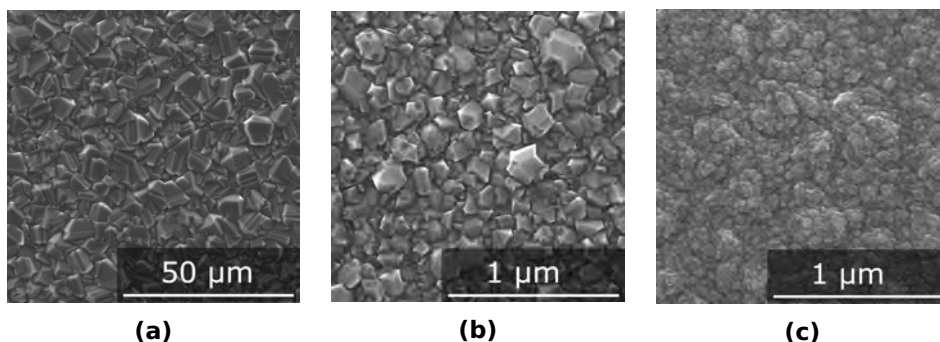


**Figure 1.6:** Scanning Electron Micrographs of a) microcrystalline diamond with a typical grain size larger than 500 nm, b) nanocrystalline diamond with grain sizes between few tens of nanometres up to 500 nm and a distinct crystalline character, and c) ultrananocrystalline diamond with typical grain sizes below ten nanometre. All three samples were deposited with an ASTeX 6500 reactor (see section 2.3).

### Nanocrystalline diamond

Nanocrystalline diamond (NCD) films have grain sizes ranging from a few tens of nanometres up to 500 nm, with a distinct crystalline character in the lower range in contrast to ultrananocrystalline diamond (UNCD). An example of NCD is shown in figure 1.6b. Both MCD and NCD processes use the same type of chemistry and show the same morphology. After short deposition runs NCD is formed but if the deposition continues the grain size increases, evolving into MCD. The exact orientation of the grains depends on the growth parameters both for MCD and NCD.

### Ultrananocrystalline diamond

In UNCD the grains are less well defined, with a more cauliflower like appearance, as shown in figure 1.6c.<sup>[39]</sup> UNCD films are grown in processes with a high degree of renucleation, which leads to small grain sizes and a high grain boundary density. The  $sp^2$  content is higher for these films compared to nanocrystalline films. Typical grain sizes are below 10 nm. Renucleation can be induced for instance by a high carbon concentration, the presence of Ar in the gas mixture, or deposition at low temperature. The key feature is that the evolution of growth is suppressed by the contin-

uous introduction of new nucleation sites. As a consequence UNCD films are generally very smooth.

## **1.4 Doping of diamond**

### **1.4.1 Surface conductivity of diamond**

Hydrogen-terminated diamond exhibits surface conductivity which can be described by a transfer doping mechanism.<sup>[40]</sup> The hydrogen-terminated surface is responsible for a negative electron affinity and the difference in electronegativity between carbon and hydrogen leads to a surface dipole. Molecules from the air can adsorb onto this surface and accept electrons from the bulk, leading to the creation of holes, i.e. lack of electrons, just below the surface. This 2-dimensional hole-gas layer allows charges to be transported and gives rise to p-type surface conductivity.<sup>[41]</sup>

### **1.4.2 p-type doping**

Intrinsic diamond is a wide bandgap semiconductor, i.e. 5.45 eV at room temperature, that can be doped with elements with a different number of valence electrons than carbon. As carbon is a group IV element, group III elements, such as boron, have one fewer electron, resulting in p-type material, and group V elements, such as phosphorus, have one more electron, resulting in n-type material. Most synthetic doped diamonds mimic those found in nature, e.g. the Hope diamond, shown in (figure 1.5) by using boron (B) as a dopant atom (group III). Boron incorporates substitutionally into the diamond lattice,<sup>[42]</sup> and induces an acceptor level at 0.368 eV above the valence band, therefore it is a p-type dopant.<sup>[43]</sup>

Both single crystal and polycrystalline diamond can be doped, but the incorporation level depends on the crystal orientation; typically the incorporation rate is the highest in (111)-oriented surfaces.<sup>[44–46]</sup> The most commonly used precursor gasses are trimethylboron (TMB) ( $C_3H_9B$ ) and



diborane ( $B_2H_6$ ). At low doping levels, diamond acts as an extrinsic semiconductor. At high doping levels the material acts as a semimetal; i.e. the metal to insulator or Mott transition, takes place between  $4.0$  and  $4.8 \cdot 10^{20} \text{ cm}^{-3}$ .<sup>[47]</sup> For boron concentrations higher than  $4\text{-}5 \cdot 10^{21} \text{ cm}^{-3}$ , diamond shows superconducting behaviour near  $4\text{K}$ .<sup>[48]</sup> Via elemental mapping in spatially resolved EELS (electron energy loss spectroscopy) experiments, Turner *et al.* showed that there is no preferential embedding of B in the grain boundaries between the NCD grains.<sup>[42]</sup> These results were in contrast with previous results on polycrystalline B-doped diamond films.<sup>[49]</sup> Moreover it was shown that the B atoms present in the diamond grains are incorporated substitutionally.<sup>[42]</sup>

### 1.4.3 n-type doping

#### Nitrogen

While p-type doping easily shows high incorporation levels, efficient n-type doping still remains a challenging task. Up to now there haven't been any reports of a donor that creates an energy level that is shallow enough to be sufficiently ionised at room temperature to show electrical conductivity. The only known n-type impurity to incorporate in natural diamond is nitrogen, which induces a deep donor level at  $1.7 \text{ eV}$  below the conduction band. Although N-doped diamond might not be conductive it is of interest in quantum applications, which is outside the scope of this thesis.<sup>[50]</sup>

#### Phosphorus

The only n-type dopant that has been reported to show n-type conductivity is phosphorus. Typical precursors are trimethylphosphine (TMP) ( $C_3H_9P$ ), tert-butylphosphine (TBP) ( $[(CH_3)_3C]_3P$ ) and phosphine ( $PH_3$ ), of which the latter is highly toxic. Unlike boron ( $r_B = 87 \text{ pm}$ ) and nitrogen ( $r_N = 75 \text{ pm}$ ) which incorporate easily into the diamond lattice because of similar radii

compared to carbon ( $r_C = 77$  pm), phosphorus ( $r_P = 110$  pm) induces a lattice distortion upon incorporation, which influences the donor activation energy. Theoretically, this level is calculated to be 0.2 - 0.27 eV,<sup>[51,52]</sup> experimentally however it is confirmed to be at 0.56 eV because of lattice distortions. The first successful P-doping of diamond was reported by Koizumi *et al.* at NIMS.<sup>[53]</sup> With  $\text{PH}_3$  as the dopant source, they deposited a CVD film onto a (111)-oriented HPHT substrate and Hall measurements proved n-type conductivity. After this first success a lot of effort was devoted by other groups to reproduce these findings and similar results were obtained at AIST, Néel, IMO and GeMac.<sup>[54-57]</sup> The doping efficiency is higher for (111) crystals than for (100) surfaces, so optimisation was needed before efficient doping of the latter substrates was obtained. The first n-type conductivity on (100)-oriented substrates was reported by Kato *et al.* in 2005 with an incorporation efficiency of about 0.02%, which is two-orders of magnitude lower than for (111) surfaces.<sup>[58-60]</sup> Phosphorus doping is typically performed at high deposition temperatures, around 850 - 950 °C. The main difference in growth parameters is the methane concentration. For efficient doping of (111) surfaces typically very low concentrations are used, i.e. < 0.15%, while for (100) facets concentrations around 1% are more commonly used, but with much higher P/C ratios. Only at AIST very low concentrations between 0.1 and 1 % have shown to be efficient for phosphorus doping of (100) single crystals.<sup>[58]</sup> Despite the fact that high incorporation levels have been achieved, the electrical conductivity remains low. A possible explanation is the co-incorporation of hydrogen atoms which can passivate phosphorus atoms.<sup>[52]</sup> Even if the incorporation and electrical conductivity can be optimised it is very unlikely for P-doped polycrystalline diamonds films to be used in electrical devices, due to issues with the electron mobility in polycrystalline materials. The grain boundaries and crystalline defects have a detrimental impact on the charge carrier mobility. The hole mobility of boron-doped diamond, for instance, has been shown to decrease with increasing amount of grain boundaries at higher C/H ratios.<sup>[61]</sup> Nevertheless, there is an in-

terest in P-doping of diamond films because of their emissive properties - hydrogen-terminated P-doped diamond films show promising characteristics for thermionic emitter applications.<sup>[62]</sup> Phosphorus doping of polycrystalline diamond remains a challenging task, however, with a very limited number of successful reports to-date.<sup>[63-69]</sup> The first successful experiments used a buffer layer growth strategy in which an undoped polycrystalline layer was deposited onto a silicon substrate, and overgrown with a P-doped diamond layer after polishing.<sup>[63]</sup> A recent report showed a large improvement in the P-incorporation efficiency by a modulation of the reactor chamber due to an increase in gas flow focused towards the substrate.<sup>[68]</sup> The growth of polycrystalline P-doped layers on non-diamond surfaces is only done by a limited number of research groups. In the first report by Schauer *et al.* P-doped polycrystalline layers on Si substrates were compared to single crystal P-doped diamond and the P-incorporation seemed to be higher in polycrystalline diamond due to a preferential P-incorporation in grain boundaries.<sup>[64]</sup> In 1995, a thorough investigation of the influence of P-doping on the morphology, growth rate, growth orientation, film quality and homogeneity was performed by Bohr *et al.*<sup>[65]</sup> Ghodbane *et al.* showed that the incorporation of phosphorus into polycrystalline diamond on Si is more efficient in {111} than in {100} facets even within one grain.<sup>[66]</sup> Recently, research performed at IMO proved phosphorus is incorporated at substitutional donor sites.<sup>[67]</sup> Additionally, contrary to the results of Schauer *et al.*, fully developed grains seem to show an enhanced P content as determined by secondary ion mass spectroscopy (SIMS) and EDX. Electrochemical characterisation (Mott-Schottky plot) has confirmed n-type doping of P-NCD with a donor concentration of  $1.8 \cdot 10^{18} \text{ cm}^{-3}$  at a nominal total phosphorus content of  $7.5 \cdot 10^{18} \text{ cm}^{-3}$ .<sup>[69]</sup>

### **Other dopants**

In consideration of other potential donors like Li, Na, S,... some theoretical calculations have been performed to determine the donor energy level.

One issue is that for some potential donors no gaseous trimethyl precursors are available, which means other experimental routes need to be developed. For Li and As experimental results have been reported though, but for none of the potential dopant atoms electrical conduction was reported unambiguously.<sup>[70,71]</sup> For arsenic, for instance, both in-situ doping and ion implantation were successful, and although no n-type conductivity could be measured the donor level was determined to be at 0.41 eV from bound excitons in ion-implanted diamond.<sup>[72,73]</sup> For lithium, in-diffusion of Li from a Li<sub>2</sub>O pellet into SCD has been reported.<sup>[74]</sup> But even though concentrations up to  $8 \cdot 10^{21} \text{ cm}^{-3}$  close to the surface and  $1 \cdot 10^{19} \text{ cm}^{-3}$  at 0.5  $\mu\text{m}$  beneath the diamond surface were found, no electrical activity could be measured.



# Chapter 2

## Diamond growth

### 2.1 Substrate pretreatment

A non-diamond substrate needs pretreatment before diamond growth, unless it is sufficiently rough and spontaneous nucleation occurs.<sup>[75]</sup> The substrates used in this thesis research are  $1 \times 1 \text{ cm}^2$  Si (100), 10-20 k $\Omega$ , Schott AF45 glass (S-AF45) and Corning Eagle 2000 glass (CE2000) and 6 inch Si wafers with 1  $\mu\text{m}$  of  $\text{SiO}_2$ , obtained by thermal oxidation of Si, on top.

#### 2.1.1 Substrate cleaning

Prior to seeding, the samples are cleaned with standard RCA-1 and RCA-2 cleaning procedures to remove organic residues and metal ions from the substrate surface respectively.<sup>[76]</sup> In the first RCA-1 cleaning step a mixture of  $\text{H}_2\text{O}$  and  $\text{NH}_4\text{OH}$  (5:1) is heated to about 80 °C after which  $\text{H}_2\text{O}_2$  (1 part) is added. The samples are immersed in this solution for ten minutes, and then rinsed thoroughly with deionised water. For the second cleaning step (1 part of)  $\text{H}_2\text{O}_2$  is added to a mixture (6:1) of  $\text{H}_2\text{O}$  and  $\text{HCl}$  at 80 °C, after which the samples are added. After ten minutes the samples are rinsed with deionised water and dried with a nitrogen gun.

### **2.1.2 Nanodiamond seeding**

At the Institute for Materials Research (IMO), non-diamond substrates are seeded with a water-based colloidal suspension of ultradispersed detonation diamond via drop casting and subsequent spin-drying.<sup>[77]</sup> The samples are spinned at 4000 rpm for 40s with a WS-400B-6NPP/LITE (Laurell technologies corporation) spin coater: during the first 20s they are continuously rinsed with deionised water and during the last 20s they are allowed to dry. The seeding is necessary to create nucleation sites and to grow a uniform and smooth film. The colloidal suspension of nanodiamonds is achieved through wet milling of the nanodiamond agglutinates with zirconia micro-beads which leads to the disintegration of the nanodiamond agglutinates by brute force. After removal of the zirconia beads by wet sieving of the obtained slurry, the nanodiamond is re-dissolved in water, centrifuged, sonicated and filtered to give a stable colloidal suspension and then the solution is mainly evaporated. The resulting flakes are pulverised, suspended in water and subjected to sonication. This colloidal suspension is further diluted and used for seeding.<sup>[78]</sup> In our lab, only the sonication and dilution are done, while the other steps are carried out by commercial powder suppliers or by collaborators. The suspension of detonation nanodiamonds from NanoCarbon Institute Co., Ltd., features a zeta potential of  $(45 \pm 5)$  mV and contains particles with a size of 6-7 nm and is diluted to a concentration of 0.33 g/l.

### **2.1.3 Mechanical abrasion seeding**

Another possible pretreatment technique is based on scratching of the substrate with diamond powder. The scratching induces defects, which are preferred nucleation spots. In addition, small residual diamond particles become embedded in the substrate surface which facilitates the nucleation process.<sup>[38]</sup>

### **2.1.4 Ultrasonic seeding**

During ultrasonic seeding the substrate is immersed in a slurry containing diamond nanoparticles and similar to mechanical abrasion seeding, ultrasonication introduces scratches, defects and residual nanodiamond particles. Compared to mechanical abrasion this technique leads to a better uniformity and is "softer", which means the sample is less rough after the seeding process and smoother diamond layers can be grown.<sup>[38]</sup>

### **2.1.5 Bias Enhanced Nucleation**

Bias enhanced nucleation (BEN) is an in-situ nucleation technique rather than a seeding procedure. During the first stage of diamond deposition the substrate is negatively biased (100 - 250 V) with respect to the reactor chamber and methane-rich conditions (4-10 %) are used.<sup>[79]</sup> The BEN mechanism is based on the subplantation model.<sup>[80,81]</sup> Incident  $\text{CH}_x^+$  ions have an energy distribution of around 80 eV, which is sufficient to become implanted or subplanted in the top few layers of the substrate. A silicon carbide layer forms and during the first stages of nucleation primarily  $\text{sp}^2$  carbon is formed.<sup>[82]</sup> The disadvantage of the technique is that it is limited to conductive substrates.

## **2.2 Chemical vapour deposition of diamond**

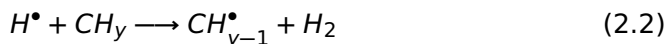
In addition to high pressure high temperature (HPHT), CVD is an interesting technique for the production of synthetic diamond. The CVD diamond process is often driven by hot filaments, plasmas, combustion flames or other techniques to ensure high temperatures which decompose larger compounds and activate atomic species for reaction at the substrate surface. This thesis will focus on Plasma Enhanced CVD (PECVD) processes and more specifically on microwave assisted plasma enhanced CVD (MW-PECVD) techniques. The plasma chemistry has been well investigated and



a generally accepted theory was summarised by Butler and Woodin.<sup>[83]</sup> Typically the process gas consists of a small amount of methane (or another carbon source) in abundance of hydrogen. The mixture can also contain dopant atom sources, e.g. PH<sub>3</sub> or TMB, or gasses like Argon (for the production of UNCD), halogens or oxygen. In the simplest gas mixture (containing only methane (CH<sub>4</sub>) and molecular hydrogen (H<sub>2</sub>)), the plasma chemistry is initiated upon ignition by the dissociation of molecular hydrogen.



Subsequently, atomic hydrogen reacts with available hydrocarbon species.



Both the reactive hydrocarbon species and atomic hydrogen are needed at the surface for the subsequent growth process, as shown in figure 2.1. The presence of atomic hydrogen activates the surface by the subtraction of a hydrogen atom to form molecular hydrogen. The active site on the surface then reacts with an active hydrocarbon. It is important to note however that this is a simplified representation, since all reactions are reversible, e.g. a growth site, created in the first step, can be passivated with hydrogen instead of completing the growth process. Moreover, the exact plasma chemistry and reactive carbon species depend a lot on the local plasma temperature. Since the first summary of Butler and Woodin in 1993, diagnostics of the growth environment have led to more clear insight into the processes that are responsible for the reactive species at the surface.<sup>[84]</sup>

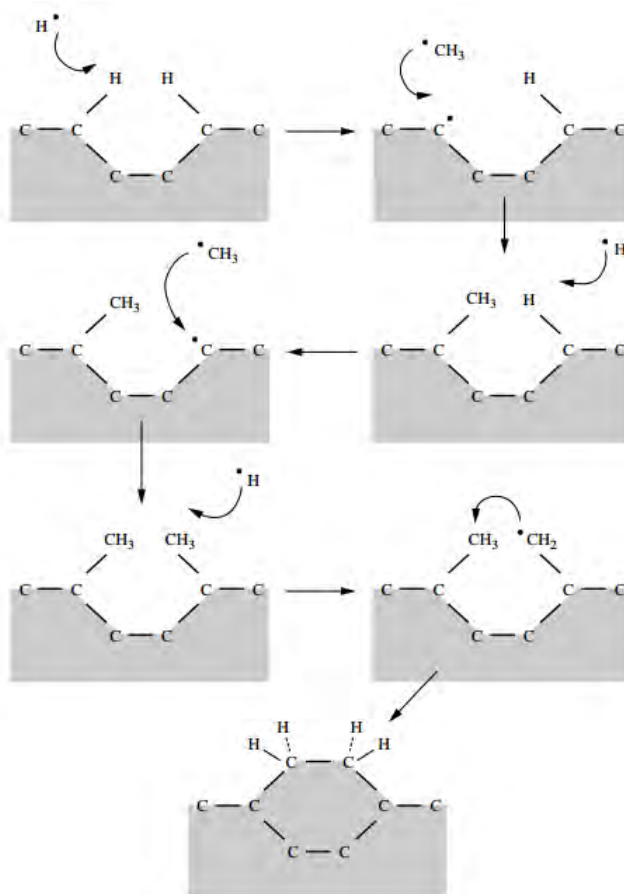


**Figure 2.1:** Simplified representation of the growth process.<sup>[10]</sup>

During the deposition process, both  $sp^2$  and  $sp^3$  hybridised carbon is formed on the substrate. Apart from activating the surface, atomic hydrogen also prevents the incorporation of hydrogen within the diamond lattice. In addition, atomic hydrogen is an effective etchant for  $sp^2$ -bonded carbon, leaving mostly  $sp^3$ -bonded diamond. This lowers the growth rate, but improves the quality of the diamond film. As mentioned above, the growth is limited by the formation and diffusion of active species to the surface. At low temperatures, etching of  $sp^2$ -bonded carbon by atomic hydrogen is limited, therefore it is necessary to add an oxygen source (e.g.  $CO_2$ ) to the plasma mixture. In presence of hydrogen and oxygen OH-radicals

are formed that are a more effective etchant for  $sp^2$  carbon phases at low temperatures.<sup>[85]</sup> Moreover atomic oxygen, in a similar fashion as atomic hydrogen, can activate the diamond surface by the abstraction of hydrogen atoms.<sup>[86]</sup> A general scheme for successful diamond growth was proposed by Bachmann *et al.* by the introduction of a C/H/O phase diagram.<sup>[87]</sup> The main idea is that, irrespective of the carbon, hydrogen and oxygen precursors and the specific deposition technique, there is a regime where diamond deposition is successful. However, successful diamond growth still requires intense optimisation of the process parameters, such as pressure and microwave power, which control the plasma density and substrate temperature.

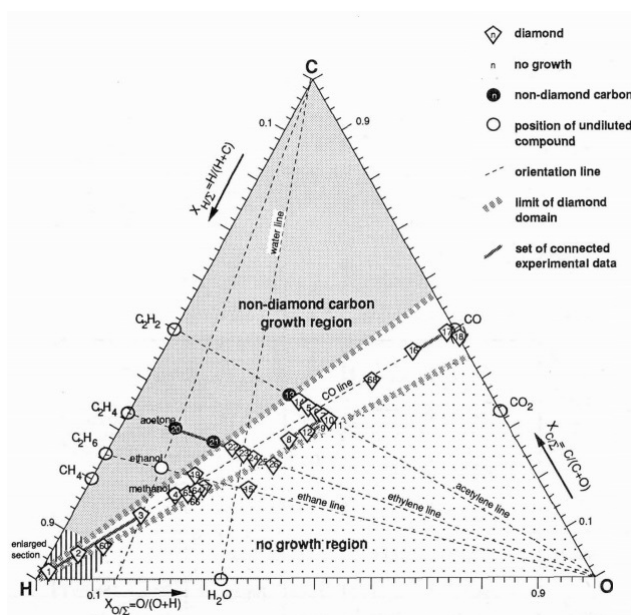


**Figure 2.2:** The C/H/O-phase diagram of diamond CVD, also known as the Bachmann diagram. It comprises more than 80 experiments from over 25 different sources and provides a common basis for all diamond CVD methods. Successful diamond synthesis is, independent from the method and the starting materials used, only feasible within a well-defined diamond domain in the diagram. [Copied from<sup>[87]</sup>]

## 2.3 Resonance cavity plasma enhanced microwave systems

One of the most common microwave plasma enhanced CVD systems is based on a resonance cavity. In this thesis, some samples were grown in a commercially available ASTeX 6500 series, with a 8 kW, 2.45 GHz microwave power generator. The design consists of three major compo-



**Figure 2.3:** Picture of the ASTeX 6500 reactor as installed at IMO.

nents: the vacuum base, the gas distribution system and the instrumentation rack. The vacuum base, which is attached to both a rough (rotational) pump and a turbomolecular pump, contains a cylindrical reactor chamber and microwave components. The microwave system is responsible for plasma ignition and includes a magnetron power head, wave guides, a three-stub tuner head, to minimize the reflected power, and a dummy load to dissipate reflected microwaves. Inside the water cooled aluminium reactor chamber the plasma is generated in a microwave cavity. The mi-

microwave coupler ensures a local maximum of the electric field in the centre of the cavity, i.e. the symmetric plasma ball is centred around the substrate holder. The Mo substrate holder or "puck" sits in the centre of the substrate stage, which is water cooled to eliminate excessive heating by the plasma at high power density regimes and ensure the desired substrate temperature. Different designs of substrate holders allow sample sizes up to 4 inch. Around the substrate stage a quartz deflector ring is placed to capture particulate carbon material which can be formed during deposition. By minimising carbon particles in the exhaust flow the entire chamber and vacuum lines last longer. The quartz ring itself can be cleaned by baking in an oxygen-rich environment to burn remaining carbon material at temperatures above 400 °C. The reactor wall contains a number of quartz windows for plasma diagnostics. The gas distribution system, responsible for the process gas inlet, contains six channels with each an individual mass flow controller. Currently only four channels are being used. Channel 1 delivers a maximum flow rate of 1000 sccm of hydrogen with a purity of 6N. Methane CH<sub>4</sub> (6N) is fed into the chamber via channel 2 (maximum flow rate 100 sccm max). 1000 ppm TMB (2.5N) in hydrogen (6N) is provided through channel 3 (maximum flow rate 100 sccm) as the dopant gas. Channel 4 (maximum flow rate 10 sccm) is dedicated to oxygen (6N) which is used e.g. for chamber cleaning in combination with hydrogen. The maximum chamber pressure is set around 240 Torr. Typical working conditions are around 3 - 4 kW, 30 - 45 Torr, and 500 sccm gas input. The base pressure is about  $1 \cdot 10^{-6}$  Torr and during deposition a throttle valve controls the working pressure.

## **2.4 Plasma enhanced linear antenna microwave systems**

An alternative to resonance cavity systems is based on linear antenna PE CVD (LA PE CVD) technology.

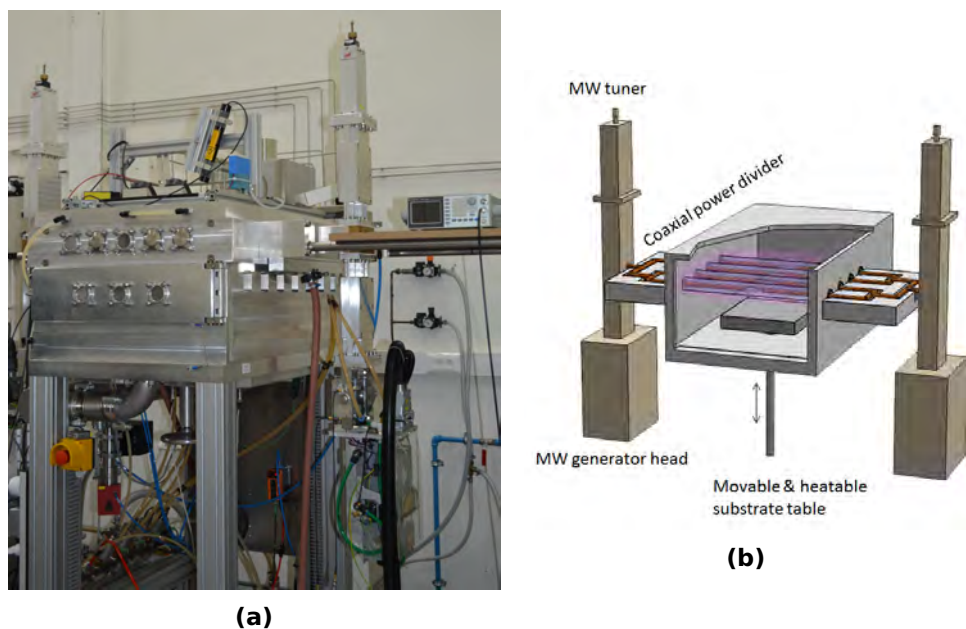


**Figure 2.4:** a) Picture and b) schematic representation of the linear antenna microwave chemical vapour deposition system as installed at IMO.

The configuration at IMO is shown in figure 2.4a. The NCS 6-300 system consists of a water cooled vacuum chamber containing the planar microwave plasma source, a process gas distribution system and a substrate stage. The system is controlled by a communication bus, which can be operated from a touch screen on the instrumentation rack, or operated remotely from a computer. (The computer and operational rack are not shown in the picture.) The microwave generator comprises two power supplies with two microwave magnetron heads, one on each side of the plasma source which can deliver up to 3 kW each at a frequency of 2.45 GHz, either in continuous wave mode or in pulsed mode. During pulsed operation, pulse peaks of up to 10 kW are possible at pulse frequencies up to 50 kHz, with variable duty cycles not exceeding a total average output power of 3 kW for each magnetron head. The microwaves are transported from the microwave heads to four parallel coaxial antennas via rectangular wave guides and a cascaded coaxial power divider on each side. The

coaxial plasma line is basically a coaxial transmission line, where the outer conductor is the conductive plasma discharge which forms on the outer surface of a dielectric tube. This tube acts as the vacuum-to-atmosphere interface for the microwaves and consists of clear fused quartz (Ilmasil<sup>®</sup> PN<sup>[88]</sup>) which has a low dielectric loss tangent.

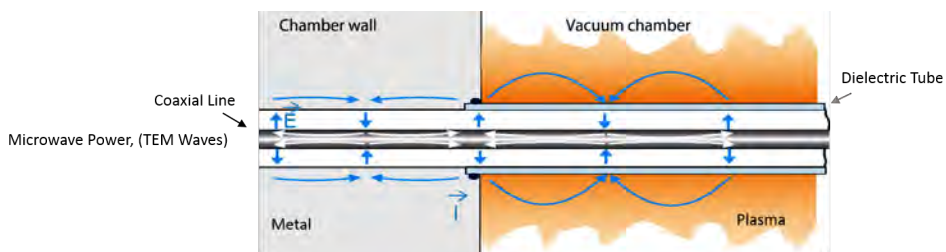


**Figure 2.5:** Wall currents inside the inner conductor (white lines) and wall currents on the metallic chamber wall and in the conductive plasma (horizontal blue lines). The plasma is ignited when the electric component of the microwave reaches the vacuum chamber and penetrates the dielectric fused quartz tube. [Courtesy of M. Liehr]

Inside the reactor walls the electric part of the microwaves propagates along a full metallic coaxial line, i.e. electric AC fields are present between the inner and outer conductor, and they induce wall currents on both conductors. When the full metallic coaxial line ends and the outer conductor is replaced by dielectric tube, the electric field of the microwaves remains, because it cannot induce wall currents in an insulator. So it penetrates the dielectric material and enters a region in which a plasma discharge can be ignited (at process pressure). The plasma ignites when the microwave electric field leaves the dielectric tube. Since a plasma loaded fused silica coaxial line usually shows a high microwave power damping, resulting in a non-uniform plasma density distribution along the tube, measures have to be introduced to level out the strong power attenuation. One such measure consists of metallic hemispherical half pipes installed inside the dielectric tubes and above the metallic inner conductor.<sup>[89]</sup> A substantial part of the propagating microwave power is transported between the inner conductor and the half pipe leading to lower power damping along the coaxial plasma line, as shown in figure 2.6.

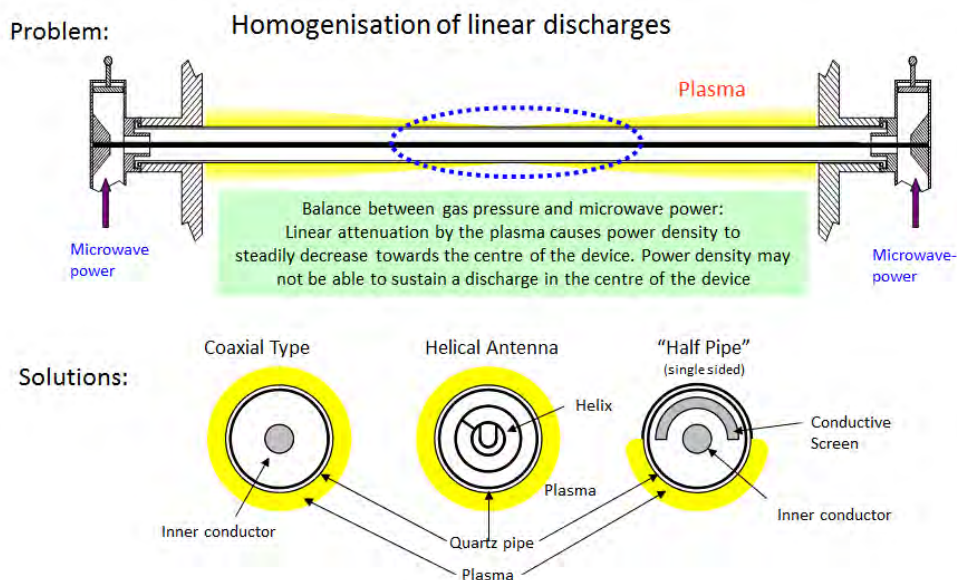


**Figure 2.6:** Schematic representation of the antenna assembly. The metallic half pipes are necessary to sustain the plasma discharge in the centre of the vacuum chamber.<sup>[89]</sup>

The coaxial plasma lines are subjected to high thermal loads during operation and therefore need to be cooled, which can be done with dried compressed air or nitrogen. Unlike the commonly used single mode microwave cavity systems (cf. ASTeX type) for high temperature "high pressure"-range (550-1100 °C and 10-50 Torr) CVD the coaxial plasma line approach allows the plasma to be in direct contact with the vacuum-to-atmosphere interface. The surface wave discharge is propelled by transverse electromagnetic wave propagation and does not depend on a resonant cavity for a selected transverse magnetic or transverse electric mode. Contact between the plasma and the vacuum-to-atmosphere interface allows for the coating very large areas (square metres), since the quartz tubes distribute the plasma evenly along their length. The maximum plasma density is, at the same time, limited by the interface material due to thermal load restrictions. However, because the quartz tubes increase the interface area, thereby lowering thermal load per area unit, no thermal damage is observed and high plasma densities can be reached. Since the sur-



face wave propagates along the 50 cm long fused silica tubes (dielectric material), the plasma discharge is not limited by the wavelength of the microwave power. The excited particles reach the substrate surface by diffusion which allows uniform diamond deposition on surfaces up to the size of the substrate stage, which is 900 cm<sup>2</sup> in this system. In order to allow excited species to reach the surface of the substrate stage without being quenched, this type of system typically operates at low pressures. Even though low pressures are used, high plasma densities ( $> 10^{11}$  cm<sup>-3</sup>) are feasible which is well above the theoretical plasma density limit of  $6 \cdot 10^{10}$  cm<sup>-3</sup> for a plasma frequency of 2.45 GHz. The Mo substrate stage can be cooled with air or heated with a resistive infrared heater (thermocoax), with temperature control through a feedback loop. Moreover, the vertical stage position (height) with respect to the coaxial plasma lines is manually adjustable as it is mounted on a vertical screw thread. The gas inlet consists of six channels, with individual mass flow controllers. Channel 1 delivers a maximum flow rate of 2020 sccm of hydrogen with a purity of 6N. Methane CH<sub>4</sub> (6N) is fed into the chamber via channel 2 (152 sccm). Channel 3 provides CO<sub>2</sub> (99.7%) (148 sccm). Channel 4 (500 sccm) is currently not in use. Channel 5 (200 sccm) is dedicated to oxygen (6N) which is used for chamber cleaning. 200 ppm PH<sub>3</sub> in hydrogen (6N) is provided through channel 6 (200 sccm) as the dopant gas. The maximum chamber pressure is set around 240 Torr. Typical working conditions vary between 1-3 kW on each head, 0.1-0.4 Torr controlled by a throttle valve, and 150 sccm gas input. It should be noted that 0.075 Torr is the lower limit of our current set-up due to the pump speed capacitance and the minimum flow of the flow controllers. The vacuum is reached through a rotational pump and the base pressure of the system is about  $2 \cdot 10^{-4}$  Torr.

### 2.4.1 Memory effect

Since the quartz tubes are the atmosphere-to-vacuum interface and the plasma itself is the outer conductor of the coaxial plasma line, the quartz

tubes and more specifically their surface are very important during deposition. After first placement of the quartz tubes, they need to be carbon coated to form a SiC layer. Unless the tubes are covered in SiC, there will not be any or extremely slow growth. This is presumably because the silicon oxide of the tubes itself is being etched by the plasma and adds oxygen to the plasma conditions, which leads to etching of the grown layer. Moreover it could be possible that the present silicon changes the plasma chemistry.

In addition, to avoid the influence of previous deposition runs, the chamber is oxygen cleaned for at least 30 min. This cleaning step is used to remove redundant carbon material, that is deposited during growth. Carbon material deposits mainly on the chamber walls and on the quartz tubes in the hot spots of the microwave field, i.e. around every 6 cm, which corresponds to the nodal plane of the 2.45 GHz generator. We observed experimentally that a short hydrogen plasma is necessary after oxygen cleaning to remove excessive oxygen remaining in the chamber, e.g. adsorbed to the chamber walls. Without an intermediate hydrogen plasma between oxygen cleaning and diamond growth, enhanced etching occurs during the first stages of growth and almost no seeds evolve into diamond grains.<sup>[90]</sup>

### **2.4.2 Continuous microwave mode**

The pioneers of nanodiamond coatings deposited with a surface wave plasma system at low temperatures (between 100°C and 500°C) onto large areas (30 × 30 cm<sup>2</sup>) were Tsugawa *et al.* in 2006.<sup>[91]</sup> In 2010, the temperature used to deposit nanocrystalline diamond reached values below 100 °C and a nucleation in the gas phase was assumed to account for diamond growth.<sup>[92]</sup> In 2011, they reported that even in hydrogen-rich conditions a high renucleation rate is obtained in surface wave plasmas, which means there is still room for improvement to obtain NCD or MCD films.<sup>[93]</sup> After these first reports, effort was devoted to characterise the

plasma by Tsugawa *et al.* They showed that the electron temperature is highest close to the vacuum-to-atmosphere interface and decreases with distance. An electron temperature of  $2.6 \pm 0.5$  eV was found for the CVD region of their surface wave plasma system, because only a thin layer is heated and excited by the microwaves, which leads to a high electron density region close to the quartz tubes from where the active species diffuse into the CVD region.<sup>[93]</sup> (For comparison, electron temperatures in conventional systems typically exceed 5 eV.<sup>[94,95]</sup>) Similar results were shown by Potocký *et al.*, where both the plasma density and electron temperature decreases with increasing distance between the substrate and the antennas.<sup>[96]</sup> At further distances, dissociation processes are not so likely to occur because of the lower electron temperature in this region: electrons with energies over 10 eV are necessary to dissociate ( $> 9$  eV)  $\text{H}_2$  and ionize  $\text{H}_2$  and H (the ionization potentials are 15.4 and 13.6 eV respectively). For the dissociation of  $\text{CH}_4$ , electrons with energies of 9, 10, 11 and 12 eV are required for successive H-abstraction.

Recently, a lot of work has been done by the group in the Czech Republic to optimise the process parameters in order to control the deposited morphology, and accomplish NCD or MCD growth. A summary of their findings is listed below.

- Babchenko *et al.* showed the effect of the distance dependence on diamond growth with a surface wave plasma: at closer distances crystalline, well-faceted layers are obtained at higher pressures compared to growth at further distances.<sup>[97]</sup>
- The beneficial effect of decreasing pressure on the growth of faceted nanocrystalline films has been shown by a number of reports.<sup>[96,98]</sup> A decrease in pressure leads to prolonging of the mean free path of excited species and expanding of the plasma towards the substrate which seems to enhance reactions at the substrate surface.<sup>[98]</sup> Both the plasma density and electron temperature drop with increasing pressure, which leads to a decrease in the atomic hydrogen concen-

tration and shifts the growth regime towards UNCD growth.<sup>[96,99]</sup>

- The addition of CO<sub>2</sub> to the gas phase leads to an increase in atomic hydrogen and sp<sup>3</sup> content.<sup>[100]</sup> Oxygen suppresses the formation of sp<sup>2</sup> phases and plays an important role for low temperature diamond growth, as explained in section 2.2.
- An extension of the diamond growth regime in the C/H/O phase diagram by Bachmann,<sup>[87]</sup> was reported by Potocký *et al.* This is presumably due to the surface wave nature of the deposition system, the low deposition pressure and temperature.<sup>[101]</sup>
- The morphology of nanocrystalline diamond films depends significantly on the microwave power.<sup>[102]</sup> An increase in power causes an increase in plasma density and this leads to an increase of active species which is beneficial for the deposition of high quality, faceted nanocrystalline diamond layers.
- Supply of thermal heat from the substrate surface leads to an increase in growth speed due to enhanced thermal activation of the growth process and a change in surface chemistry.<sup>[102]</sup>
- Diamond growth in a linear antenna deposition system is a combination of different growth mechanisms, i.e. active growth species and dominant development of a specific crystal face, that are responsible for different activation energies at low and high temperatures.<sup>[102]</sup> Tsugawa *et al.* ascribed this difference in activation energies to the different growth regimes for NCD and UNCD.<sup>[92]</sup>

### 2.4.3 Pulsed microwave mode

When the system operates in continuous wave (CW) mode the plasma density is constant under steady state conditions, i.e. at a fixed power input, because of the synergy between the production and recombination of charged species. In case of delicate substrate materials that can't

withstand high thermal loads the use of pulsed discharges can offer a solution. Pulsed discharges can increase the performance by the use of higher microwave peak powers, which increases the electron temperature while keeping the mean consumed power constant and the thermal load low. During the use of pulsed mode, with repetition rates up to 20 kHz, non-linear MW absorption takes place, leading to higher plasma densities for the same average power input compared to continuous wave mode, as shown in figure 2.7.<sup>[103]</sup> The electron density does not decay completely at the end of each microwave pulse but tails off with some delay even at low pulse frequencies. With increasing pulse frequencies the pulse-off period becomes shorter and the plasma particle recombination becomes less dominant. Hence, the density of atomic hydrogen can remain almost at the pulse-on level even during the pulse-off period for very high pulse frequencies which suppresses renucleation and promotes higher  $sp^3/sp^2$  ratios, allowing preparation of high quality NCD films with lower  $sp^2$ -bonded carbon content.<sup>[104,105]</sup>

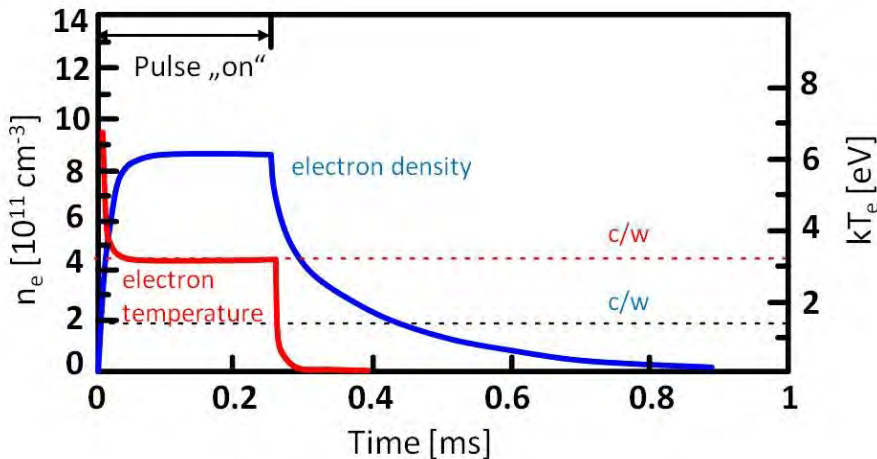


**Figure 2.7:** Time evolution of the plasma density,  $n_e$  and electron temperature  $kT_e$  for a time-average power of 500 W, a duty cycle of 25% and a frequency of 1 kHz.<sup>[103]</sup>

As shown in figure 2.8, there is no drop in the plasma intensity during the off-period of the pulse at higher pulse frequencies, which confirms that

the off-time is too short for recombination to take place and the atomic hydrogen concentration remains high. During one pulse cycle both activation and decay take place, but because the off-period is too short for recombination, the process shows the same behaviour as in continuous wave mode.

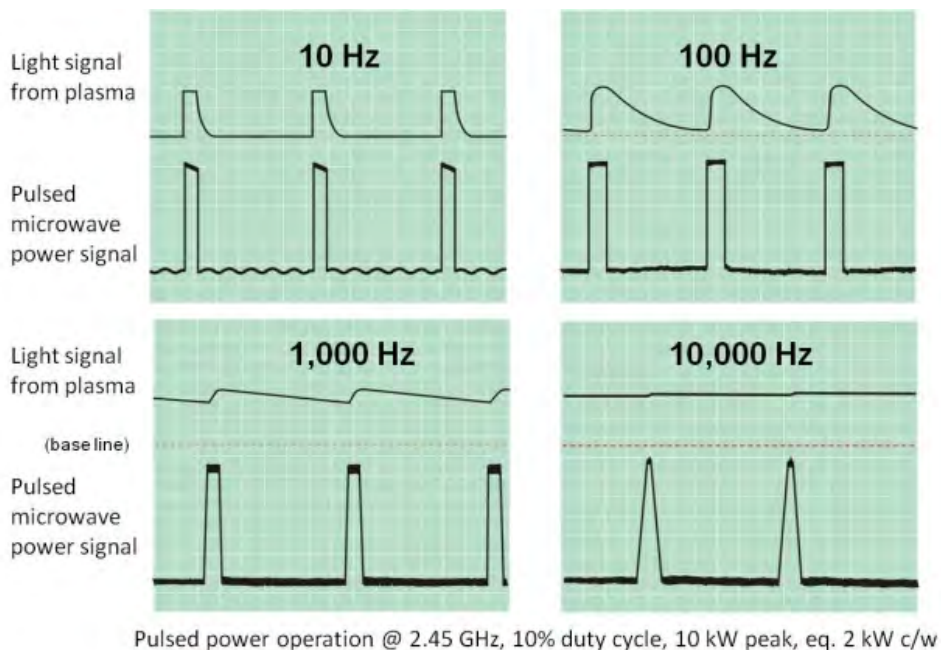


**Figure 2.8:** Summary of the plasma characteristics (determined by the light intensity) with varying pulse frequency. At high pulse frequencies, the light intensity becomes constant. [Courtesy of M. Liehr]

To our knowledge, the first report on pulsed discharges for diamond deposition dates from 1994 and is based on a quartz tubular resonant cavity reactor.<sup>[106]</sup> Laimer and Matsumoto presented an increase in the  $H_{\alpha}$  line, indicating a higher atomic hydrogen content for pulsed discharges during the pulse, for pulse frequencies between 50 Hz and 20 kHz. The average hydrogen concentration is similar for pulsed and continuous wave mode and the resulting diamond layers are comparable. Based on these results, attempts to improve the diamond quality in resonant cavity reactors using pulsed discharges were successful. An increased  $sp^3/sp^2$  ratio in Raman

spectroscopy and increased growth rates were reported for pulsed mode compared to continuous mode.<sup>[107–109]</sup> In the early 2000s, the group of Gicquel at CNRS, published work on the modelling of pulsed discharges in a quartz tubular reactor.<sup>[110]</sup> The main general results are briefly mentioned here:

- In CH<sub>4</sub>/H<sub>2</sub> plasmas the amount of hydrogen related ions increases during the pulse-on period, while methane is converted into acetylene (C<sub>2</sub>H<sub>2</sub>) during this period. During the off-period CH<sub>4</sub> is regenerated. The CH<sub>3</sub> radical is produced via thermal dissociation of CH<sub>4</sub> and is thus more abundant during the off-period or in colder plasma conditions. The atomic hydrogen concentration, which correlates with the electron temperature, is responsible for the dissociation of hydrocarbons.
- Pulse-on/pulse-off ratios, also called duty cycles, higher than 50 % don't show any significant change in atomic hydrogen concentration compared to continuous wave mode. The most important or relevant conclusion of the work of Gicquel *et al.* probably is the importance of the duty cycle value with a given frequency, which can be responsible for opposite conclusions found in literature. This means that for a given frequency, the duty cycle is determinative for whether or not pulsed mode is beneficial for the quality of the nanocrystalline layer.

For surface wave plasmas it is important to keep in mind that the plasma changes during the pulse due to the intrinsic plasma properties. At the start of the pulse, the plasma only excites a very small volume, which leads to very high local gas temperatures. In the second phase, the plasma volume increases and the gas temperature decreases. This gas temperature is set by the pulse peak power density and the duty cycle. Both the electron and gas temperature decrease with an increase in duty cycle for a constant pulse peak power.<sup>[111]</sup>

- The atomic hydrogen concentration increases with duty cycle and is

dominated by electronic dissociation (as mentioned above for continuous wave mode). Recombination of H-atoms is limited during the short off-times of the pulse.<sup>[111]</sup>

- The CH<sub>3</sub> radical concentration decreases with duty cycle, probably because the gas temperature decreases as well and the thermal dissociation of methane decreases.<sup>[111]</sup>

For surface wave plasmas, research on pulsed discharges is still ongoing. Fendrych *et al.* and Vlcek *et al.*, confirmed that it is possible to grow good quality NCD layers in pulsed mode with the addition of CO<sub>2</sub> in a set-up similar to the linear antenna system in Hasselt.<sup>[100,112]</sup> The quality is related to an increase in atomic hydrogen concentration with pulse frequency which is ascribed to non-linear microwave absorption by the plasma in high frequency pulse modes, as shown by Taylor *et al.*<sup>[105]</sup> Similar results were reported later by Vlcek and Mistrik; the diamond quality (and growth rate) is improved with increasing pulse frequency, more specifically shorter off-times with the same on-time, because a high atomic hydrogen concentration is maintained due to limited recombination rates.<sup>[104,113]</sup> For low pulse frequencies, the plasma temperature and density are increased compared to CW mode during the on-time of the pulse, but there is a fast decrease during the off-time. With high frequencies, the plasma temperature and electron density become more constant during the entire process (as explained in figure 2.8). The best results, in terms of crystallinity, faceting and sp<sup>3</sup>/sp<sup>2</sup> ratio, reported to date are obtained with a frequency of 14.3 kHz and using 30 and 50 % duty cycle.<sup>[100,105]</sup> An example of a typical pulse profile is shown in figure 2.9.

It should be noted that the LA MW CVD is the only commercially available scalable MW deposition system today based on this unique plasma. Whereas a classical system easily leads to local changes in the surface properties due to inhomogeneity of the plasma ball, layers deposited with linear antenna technology are homogeneous with respect to thickness and dopant incorporation, and this independent of the type of substrate ma-



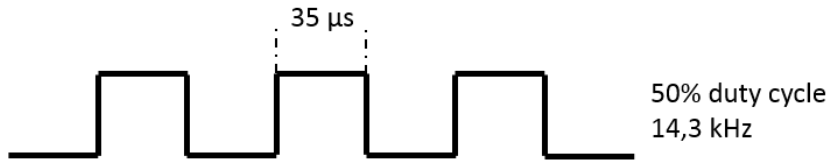


**Figure 2.9:** Example of a typical pulse profile used for the growth of nanocrystalline diamond with a linear antenna set-up.<sup>[105]</sup>

terial. Nevertheless, diamond deposition systems based on surface wave plasma have been realised without the use of linear antennas as well, i.e. with a distributed antenna array.<sup>[114]</sup> The system used at LSPM-CNRS consists of 16 coaxial plasma sources inserted in a square metallic flange and arranged in a  $4 \times 4$  matrix.

# Chapter 3

## Characterisation and experimental techniques

### 3.1 In-situ laser interferometry

During growth the substrate temperature is monitored with a hand-held single color optical pyrometer (Cyclops 52, Minolta), assuming the optical emission coefficient,  $\epsilon$ , is 0.3. The layer thickness is determined by in-situ laser interferometry. A He-Ne laser (633 nm) is aimed at the substrate surface through one of the top windows. Since the light is reflected both from the surface and from the growing diamond layer, the interference pattern, collected by a Si photodiode, can be used to determine film thickness as described below. The light reflected by the NCD surface and the light reflected by the underlying substrate interferes because of the optical path difference (OPD), which means the film thickness can be derived from the interference pattern. Implementing Snells' law:

$$n_0 \cdot \sin \alpha = n_{NCD} \cdot \sin \beta \quad (3.1)$$

the OPD between the light reflected by the NCD surface and the light

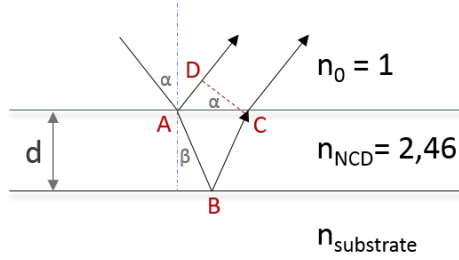


**Figure 3.1:** Schematic representation of the reflection of the laser beam by the NCD layer (at point A) and by the underlying substrate (at point B).

reflected by the underlying substrate is equal to:

$$\begin{aligned}
 OPD &= (|AB| + |BC|) \cdot n_{NCD} - |AD| \cdot n_0 \\
 &= 2 \cdot n_{NCD} \cdot \frac{d}{\cos \beta} - 2d \cdot n_0 \cdot \sin \alpha \cdot \tan \beta \\
 &= 2 \cdot n_{NCD} \cdot \frac{d}{\cos \beta} \cdot (1 - \sin^2 \beta) \\
 &= 2 \cdot n_{NCD} \cdot d \cdot \cos \beta
 \end{aligned} \tag{3.2}$$

Constructive interference takes place for:

$$2 \cdot n_{NCD} \cdot d \cdot \cos \beta = m \cdot \lambda \tag{3.3}$$

which, for the geometry in the linear antenna system ( $\alpha = 20^\circ$ ) and the refractive index of diamond, means the first extremum occurs for a layer thickness of 65 nm and an entire period finishes after 130 nm. With time the overall intensity of the interference pattern will decrease due to scattering at an increasingly rough diamond surface.

## 3.2 Optical Emission Spectroscopy

Atoms and ions present in a plasma are excited to higher electronic states in this highly energetic environment. Upon relaxation to lower energy states, and eventually ground state, photons are emitted. For each spe-

cific atom the energy of these photons is equal to the difference between higher and lower energy states, and thus each element creates a characteristic set of spectral emission lines. The total spectrum acquired is a collection of spectral lines of all excited states in the plasma. The intensity of each line depends on the concentration of that species in the plasma. For this thesis an Avantes FC UV600-2 optical fiber was used to collect the emitted light through one of the top windows and transfer it to an AvaSpec-2048 (Avantes) spectrometer which recorded the spectrum. The spectrometer contains a 2048 pixel charge coupled device (CCD) detector array and covers a wavelength range between 200 nm and 1100 nm. Shortpass filters remove all signals below 450 nm or 525 nm and in particular  $H_{\alpha}$  and  $H_{\beta}$  lines. This ensures an increased signal-to-noise ratio for less pronounced signals in the higher wavelength ranges.

### **3.3 Scanning Electron Microscopy**

For scanning electron microscopy (SEM) a focused electron beam is used to image samples from mm down to nm scale, with magnifications up to 200 000 times. An SEM set-up can be used to reveal information about the sample morphology, chemical composition and crystalline structure. The electron beam consists of high energy (primary) electrons (typically around 15 kV for imaging nanocrystalline samples produced for this thesis) and is aimed at the sample surface. Upon interaction with the sample, the primary electrons experience both elastic and inelastic scattering. In case of elastic scattering, the energy of the primary electrons is not changed in the collision and back scattered electrons (BSE) are reflected from the sample. BSE give information about the distribution of the sample species since the intensity depends on the atomic number of the specimen thereby showing contrast in composition. The higher the atomic number, the more electrons are backscattered. Inelastically scattered electrons give rise to secondary electrons, which can only escape from the sample

and reach the detector if they are generated within the top layer of the sample surface, i.e. the number of secondary electrons reaching the detector is highly dependent on morphological characteristics, and thus a topographical image is created. The sample can also emit X-rays in case of inelastic collisions with the electron beam. During collision, the high-energy primary electrons knock out electrons from a core-level (1s, 2s, etc.) in the top few micrometres (1-3  $\mu\text{m}$  for 15 kV). An atom with a 'hole' in this level (E1) is unstable, and so an electron from a higher energy level (E2) drops down to fill this hole, emitting an X-ray of characteristic wavelength (E2-E1). In energy dispersive X-ray (EDX) analysis, the X-rays emitted by the sample are collected in function of their energy which gives information about the chemical composition of the sample. SEM analysis is non-destructive and it has become a much used imaging technique for diamond samples. At IMO, a FEI Quanta 200 FEG SEM is used.

### **3.4 Transmission Electron Microscopy**

Transmission electron microscopy (TEM) uses a broad, nearly parallel, electron beam which is transmitted through a very thin sample. The electrons interact with the specimen during transmission, which means the transmitted electrons form a representative image which is detected by a CCD camera. The contrast in this TEM image depends on the absorption, as determined by the composition and thickness, and diffraction of electrons by the sample material, depending on the crystal structure and orientation. Dependent on the location and size of the aperture of the objective lens, only the direct beam (bright field) or only diffracted beams (dark field) can pass. Practically, in modern bright field TEM mode, both the central beam and a few diffracted beams are collected because of the size of the aperture. This gives information about the absorption contrast, and thus relative sample thickness, and diffraction contrast of the sample material. Dark field TEM, i.e. the direct electron beam is blocked

and only diffracted electrons are being collected, is mainly used to image defects and other crystal imperfections. Modern TEM setups can easily switch between bright and dark field mode and allow for tilting of the sample in order to select a specific zone axis. In an alternative mode a transmission electron microscope can also give information about chemical species through energy dispersive X-ray spectroscopy (EDX), about the crystal structure and orientation using selected area electron diffraction (SAED) and about the electronic structure by electron energy loss spectroscopy (EELS). The energy of the incoming electron beam loses energy to the sample upon interaction. This energy loss is characteristic for the electron-sample interaction and thereby gives information on elemental composition. In EELS, the intensity is plotted versus the electron energy loss. Inelastically scattered electrons with an energy around 285-290 eV less than the incoming beam, are characteristic for carbon, since this is the energy necessary to remove an inner-shell electron from a carbon atom. Through the fine structure of the carbon K EELS edge the crystalline structure can be determined, which means it can distinguish between  $sp^2$  and  $sp^3$  carbon.  $sp^2$  carbon compounds show a peak at 285 eV, while diamond has a different edge shape and a peak maximum at 292.6 eV.<sup>[115]</sup> SAED is a crystallographic diffraction technique that is used to determine the crystalline structure and orientation, similar to XRD (see section 3.5). Incoming electrons are diffracted to certain angles which are characteristic for the crystal orientation and determined by Bragg's law:

$$2 \cdot d \cdot \sin \theta = n \cdot \lambda \quad (3.4)$$

where  $d$  is the spacing between diffracting planes,  $\theta$  the incident angle (which is also called the diffraction angle),  $n$  an integer, and  $\lambda$  the wavelength of the beam. The reflections at specific scattering angles can thus be related to interplane distances in crystals to identify materials, and to determine crystal orientations. A selected electron area diffraction pattern can be created for areas as small as several hundred nanometres in size.

The crystal and even atomic structure can be investigated by high-resolution transmission electron microscopy (HRTEM). In HRTEM a phase contrast image is obtained from the interference between electron waves. Even though these interactions are complex, a qualitative idea about the crystalline structure can be obtained. For scanning transmission electron microscopy (STEM) the electron beam is focused into a narrow spot and scanned over the sample in order to map the sample. Annular dark field STEM allows to gain more insight into the sample composition, since elements with a high Z-number show enhanced scattering of the electron beam. The annular dark field detector is a ring, i.e. an annular aperture, that is centred around the unscattered beam (without collecting this beam).

The TEM used for the results presented in this thesis is a FEI Titan cubed aberration-corrected microscope equipped with Gatan EELS spectrometer and all experiments were done at 300 kV. Depending on the density of the sample material, the sample can be at maximum a few hundreds of nanometres thick for transmission electron microscopy, which means appropriate sample preparation is necessary. To obtain electron transparent TEM foils the samples are ion milled.

The machine used for focused ion beam (FIB) milling is a FEI dual beam (equipped with electron gun and Ga ion gun) Helios Nanolab 650. For cross-sectional imaging, first, a protective platinum layer is deposited onto the sample so the surface is protected during further thinning. A special gas injection system in the FIB contains a Pt organic compound, which is aimed at the desired location using the electron gun to very gently deposit a Pt containing amorphous carbon layer. In the second step Pt is deposited with the ion beam of the Ga gun using low currents, yet higher energy than with the electron gun, enabling the deposition of almost pure Pt. Then two parallel trenches are made on both sides of the area of interest, thereby creating a lamella with a thickness of about 1  $\mu\text{m}$ . The length of the trenches is 15  $\mu\text{m}$ , the width and depth are 4  $\mu\text{m}$  and 3  $\mu\text{m}$  respectively. The lamella is then partly cut from the bulk and attached to

a special manipulator by platinum. Finally, the lamella is completely removed from the sample by ion milling of the remaining connections. With use of the manipulator the lamella is placed onto the TEM copper grid and attached by platinum. Then the connection between the manipulator and lamella is milled away. During final thinning the width of the lamella is slowly reduced by ion milling of both sides until it reaches less than 100 nm. In this process an ion gun is aimed perpendicular to the top of the lamella, i.e. to the protective platinum layer. The voltage of the ion gun is slowly decreased in this process in order to minimize the amorphisation of the lamella's surface.

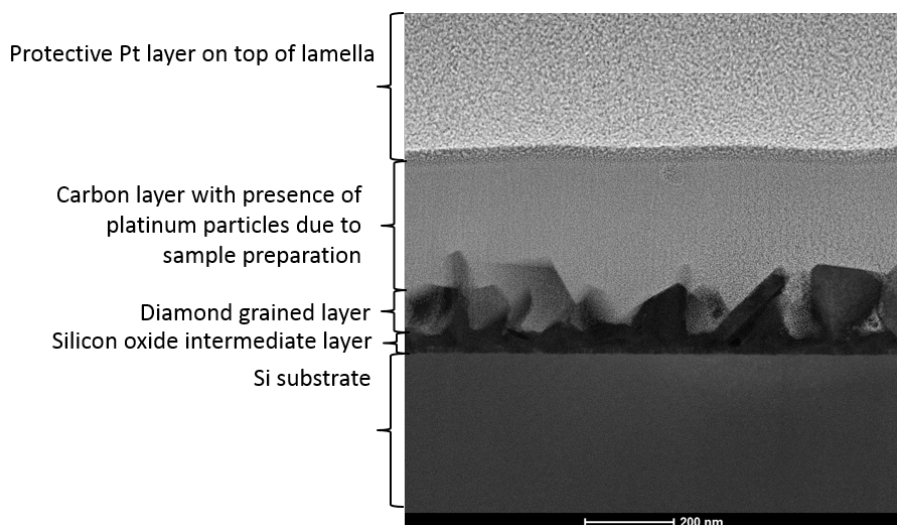


**Figure 3.2:** TEM cross sectional view of a sample after sample preparation.

The preparation for plan view imaging of the samples was done differently. First, a small piece around 2 by 4 mm is cut from the sample and the diamond side (front) is attached to the holder of the polishing machine with an easily removable glue. Then the silicon backside is polished by a MultiPrep™ polishing system, with a rotating abrasive plane. When the sample is thin enough, i.e. around 20  $\mu\text{m}$ , it is removed from the holder and attached to the copper grid. Further thinning is performed by an Ar milling



machine Leica EM RES102, which has two broad Ar ion beams. The sample is in between the beams and is milled from both sides almost parallel to the surface of the sample (the angle between Ar beam and the surface is around 6 degrees). In this way mostly the middle part of the sample is being thinned until a small hole in the middle appears, which means the sample is thin enough. The optical system of the milling machine monitors the progress. The voltage of the Ar ion guns decreases from 5-7 kV to 0,5-1 kV during milling in order to control the speed of the milling and reduce amorphisation.

### 3.5 X-ray Diffraction

X-ray diffraction (XRD) can be used to identify crystal structure, orientation and lattice parameters in crystalline materials. Incident X-rays are diffracted in many directions by the atoms of a material. Since the atoms are strictly ordered in a crystal, diffracted X-rays only interfere constructively when Bragg's law is fulfilled. Similar to SAED, the scattering angles of the reflections are related to interplane distances in crystals and can be used to identify materials and to determine crystal orientations. The XRD measurements are performed with a Bruker D8 discover diffractometer with a theta-theta goniometer. The system is equipped with a Göbel mirror and incoming Cu  $K_{\alpha 1}$  ( $\lambda = 1.54 \text{ \AA}$ ) X-rays are used. Diffracted X-rays are detected by a lynxeye detector. This 1D detector uses 192 separate channels (Si strips) that each act as a single detector. The position of the X-ray source ( $\theta$ ) and detector ( $2\theta$ ) with respect to the sample surface is varied. When Bragg's law is satisfied for a specific crystal orientation X-rays are reflected and a spike in intensity at  $2\theta$  is observed. For nanocrystalline diamond reflections are expected at following  $2\theta$  angles.

These crystal planes are described by their Miller indices, i.e. three integers (hkl) that denote a plane. The Miller indices represent the reciprocal of where the plane intersects the main crystallographic axes. For exam-

**Table 3.1**

$2\theta$	Intensity (%)	Crystal plane
43.9	100	(111)
75.3	25	(220)
91.5	16	(311)
119.5	8	(400)
140.6	16	(331)

ple, in figure 3.3, the (111) plane of a diamond unit cell is shown. These

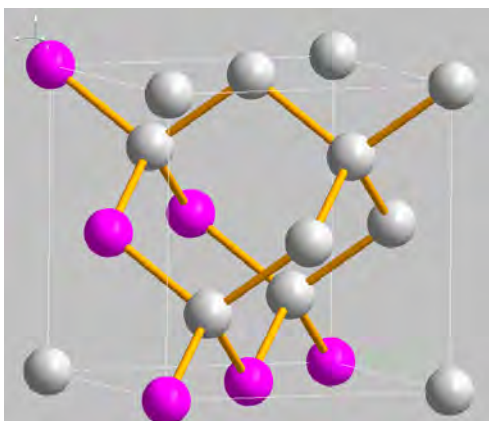


**Figure 3.3:** Unit cell of cubic diamond. The carbon atoms highlighted in pink show a  $\{111\}$  plane.

Miller indices can be used to describe one plane, e.g. (111), or a family of planes equal to it,  $\{111\}$ . Using square brackets, a direction is described, e.g.  $[111]$  is a direction normal to the (111) plane. And similar to above a family of directions is denoted with  $\langle 111 \rangle$ . As shown in table 3.2, these families of planes have characteristics angles with respect to each other, which can be used to determine the crystal facets of a diamond grain.

**Table 3.2:** Calculated angles between crystal planes in diamond.

	$\{100\}$	$\{110\}$	$\{111\}$
$\{100\}$	$0^\circ$ or $90^\circ$	$45^\circ$ or $90^\circ$	$54.73^\circ$
$\{110\}$	$45^\circ$ or $90^\circ$	$0^\circ$ , $60^\circ$ or $90^\circ$	$35.26^\circ$ or $90^\circ$
$\{111\}$	$54.73^\circ$	$35.26^\circ$ or $90^\circ$	$0^\circ$ or $70.53^\circ$

## 3.6 Raman Spectroscopy

In Raman spectroscopy a sample is irradiated with a laser and the back-scattered light is detected, giving information about molecular or lattice vibrations (for solids). Most of the light scatters elastically (Rayleigh scattering), i.e. there is no interaction with the sample. A very small (5-10 %) amount of the incident light however interacts with the sample during scattering. In this case the energy of the scattered light differs from the incident light by an amount that is characteristic to the vibrational energy levels of the compounds in the sample. By interacting with the incident light, the sample can either absorb or release energy. In the case where the sample absorbs energy, the scattered photon has lower energy, and the process is called Stokes scattering. During anti-Stokes scattering a photon with higher energy than the incident light is emitted because the sample releases energy. Since this requires the molecules or lattice to be in a higher energy vibrational state, anti-Stokes scattering is much less intense. A Raman spectrum summarizes the intensity of this inelastically (Stokes) scattered light versus the frequency and is a fingerprint of the sample material. The advantage is that Raman Spectroscopy is a straight-forward, easy accessible and non-destructive characterisation method. For the purposes of this thesis, a blue Lexel SHG-95 Ar-ion laser ( $\lambda = 488 \text{ nm}$ ) was used in combination with a confocal microscope with a Horiba Jobin-Yvon T64000 micro-Raman spectrometer. All measurements were performed at room temperature with a liquid nitrogen cooled CCD detector for varying time periods that ensure a high signal-to-noise ratio. Raman spectroscopy is a valuable tool to distinguish between carbon allotropes or even to determine the ratio of  $sp^2$  versus  $sp^3$  in a compound. Since the bond energy for  $sp^2$  carbons is higher, their signal is shifted to higher wavenumber compared to the signal for diamond, located at  $1332 \text{ cm}^{-1}$ . The exact location of the diamond Raman peak is known to depend on the stress in the diamond layer. The diamond peak shifts to higher wavenumber under compressive stress and to lower wavenumber under

tensile stress.<sup>[116]</sup> The G band (characteristic for graphite) typically lies around  $1550\text{ cm}^{-1}$ . In nano- or polycrystalline diamond other signature peaks of  $sp^2$  carbon can arise, i.e. the D band, characteristic for defects in  $sp^2$  phases, lies around  $1350\text{ cm}^{-1}$  and if transpolyacetylene is present at the grain boundaries this causes a peak around  $1450\text{ cm}^{-1}$ . Closer examination of these peaks allows for an estimate of the diamond quality, i.e. the ratio between  $sp^3$  and  $sp^2$  carbon. A method proposed by Silva *et al.* was adopted to qualitatively compare the  $sp^3$  content of the obtained NCD samples.<sup>[117]</sup>, as given by equation 3.5,

$$sp^3(\%) = 100 \cdot \left( \frac{75 \cdot A_{diamond}}{75 \cdot A_{diamond} + A_{non-diamond}} \right) \quad (3.5)$$

in which  $A_{diamond}$  is the integrated area of the diamond Raman peak and  $A_{non-diamond}$  is the sum of the integrated areas of  $sp^2$  related peaks.

The scattering efficiency depends on the laser wavelength, i.e. for a blue or green laser,  $sp^2$  scatters about 50 times more strongly than  $sp^3$ , while for an IR laser  $sp^2$  scatters 200 times more efficiently.<sup>[118]</sup> At these wavelengths, the scattering efficiency of  $sp^2$  carbon is higher than that of diamond, since the  $\pi$  bonds give rise to a higher polarisability of  $sp^2$  carbon. Generally, correction factors between 50 and 233 are used to account for the larger cross-section of  $sp^2$  carbon.<sup>[119][120]</sup> Here, a correction factor of 75 (similar to Silva *et al.*<sup>[117]</sup>) was used to correct for the enhanced scattering of all  $sp^2$  carbon, so there was no distinction made between the correction for graphite and acetylene. The  $sp^3$  carbon content gives a qualitative measure for comparison between various samples and is by no means a quantification of the actual  $sp^3$  content. The errors on the  $sp^3$  are calculated from the errors on the fit of the individual peaks. After removal of the background, the diamond peak was fitted by a Lorentzian peak with the use of Fityk software.<sup>[121]</sup>  $sp^2$  carbon contributions were fitted by Gaussian curves.<sup>[121]</sup> These fitting procedures lead to errors on the estimated area because of the large spread between measurement points, overlap between the peaks and background removal. The errors

on the individual peaks were then used to calculate the error on the  $sp^3$  content. The errors on the estimated  $sp^3$  content increase with decreasing  $sp^3$  content since the relative spread on the single measurement points of the entire curve is bigger, since the absolute intensity (of the diamond peak) is lower. Therefore the errors are more an indication of the spread of the points than of the accordance between the fit and the actual curve. For boron-doped samples, the diamond peak shifts towards lower wavenumber with increasing boron concentration, which is attributed to a combination of the self-energy shift due to the Fano interaction and tensile stress in the lattice from the incorporation of substantial quantities of boron.<sup>[122]</sup> In addition, analysis of the peak around  $500\text{ cm}^{-1}$  gives information about the boron content.<sup>[123]</sup> This peak can be fitted by a Gaussian and a Lorentzian component (see figure 3.4a). The peak position of the latter decreases with increasing B/C ratio (see figure 3.4b).

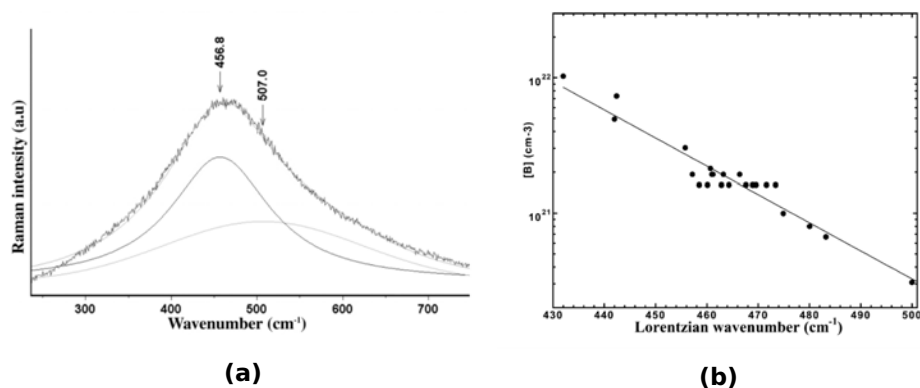


**Figure 3.4:** a) Example of the fit of the  $500\text{ cm}^{-1}$  peak by a Lorentzian ( $456.8\text{ cm}^{-1}$ ) and a Gaussian component ( $507.0\text{ cm}^{-1}$ ) for a sample grown with 8000 ppm B/C in the gas phase. b) Boron concentration of B-doped polycrystalline films as function of wavenumber of the Lorentzian component of the peak around  $500\text{ cm}^{-1}$ . [Reprinted from<sup>[123]</sup>

### 3.7 Surface curvature measurements

Upon deposition of a film onto a substrate, stress is generated both in the substrate and in the deposited film. The stress in the film can either be compressive or tensile, dependent on the characteristics of the deposition process. In the case where there is excessive film stress cracking or even delamination of the film takes place. In order to estimate the amount of stress, surface curvature measurements were performed in the framework of this thesis. The surface curvature before and after film deposition is measured along the same trace with a Bruker Dektak XT™ stylus profiler with a height resolution of 1 Å (at 6.55 μm range). The radii of the surface

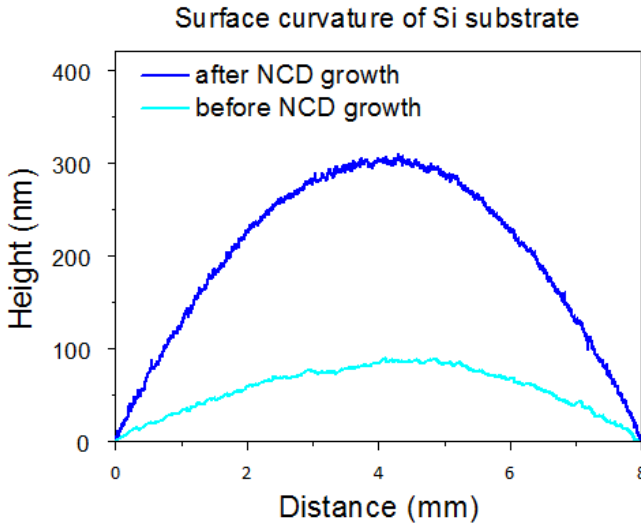


**Figure 3.5:** The surface curvature as determined by dektak profilometry before and after diamond film deposition.

curvature are fit with Spyder software to a least squares circle fitting. Once the radii of curvature are known, the stress in the film can be calculated with the Stoney equation:

$$\sigma = \frac{1}{6} \left( \frac{1}{R_{after}} - \frac{1}{R_{initially}} \right) \frac{E_s}{(1 - \nu_s)} \frac{t_s}{t_f} \quad (3.6)$$

with  $\sigma$ , the stress in the film after deposition,  $R_{initially}$  and  $R_{after}$  the substrate radii of curvature before and after deposition respectively,  $E_s$  the Young's modulus and  $\nu_s$  Poisson's ratio of the substrate,  $t_s$  the substrate thickness and  $t_f$  the film thickness.<sup>[124]</sup>

## Chapter 4

# Diamond plates

Nanotechnology is an emerging field of research in which diamond is also being considered for nano-applications, i.e. diamond nanowires or nano-plates are promising materials for nanotechnological applications, such as field and thermionic emitters, nanophotonics and nanoelectromechanical system applications, due to a high Young's modulus and strength-to-weight ratio.<sup>[125,126]</sup> There is an interest for nanodiamond structures and devices but for most nanotechnological purposes, as-grown diamond nanostructures offer benefits over their top-down fabrication. The latter approaches are being used more, however, due to the lack of techniques that offer control over the morphology. So despite a large collection of interesting properties, such as high hardness, good thermal conductivity, biocompatibility, chemical hardness and the possibility for doping, control over the morphology and crystal orientation remains challenging. For nanocrystalline diamond, some properties are influenced by the crystallographic orientation, so a technique that offers some control during growth would be highly valuable. Chemical vapour deposition of diamond already is quite suited for this purpose, since the alpha parameter (see below) can be influenced by the growth parameters. Nevertheless, the most encountered diamond morphology is octahedral grains, although efforts have been made for the direct fabrication of diamond nanostructures.<sup>[127,128]</sup>



An interesting morphology that has only been reported by a limited number of researchers is the diamond plate structure, first discovered by Angus *et al.*<sup>[129]</sup> in 1992 and later confirmed by Chang *et al.*<sup>[130-132]</sup> both using microwave plasma enhanced CVD and very recently by Alexeev *et al.* using direct current discharge PECVD.<sup>[133]</sup> Although this morphology was previously referred to as diamond 'platelets', in this thesis it will be called 'plates' to avoid confusion with the nitrogen defect in single crystal diamond.<sup>[134]</sup>

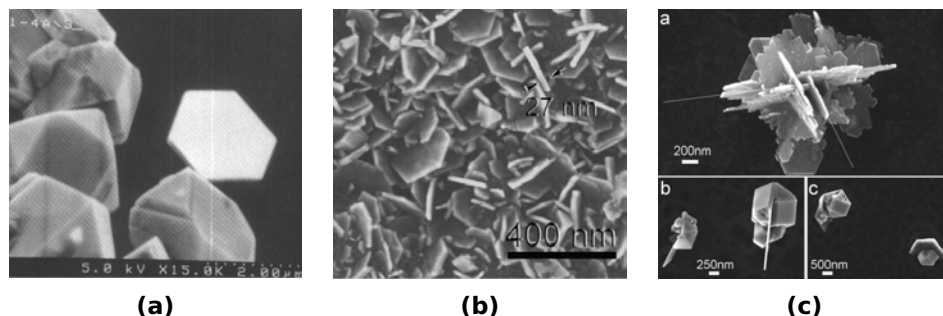


**Figure 4.1:** SEM images of diamond plates as reported by a) Angus<sup>[129]</sup>, b) Chang<sup>[131]</sup> and c) Alexeev<sup>[133]</sup> *et al.*

## Alpha parameter

The growth morphology is determined by the alpha parameter, i.e. the crystal shape is correlated to the ratio of growth rates in  $\langle 100 \rangle$  and  $\langle 111 \rangle$  directions:  $\alpha = v_{100}/v_{111} \cdot \sqrt{3}$ . Going from 1 to 3, the crystal shape changes from cube to cubo-octahedron to octahedron, which means the alpha parameter does not account for plate formation.

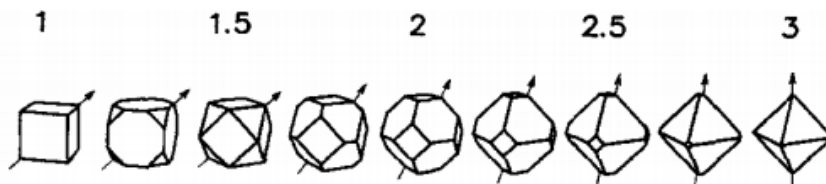


**Figure 4.2:** Idiomorphic crystal shapes for different values of the growth parameter  $\alpha$ . The arrows indicate the direction of fastest growth. Reproduced from<sup>[135]</sup>.

## 4.1 Re-entrant groove model

Angus *et al.* first reported the formation of hexagonally shaped plates, next to octahedral grains, during the first stages of growth.<sup>[129]</sup> As shown in figure 4.1a, the plates are approximately 2.5  $\mu\text{m}$  long and the thickness is much smaller, but was not reported. The mechanism behind the formation of these plates, i.e. the presence of stacking faults, is discussed without giving a possible reason for these stacking faults to occur. According to their findings and a model adopted from Hamilton and Seidensticker, re-entrant grooves ( $141.1^\circ$ ), originating from stacking faults, play a critical role for the growth of  $\{111\}$  faceted diamond crystals because they are preferred nucleation sites.<sup>[136]</sup> The simplest stacking fault is one layer of hexagonal diamond within a cubic crystal lattice, parallel to the  $\{111\}$  plane. Other stacking faults can consist of multiple adjacent layers of hexagonal diamond or multiple layers of hexagonal diamond separated by correctly stacked cubic layers. An intrinsic stacking fault consists of two adjacent layers of hexagonal diamond, while an extrinsic fault consists of two layers of hexagonal diamond separated by a cubic diamond layer. Hexagonally versus cubically stacked layers differ in their conformations, as shown in figure 4.3a and b. Cubic diamond stacking consists of adjacent chair conformations, while a stacking fault contains one or more layers in boat conformations. Once an intrinsic or extrinsic stacking fault is formed a re-entrant groove forms and continues to exist, as shown in figure 4.3c and d, because the addition of only two carbon atoms is required to complete every new layer, while for non faulted diamond three ad-atoms are needed for stable addition. The geometric nature of this re-entrant groove is self-regenerating, i.e. in every consecutive layer only two atoms are needed for the formation of a stable nucleation site. The re-entrant corner from a single stacking fault, in comparison, does not continue to exist but fills out to form a convex corner, as shown in figure 4.3e.

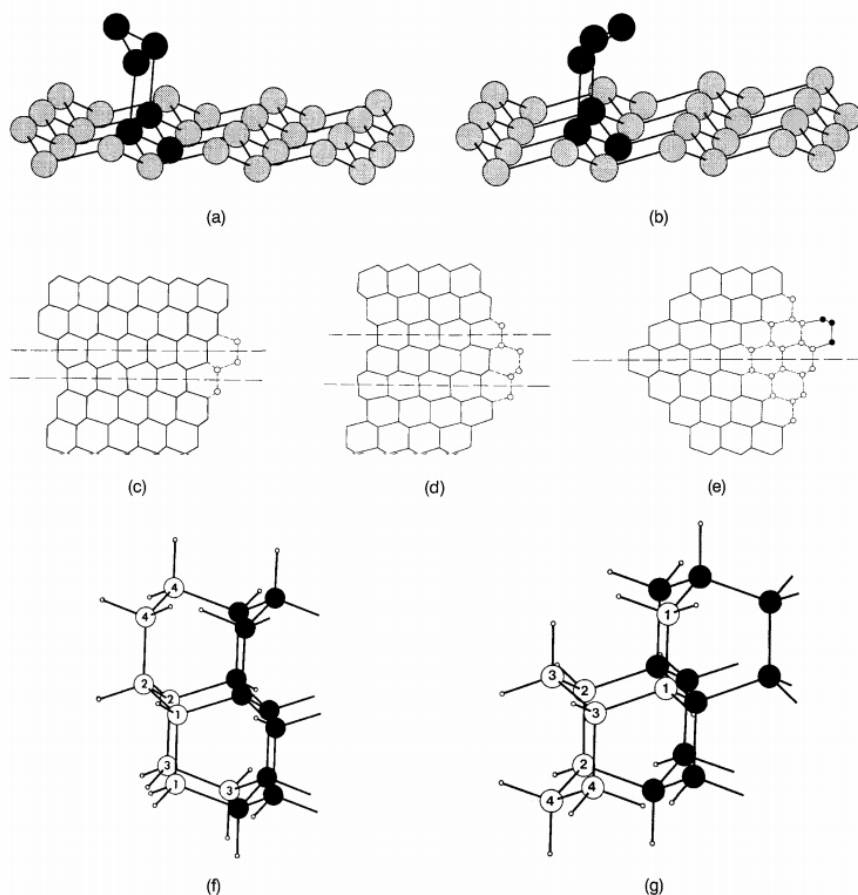


**Figure 4.3:** a) Correct and b) incorrect three-atom nucleus on a  $\{111\}$  surface. The six-membered ring that includes the three ad-atoms is in the chair or boat conformation respectively. c) Two adjacent stacking faults in the diamond-cubic lattice viewed in a  $[110]$  projection ("intrinsic" stacking fault). d) Two stacking faults in a diamond-cubic lattice with a layer of correct stacking in between, viewed along a  $[110]$  projection ("extrinsic" stacking fault). Addition of pairs of atoms at the re-entrant groove where the stacking fault intersects the surface is shown with dashed lines and open circles in (c) and (d). e) Single stacking fault viewed in a  $[110]$  projection. The re-entrant groove fills out to form a convex corner. Further growth requires a three-atom nucleation event on a smooth  $\{111\}$  surface, shown with filled atoms. f) Detail of (c) showing a sequence of two-atom addition events along intersection of "intrinsic" stacking fault with the surface. The filled atoms are in the original diamond lattice. Small circles represent hydrogen atoms. The filled atoms have the structure of a trans boat-boat bicyclodecane. g) Detail of two-atom addition events showing propagation of a re-entrant corner of the crystal. The filled atoms are in the diamond lattice. The small circles represent hydrogen atoms. The filled atoms have the structure of cis boat-boat bicyclo decane. [Source: <sup>[129]</sup>]

To explain why the addition of two ad-atoms will evolve faster than of three ad-atoms, the addition and removal rates need to be considered. An atom that is singly-bonded has a certain probability to leave again, but when another atom bonds to it, the probability of both atoms to leave is dramatically lowered. For sites at stacking faults, two atom addition is sufficient for stable nucleation, which has a higher probability than the consecutive addition of three atoms at  $\{111\}$  surfaces. However, once one stable nucleation site is formed at a  $\{111\}$  surface, the entire surface will grow by step flow, i.e. by means of atom attachment to the edge of the plane that arises from this nucleation site. Since the growth progresses in the plane of  $\{111\}$  surfaces, the available surface area increases and the probability for the formation of stable nucleation sites on top of these  $\{111\}$  planes increases as well. Eventually a hexagonal plate is formed due to the nature of a stacking fault. Each fault causes a  $60^\circ$  rotation about an axis normal to the  $\{111\}$  plane.

## 4.2 Sub-step model

In 2004 Chang *et al.* reported the deposition of diamond plates, as shown in figure 4.1b. In contrast to Angus *et al.*, where there was co-deposition of 3D diamond crystallites and plates, Chang *et al.* observed only diamond plates. The plates are about 30 nm thick and from a few hundreds of nanometres up to several micrometres long. They were deposited by microwave CVD on a nickel covered polycrystalline diamond sample grown on Si. It is stated that from side view high resolution TEM of diamond plate structures only a ridge side face structure is observed. So it is uncertain if the previous model can be applied to diamond plate growth, as there is no clear evidence of re-entrant grooves. It should be noted, however, that the side face structure has very low contrast in their HRTEM (as shown in figure 4.4) and that the crystal plane assignation can be interpreted differently, as shown by the red lines. Nevertheless, the sub-step model,

originally proposed by Ming *et al.* and adapted for diamond deposition by Chen *et al.*,<sup>[132,137]</sup> can still potentially account for the emergence of plate diamond structures.

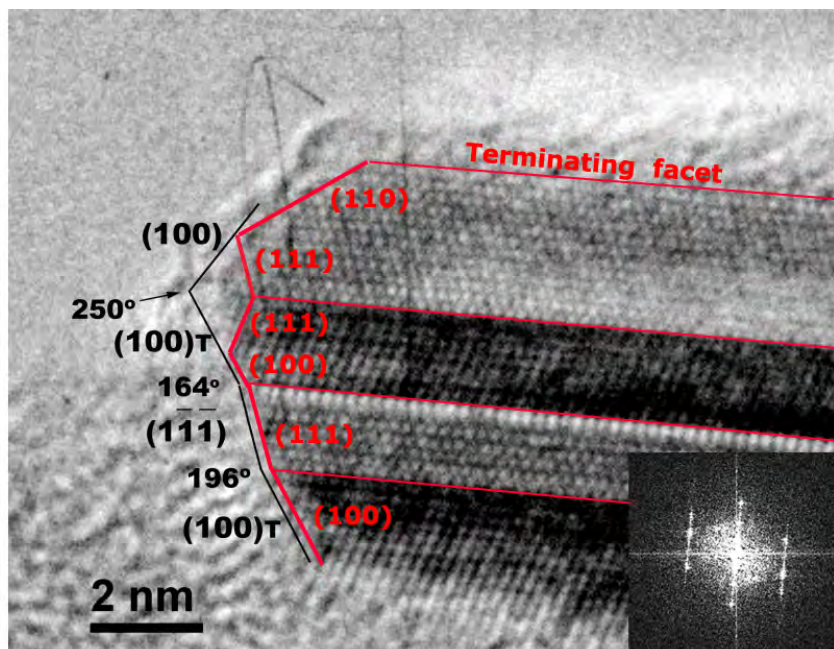


**Figure 4.4:** HRTEM image showing the fine structure of the side face structure of a plate. The black lines were introduced by Chen *et al.* to indicate the crystal facets at the ridge structure.[Reprinted from<sup>[132]</sup>] The designation of the crystal planes can be interpreted differently since the HRTEM images is blurry at the edge. The red lines show the interpretation made in this thesis which does not necessarily disclose the re-entrant groove model.

The sub-step model is described in figure 4.5 and again no explicit reason for its occurrence is postulated, but the existence of (multiple parallel) twins is of key importance. The different crystal planes, for instance  $\{111\}$  and  $\{100\}$  have different growth speeds, which gives rise to a ridge edge side face structure (e.g. in figure 4.5a). The sub-step model is based on the assumption that  $\{100\}$  faces grow faster than  $\{111\}$ , because there are more neighbours for ad-atoms which leads to a higher nucleation rate on  $\{100\}$ . The  $\{100\}$  faces will grow until the twin plane, i.e. ridge edge (figure 4.5c), where nucleation is preferred compared to flat  $\{111\}$  faces because again only two ad-atoms are necessary for a stable nucleus.

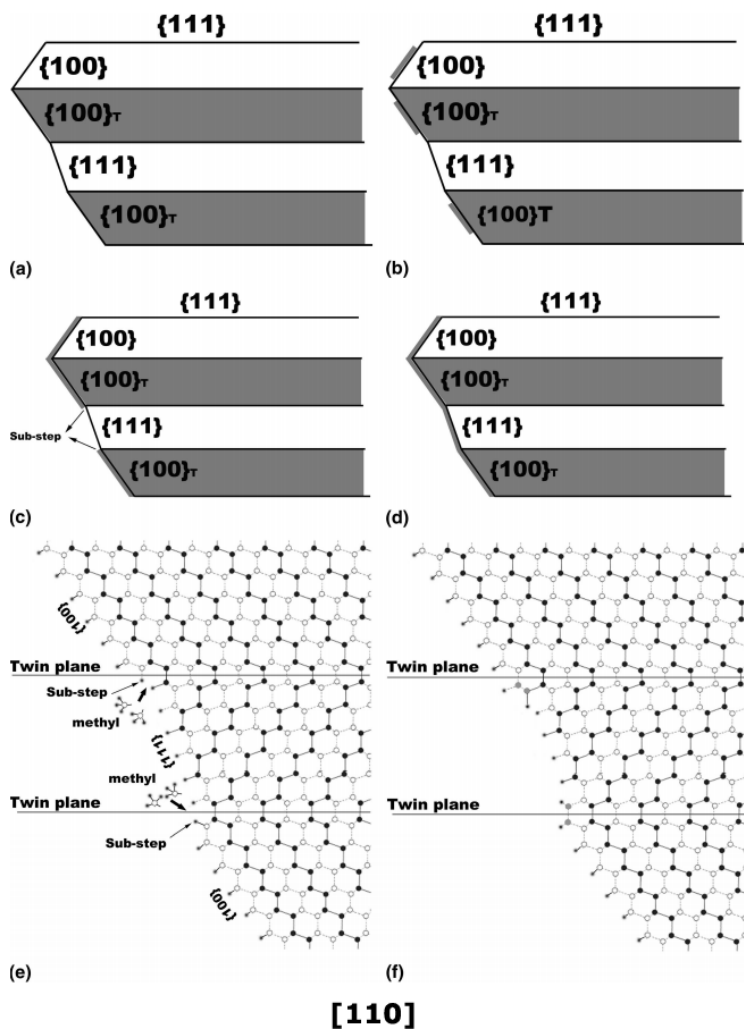


**Figure 4.5:** Schematic illustration showing lateral growth on the ridge edge by the sub-step model in the  $[110]$  viewing direction: a) Initial side face structure. b) Nucleation of a new layer on  $\{100\}$  faces. c) Emergence of sub-steps when propagation of the new layer reaches the twin edge. d) Extension of the new layer across the ridge edge (twin plane) due to favourable incorporation of ad-atoms into sub-step site to complete the growth of the whole layer in lateral direction. e) Atomic sketch showing the sub-step at the ridge edge projected on  $\{110\}$  plane. The foreign radicals (such as methyl) favourably incorporate into the sub-step sites. Small solid dots represent hydrogen atoms; open circles represent carbon atoms; and solid circles represent carbon atoms in different layers. f) Incorporation of two carbon atoms into the sub-step site. The new layer can then extend across ridge edge (twin plane) and further sustain the growth on  $\{111\}$  sector. [Reprinted from<sup>[132]</sup>]

Further growth proceeds along the  $\{111\}$  face to complete the layer, with the addition of only two atoms in every step to form a stable nucleus, which means this sub-step site is regenerating itself. The main reason  $\{111\}$  faces along the ridge edge grow is the sub-step site, which explains the lateral growth of the plates. The terminating  $\{111\}$  faces, i.e. the large top and bottom surfaces (indicated in figure 4.4), still require three ad-atoms for stable nucleation. Similar  $\{100\}/\{111\}$  ridge-and-trough side faces are known to occur for noble metals or silver halides.<sup>[138,139]</sup> After the adoption of the sub-step model to account for plate formation, the group of Chang *et al.* has done more work on the synthesis and characterization of diamond plates structures.<sup>[130,131,140,141]</sup> The deposition of diamond plates requires high temperature ( $> 1100$  °C) and low methane concentration ( $< 2$  %) and often a foreign material is present, such as Ni, Fe or Au and Ge. Both plates with  $\{111\}$  and  $\{110\}$  terminating or tabular faces have been synthesized. The most recent report of diamond plates was by Alexeev *et al.* in the beginning of 2016.<sup>[133]</sup> The plates obtained in their experiments are shown in figure 4.1c and are composed of stacked (111) diamond planes and TEM confirms the presence of planar stacking faults or twin boundaries in  $\{111\}$ . Multiple diamond plates intersect at about  $70.5^\circ$ , which corresponds to intersection angle between  $\{111\}$  planes in cubic crystal structures, and confirms the  $\{111\}$  nature. In addition, to explain the emergence of plates, high temperature and low methane concentration is believed to be of key importance, together with the re-entrant groove model.

### 4.2.1 Simulations

Monte Carlo simulations done by Sunkara have shown that while one stacking fault on parallel  $\{111\}$  planes leads to slowly growing triangular plates, two or more stacking faults lead to hexagonal plates.<sup>[142]</sup> Moreover, hexagonal plate development is in agreement with a kinetic and thermodynamic approach of modified Wulff constructions (a modelling tool

to predict the shape of nanoparticles) for twinned nanoparticles adopted by Ringe *et al.*<sup>[143]</sup> According to their model, a hexagonal plate can be obtained with fast  $\{100\}$  growth, compared to slow  $\{111\}$  growth, and enhanced twin growth, which means that all faces adjacent to the twin plane grow equally fast.

### 4.3 Occurrence of stacking faults

A plausible mechanism for the occurrence of stacking faults on  $\{111\}$  surfaces was described by Butler *et al.*<sup>[144]</sup> in 2008. In order to create a stable nucleus on  $\{111\}$  at least four carbon atoms need to be bonded to this  $\{111\}$  surface and to each other. In the first step a three-atom bridge is formed between adjacent carbon atom sites on the  $\{111\}$  surface by subsequent abstraction of atomic hydrogen and reversible carbon adsorbate additions (as described section 2.2). This three-atom bridge rapidly isomerises between the boat and chair conformation (see figure 4.6), because they are similar in energy, until it is locked in either of the two positions by the addition of a fourth carbon, as shown in figure 4.7. The nucleus formed has four bonds to the diamond surface and is thus very stable. Because of the similarity in energy, the created nucleus has almost 50 % chance of being a stacking fault.

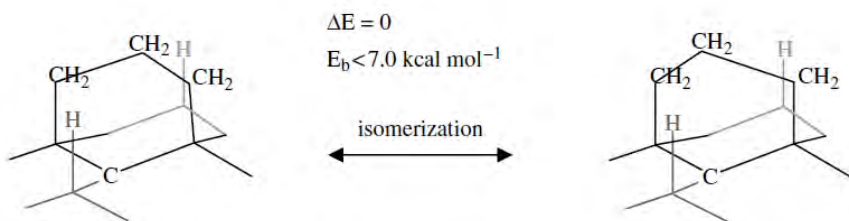


**Figure 4.6:** Representations of a local region of the  $\{111\}$  surface with various adsorbates bonded to the surface carbons showing the rapid isomerisation of the three-atom bridge between the chair (normal stacking) and boat (stacking fault) forms of the six-atom ring. Reaction enthalpy changes are shown in eV ( $\text{kcal mol}^{-1}$ ). [Reprinted from<sup>[144]</sup>]



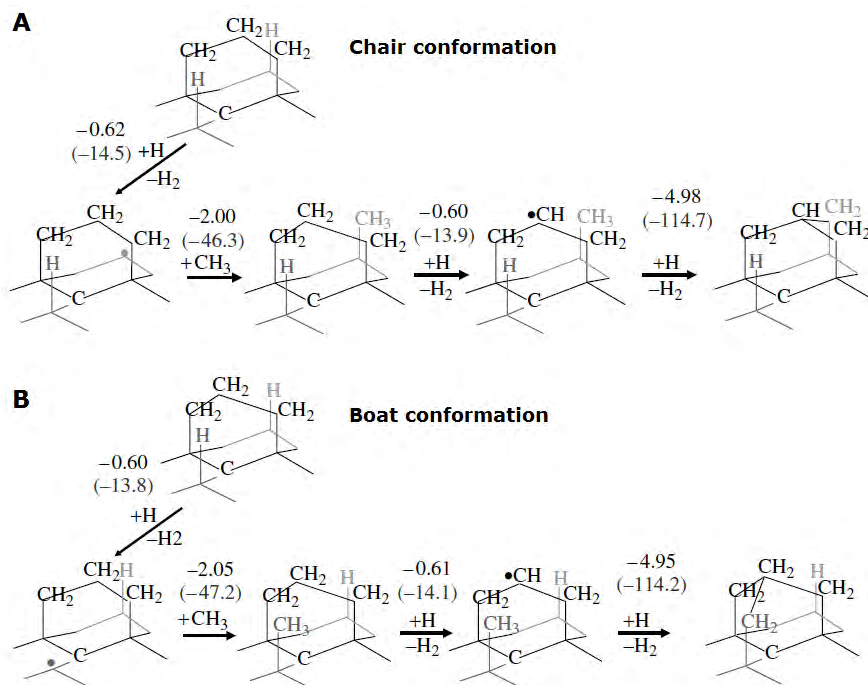


**Figure 4.7:** Representations of a local region of the  $\{111\}$  surface with various adsorbates bonded to the surface carbons showing the formation of the stable four-atom island, or nucleation of the next layer of growth on  $\{111\}$  surfaces resulting in a) normal stacking and b) a stacking fault. Reaction enthalpy changes are shown in eV ( $\text{kcal mol}^{-1}$ ). [Adapted from<sup>[144]</sup>

## **Part II**

# **Results and discussion: Membranes**



## Chapter 5

# Diamond membranes on glass

The fabrication and application of nanocrystalline diamond (NCD) membranes is an interesting and developing research topic. Kummer *et al.* showed that thin conductive diamond films can be used for in-situ monitoring of the intensity of soft X-ray beams.<sup>[145]</sup> Williams *et al.* demonstrated tuneable lenses out of boron-doped NCD (B:NCD) films.<sup>[146]</sup> Even 300 nm thick single crystal diamond membranes were reported for use as optical resonators for colour centres.<sup>[147]</sup> Additionally, research of pressure sensors based on piezoresistive materials has been carried out extensively and is well described in literature.<sup>[148]</sup> Piezoresistive sensors are being used for industrial and for biomedical applications, e.g. for the measurement of blood pressure.<sup>[149]</sup> The gauge factor, a measure for the relative change in electrical resistance compared to the applied mechanical strain, depends on the nature on geometrical properties of the piezoresistive material. In order to maximise the sensitivity of pressure sensors we need to increase the gauge factor as much as possible. NCD diamond thin films typically have gauge factors of up to 30, which is comparable to that of silicon,<sup>[150]</sup> and moreover, they are suitable for use in harsh environments

which makes them ideal candidates for pressure sensors.<sup>[146,151]</sup>

## 5.1 Fabrication of NCD membranes on glass

The creation of a membrane in the centre of a Hall bar pattern occurs in various steps, as described in figure 5.1. Prior to the fabrication of the membranes, the glass substrates are cleaned with the standard cleaning procedures, seeded from a water based colloidal suspension via spin coating and grown either intrinsically or B-doped in an ASTeX type reactor (step 1, figure 5.1). Although the NCD layers are compressed, delamination from the substrate surface was not observed to occur. Then a Hall bar pattern is created in the diamond film by the following steps: application of positive photoresist, subsequent sputtering of an approximately 200 nm thick aluminium layer, lift-off of the resist with acetone and finally oxygen plasma treatment to etch away the exposed diamond (step 2). The remaining aluminium layer is then removed with hydrogen chloride, leaving behind a patterned NCD layer on glass. The Hall bar pattern (see figure 5.2) is commonly used for Hall effect<sup>1</sup> measurements, but can be used for electrical resistance measurements of a particular section of a sample by clever positioning of the contacts. In this particular case, the measurement area is limited to 1 mm<sup>2</sup> containing the membrane in the centre of the created pattern.

In order to make a diamond membrane a second photolithography step is needed: on the backside of the sample a dot is patterned in the centre of the Hall bar diamond pattern present on the top side. Applying this pattern with negative photoresist and subsequent development exposes a circle in the very centre of the glass substrate (step 3 and 4). In the last two steps the glass substrate is etched away with HF. The etching process needs to be performed in two steps, because there are impurities present in the glass substrate that form non-soluble fluorides which create a thick

---

<sup>1</sup>The occurrence of a voltage perpendicular to the applied current through a conductor upon application of a magnetic field also perpendicular to the applied current.

crust causing the membrane to break in case of continuous etching to the diamond film. The etching process is stopped after about 500 microns ( $\pm 70\%$ ) of glass is etched away (step 5) and the photoresist can be peeled off. Then the insoluble fluorides are dissolved in a HCl:H<sub>2</sub>O (1:1) mixture after which the remaining thin glass layer is completely etched away and a diamond membrane is formed (step 6).

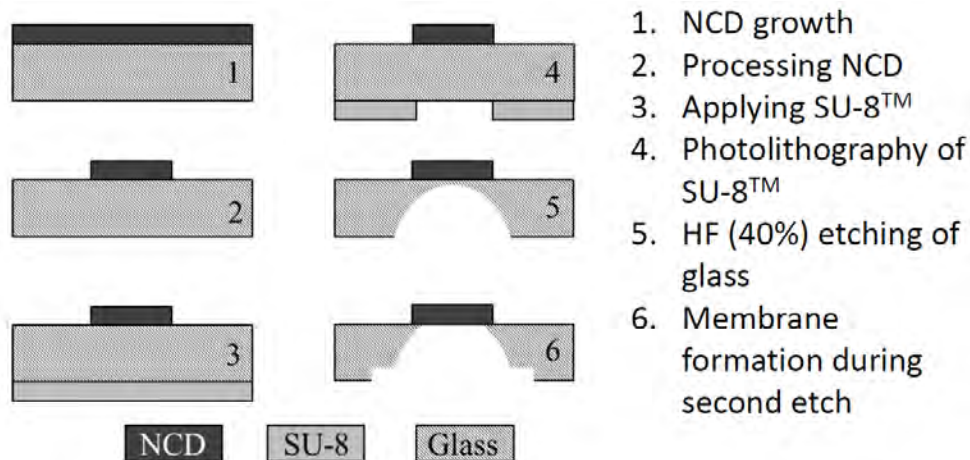


**Figure 5.1:** Step-wise representation of the implemented fabrication method for NCD membranes on glass.



**Figure 5.2:** Depiction of a nanocrystalline diamond film on glass patterned into a Hall bar structure.

Prior to measuring, ohmic Ti/Al contacts are sputtered onto the Hall bar structure by the use of a mask. Then the sample is mounted in a home-built measuring set-up (see figure 5.3a), which is designed to inflate mem-

branes with positive differential pressures at ambient conditions. During inflation, four-point resistance measurements were performed with a Keithley 2400 multimeter by application of a fixed DC current. As shown in figure 5.3b, the DC current is applied from contact C1 to C2, and the voltage difference is measured between C3 and C4. In order to eliminate temperature effects caused by the current flow, measurements were started only after the resistance reached a stable value.

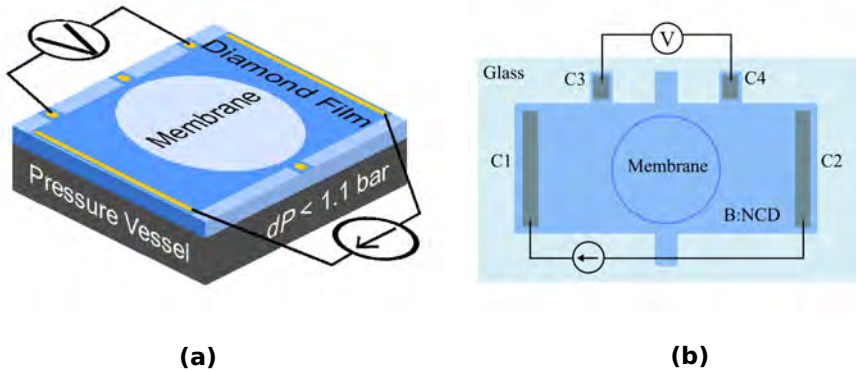


**Figure 5.3:** Schematic representation of a) the home-built measurement set-up: the membrane is bulged via the pressure vessel underneath during which electrical measurements are performed, and b) the top view of a B:NCD membrane in the middle of a Hall bar structure with wiring for electric measurements.

## 5.2 Piezoresistive effect of NCD membranes

Piezoresistivity is the change of an object's electrical resistance under applied mechanical strain. To quantify a material's piezoresistivity, often the gauge factor is used. The gauge factor is a measure for the relative change in electrical resistance compared to the applied mechanical strain, and it depends on the nature of geometrical properties of the piezoresistive material.

$$\gamma = \frac{dR}{R} \frac{1}{\epsilon} = (1 + \nu) + \frac{dp}{\rho} \frac{1}{\epsilon} \quad (5.1)$$

Here,  $dR$  is the resistance change of a material, induced by an applied strain ( $\epsilon$ ),  $R$  is the initial resistance,  $\nu$  is Poisson's ratio, and  $\rho$  is the resistivity. For diamond  $dR/R$  can be approximated by  $d\rho/\rho$  according to Imboden *et al.*<sup>[152]</sup>, since the first term of equation 5.1 is negligible compared to the latter. Furthermore the change in resistance as function of the applied differential pressure is linear, e.g. the response of a 200 nm thick B:NCD membrane with a diameter of 550 micrometre of S-AF45 glass in figure 5.4. Because of this piezoresistive effect it is possible to use di-

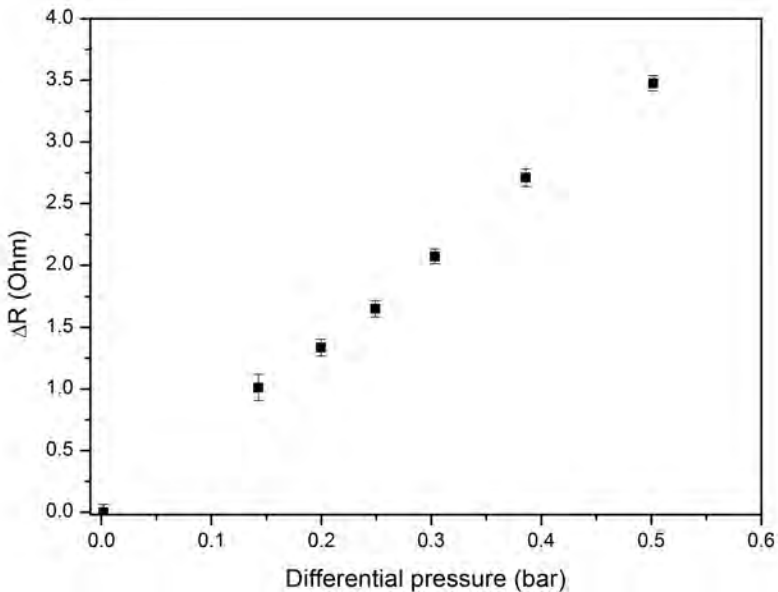


**Figure 5.4:** Change in resistance as a function of applied differential pressure for a 200 nanometre thick B:NCD membrane on S-AF45 glass with a diameter of 550 micrometre.

amond for pressure sensing purposes. Currently, state-of-the-art piezoresistive sensors consist of a non-piezoresistive membrane or diaphragm to which piezoresistive components are attached, e.g. boron-doped nanocrystalline diamond films or structures on Si diaphragms<sup>[153,154]</sup>. In the case where the membrane itself is a piezoresistive material, the number of fabrication steps can be reduced, for example diamond membranes of



a few micrometres thick have been demonstrated<sup>[153,155]</sup>. Especially with the use of an insulating substrate and a conductive diamond layer, very thin and very sensitive systems can be made because the need for an insulating carrier material is omitted. Since diamond has a high Young's modulus and a high fracture strength compared to other materials, much thinner films can be made, which require a smaller differential pressure for a significant response, i.e. a higher value for the gauge factor is obtained. Moreover, the benefits of using glass as a carrier substrate are undeniable, 1) it allows fairly easy processing because it is optically transparent and therefore easy to align the patterns on the top and back side, and 2) glass is a very resistant material which allows the sensors to be used in harsh, e.g. acidic, condition.

### **5.2.1 Piezoresistivity of NCD:H membranes**

The origin of the surface conductivity of hydrogen-terminated diamond has been discussed in section 1.4.1. A deeper insight into the electronic transport properties of NCD:H can be obtained by the investigation of the piezoresistive effect. This part of the research was conducted in collaboration with S.D. Janssens. 350 nm thick hydrogen-terminated nanocrystalline diamond films were grown onto CE2000 glass substrates and etched into a Hall Bar structure. Subsequently a membrane with a diameter of 328  $\mu\text{m}$  was created by deep etching of the glass substrate. Electrical 4-point measurements were performed during inflation and deflation experiments (figure 5.5). A piezoresistive effect and a linear relation between  $dR$  and  $dP$  (2762  $\text{k}\Omega/\text{bar}$ ) is clearly observed after several bulging experiments, as shown in figure 5.6a. Since there are no wrinkles present, probably because the diamond film becomes too rigid at a certain thickness, it is possible to obtain the gauge factor from equation 5.1.

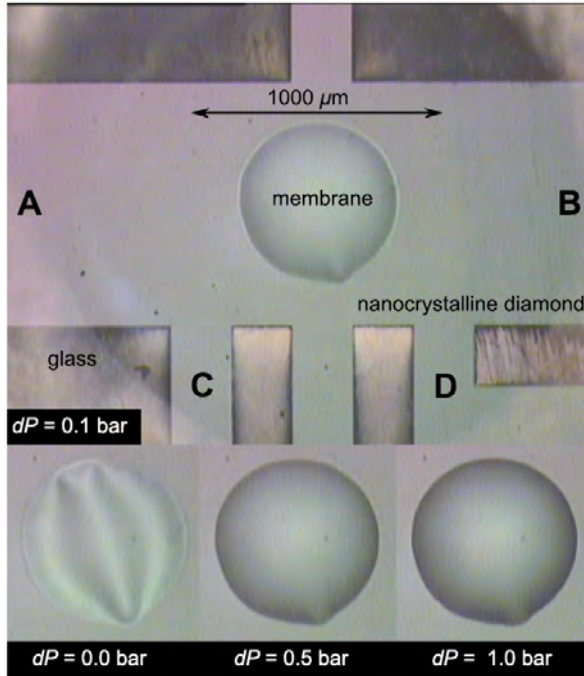


**Figure 5.5:** Bulging of the hydrogen-terminated nanocrystalline diamond membrane under differential pressures of 0.0, 0.1, 0.5, and 1.0 bar. To measure the piezoresistive effect, a fixed current is applied from A to B and the electrical potential change is measured between C and D.

First the strain in the membrane ( $\epsilon$ ), induced by a differential pressure  $dP$ , needs to be determined. This is done by the use of Cabrera's equation<sup>[156]</sup>

$$dP = \frac{4w_0t}{r^2} \left( \sigma_0 + \epsilon \frac{E}{1-\nu} \right) \quad (5.2)$$

with  $w_0$ , the maximum deflection of the membrane;  $t$ , the membrane thickness;  $r$ , the membrane radius;  $E$ , the Young's modulus of the NCD:H film;  $\sigma_0$ , the residual stress in the membrane and  $\nu$ , Poisson's ratio and

$$\epsilon = \frac{2w_0^2}{3r^2}. \quad (5.3)$$

Since there is a very small change in resistance upon straining, i.e.  $R_{HB}(\sigma = 0) \approx R_{HB}(\sigma \neq 0)$  with  $R_{HB}$ , the resistance of the Hall Bar structure, and  $dR/dP$  is constant for a broad range,  $\sigma_0$  can be approximated as zero. In

addition, for diamond  $\nu = 0.069$  and is negligible compared to one.<sup>[125]</sup> Therefore, it is possible to express equation 5.2 as

$$w_0 = \left( \frac{3r^4 dP}{8tE} \right)^{\frac{1}{3}} \quad (5.4)$$

Substituting equation 5.4 in 5.3 eliminates  $w_0$  and leads to the expression for the gauge factor used in this work

$$\gamma = \frac{dR}{R} \frac{3}{2} \left( \frac{8tE}{3rdP} \right)^{\frac{2}{3}} \quad (5.5)$$

$R$ , the resistance of a membrane in the middle of a Hall bar structure, is approximated as  $2R_{HB}/\pi$  (see section 5.2.2),  $dR = 27 \pm 2\text{k}\Omega$  at  $dP = 1$  bar and by comparing similar NCD layers,  $E \approx 800$  GPa or more.<sup>[157]</sup> Using the latter values, a gauge factor of 35 for the surface conductive NCD:H membrane is obtained.

The pressure is cycled between bulging, with a maximum pressure of 1.04 bar, and deflation. The change in resistance,  $dR$ , is a superposition of two effects. As shown in figure 5.6b, with a change in pressure there is a very fast, quasi instant change in resistance  $dR_i$  followed by a time-dependent change  $dR_t$ . These two contributions originate from two separate mechanisms, i.e.  $dR = dR_i + dR_t$ . In order to explain the electronic transport properties of polycrystalline materials, in this case NCD:H, a one-dimensional model in which the grains and grain boundaries are approximated as resistors in series, as shown in figure 5.7 is sufficient.<sup>[61,158]</sup> The model considers the grains as a line of squares, separated by grain boundaries and the resistance consists of the contributions of both the grains and the grain boundaries. With the use of this model the change in resistance,  $dR$ , can be explained. Part of the resistance is induced by charge carrier transport in the grain boundaries, and therefore  $dR_i$  can be assigned to the piezoresistive effect of the grain boundaries. The grain boundaries are known to be able to conduct current.<sup>[158]</sup> They contain mainly hydrogenated amorphous carbon (a-C:H) and are several nanometres long.<sup>[42,159,160]</sup> In ad-

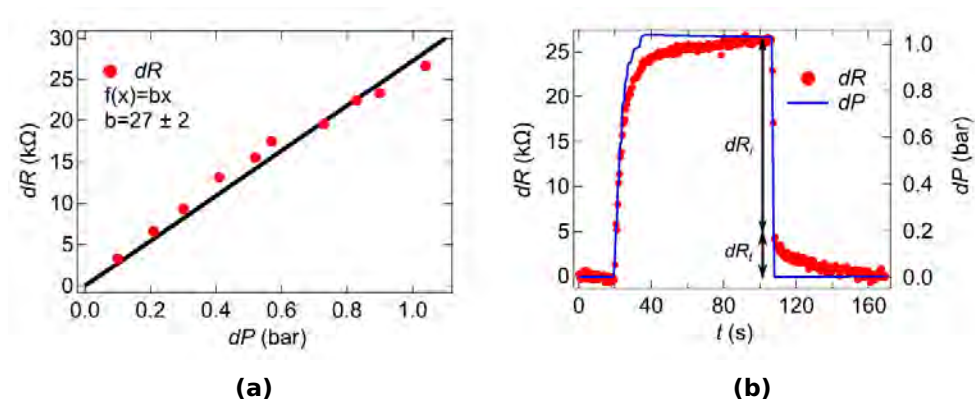


**Figure 5.6:** a) Resistance change as a function of differential pressure for several bulging experiments and b) Resistance change (left axis) of the NCD:H membrane, induced by a differential pressure (right axis), presented as a function of time.

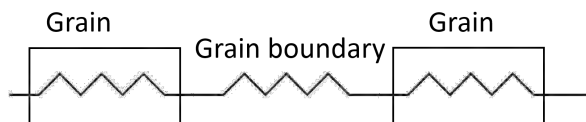


**Figure 5.7:** One-dimensional model with the grains and grain boundaries approximated as resistors in series.

dition, they have a lower Young's modulus than diamond. Therefore the piezoresistive effect of the grain boundaries is compared to that of a-C:H. The gauge factor of NCD:H is calculated to be 35, which is in the range of gauge factor values for a-C:H (16-81),<sup>[161]</sup> and in agreement with the hypothesis above. For sensing applications the characteristics of the grain boundary material, controlled by the deposition parameters, can be optimized.<sup>[157]</sup> The time-dependent component of  $dR$  is attributed to the interaction of the surface conducting grains with the grain boundaries via a trapping mechanism, similar to one which explains electronic transport in polycrystalline silicon.<sup>[162,163]</sup> The mechanism is based on the entrapment of charge carriers at trap states in the grain boundaries. During trapping, the formerly neutral trap states become charged, which creates a potential barrier ( $V_b$ ) at the interface of the grain boundaries and grains. This potential barrier has a certain width ( $W$ ), which the charge carriers have to overcome, thereby increasing the resistivity of the material. The potential

barrier can be described by

$$V_b = \frac{qN_dW^2}{2e} \quad (5.6)$$

with  $q$ , the elementary charge,  $\epsilon$ , the permittivity of a grain, and  $N_d$ , the doping concentration of the material.<sup>[163]</sup> For NCD:H,  $N_d$  is the carrier density and  $\epsilon$  is the permittivity of SCD:H. If we assume that the number of traps is twice the number of charge carriers and express the barrier width as

$$W = \frac{Q}{2N_d} \quad (5.7)$$

with  $Q$ , a trap state density at a fixed energy level,<sup>[162]</sup> which leads to

$$V_b = \frac{qQ^2}{8N_de} \quad (5.8)$$

At constant temperature one can write that  $R \propto \exp(eV_b/kT)$ .<sup>[163]</sup> Here,  $k$  is Boltzmann's constant,  $T$  is temperature and for small changes in  $V_b$

$$dR \propto dV_b \quad (5.9)$$

which indicates that a small change in  $V_b$ , induced by straining NCD:H, will give rise to a piezoresistive effect.

To explain, we consider the variables  $Q$  and  $N_d$  in equation 5.8. First the effect of straining NCD:H on  $N_d$  is discussed: in a single grain (SCD:H) the band gap narrows when it is strained because the electron states from surface H atoms decrease, which shifts the conduction band minimum toward the valence band.<sup>[164]</sup> A less wide band gap will in turn lead to an increase of charge carriers.<sup>[41]</sup> An increase of the carrier density would increase the surface conductivity and second, according to equation 5.8, lower  $V_b$  at the grain boundaries which leads to a further increase of the surface conductivity. It is important to note that a decrease of  $V_b$  would be valid in our results because the charge carriers are abundant, which means that the amount of non-trapped carriers remains high enough to

conduct current.<sup>[163]</sup> This assumption is true since the doping concentration,  $N_d$ , is almost as high for NCD:H as for SCD:H.<sup>[158]</sup> However, in these experiments, the surface conductivity decreases, i.e.  $dR > 0$  upon straining, so an increase of  $N_d$  by straining NCD:H cannot be the main cause of the piezoresistive effect in NCD:H.

Another parameter in equation 5.8 is the trapping state density,  $Q$ , which causes an increase in the resistivity with the appearance of more trapping states. This means that trapping states are generated when the grain boundaries are being strained, i.e.  $dR_t$  can be explained by an exponential time-dependent increase of the potential barrier due to the a corresponding increase of charge carrier trapping during straining of NCD:H. In addition, as mentioned before, trapping of charge carriers at neutral trap states at the surface of a grain, induced by straining, is also a possible mechanism to explain  $dR$ .<sup>[165]</sup>

### **5.2.2 Piezoresistivity of B:doped NCD membranes**

In collaboration with S.D. Janssens, B:NCD membranes of a few hundred nanometres thick were made and tested as pressure sensors in the scope of this thesis.<sup>[151]</sup> A 100 nm thick NCD layer was grown on a S-AF45 substrate and covered with a 50 nm B:NCD layer. The linear piezoresistive effect can be expressed as  $dR/dP = 27,3 \pm 0,1 \Omega / \text{bar}$ . However, as shown in figure 5.8, the fabricated membranes are wrinkled, which complicates strain calculations.

The strain is usually determined by finite element analysis or derived from the height of a bulged thin film, as proposed by Tsakalakos.<sup>[166,167]</sup> Both methods are based on the determination of the Young's modulus of the membrane by bulging experiments. The average membrane strain as function of the applied pressure is then used to calculate the gauge factor. For wrinkled membranes, there is, however, no reliable way to determine the Young's modulus and thus the gauge factor.<sup>[167]</sup> Therefore this work is limited to an indirect evaluation of the piezoresistive effect, i.e. the rel-

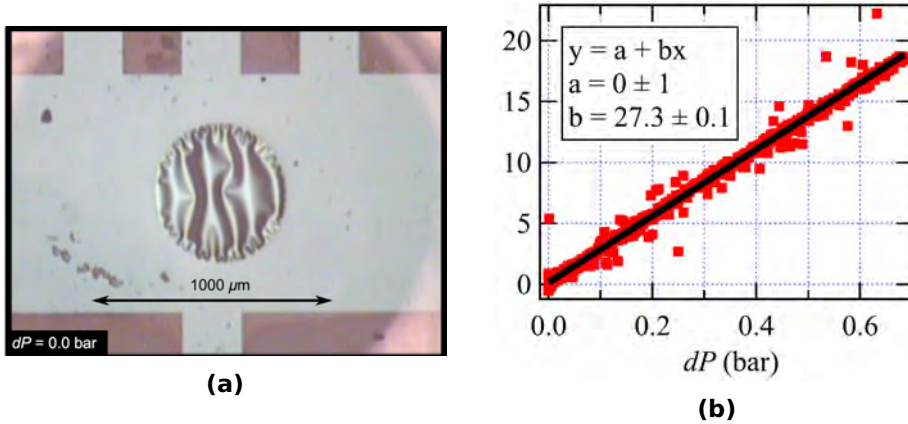


**Figure 5.8:** a) Top view of a 150 nm thick nanocrystalline diamond membrane, fabricated on Schott AF45 glass. The membrane has a diameter of roughly 555 micrometre and is positioned in the middle of a Hall bar structure. b) The change in resistance of the Hall bar structure, as a function of the differential pressure for the membrane in (a).

ative change of the resistance as function of the applied differential pressure. The resistance is assumed to be homogeneous over the diamond membrane, which allows for the division of the membrane into infinitesimally small rectangles, as shown in 5.9.

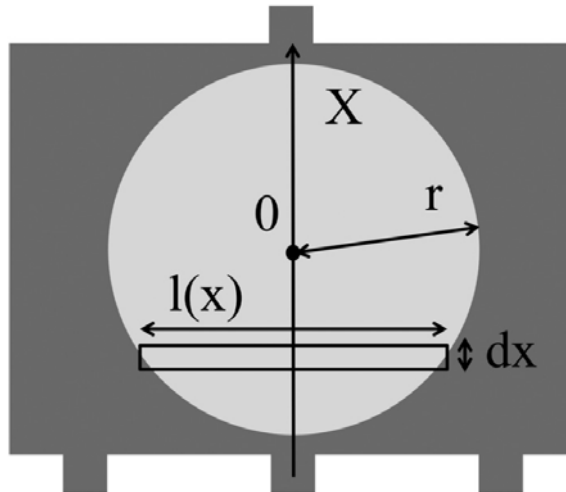


**Figure 5.9:** Sketch of a membrane with radius  $r$ , in the middle of a Hall bar structure. The membrane can be divided into an infinitesimal amount of rectangles with length  $l(x)$  and width  $d(x)$ .

The length ( $l$ ) of one rectangle is determined by Pythagoras:

$$l(x) = 2 \sqrt{r^2 - x^2} \quad (5.10)$$

in the case where the x-axis originates from the centre of the membrane. The conductance of one rectangle ( $dG$ ) can be expressed as

$$dG(x) = \frac{t}{\rho l(x)} dx = \frac{t}{2\rho \sqrt{r^2 - x^2}} dx \quad (5.11)$$

with  $\rho$  the resistivity (38 m $\Omega$  cm) and  $t$  the thickness (50 nm) of the doped layer. The total conductance of the membrane follows from the integration over all rectangles

$$G = \int_{-r}^r \frac{t}{2\rho \sqrt{r^2 - x^2}} dx = \frac{\pi t}{2\rho} \quad (5.12)$$

Thus the resistance of the membrane in non-bulged state equals  $R = \frac{2\rho}{\pi t}$ , i.e. a value of 4.8 k $\Omega$  for the diamond membrane.  $R$  is found to be independent of the membrane size for a circular membrane, and similar conclusions have been found for squares ( $R_{sq}$ ) with a fixed thickness,  $R_{sq} = \frac{\rho}{t}$ . The relative change in resistance, i.e. the recorded resistance difference over the calculated resistance, as function of applied differential pressure is approximately 0.6 % bar $^{-1}$ .

### 5.3 Pressure sensitivity of wrinkled B-doped NCD membranes

In order to maximise the sensitivity of pressure sensors the gauge factor should be as high as possible. The underlying substrate affects the properties of the resulting diamond film since the amount of stress in the film is highly dependent on the differences in thermal expansion coefficients between the diamond and the substrate. In the next sections, the influence of the size of the membranes, the boron doping level and of the substrate



material, and more specifically of its thermal expansion coefficient, on the sensitivity of the resulting B:NCD membranes will be investigated. For this purpose, films with different doping concentrations and different sizes were grown onto two different types of borosilicate glass, Schott AF45 (S-AF45) and Corning Eagle 2000 (CE2000). Characterization was done by scanning electron microscopy (SEM), Raman spectroscopy and laser scanning microscopy; and the results were compared with respect to the sensitivity of the membranes. The difference in thermal expansion coefficient causes a difference in stress in the diamond films upon cooling after growth. Laser scanning micrographs show that this stress is directly observable by the number of wrinkles present in the membranes, and that it influences the sensitivity of the membranes to pressure differences.

### 5.3.1 Pressure sensitivity

In order to produce pressure sensors that can compete with commercially available silicon sensors, it is important to reach high sensitivities. For this study, three types of membranes were prepared on two types of glass (S-AF45 and CE2000) to illustrate their typical behaviour. A summary is given in table 5.1.

**Table 5.1:** Summary of the membranes fabricated for this research.

Sample Code	B concentration B atoms · cm <sup>-3</sup>	Substrate material	Diameter μm	Sensitivity mΩ · Ω <sup>-1</sup> · bar <sup>-1</sup>
A	8 · 10 <sup>21</sup>	S-AF45 glass	280	0.52 ± 0.04
B	8 · 10 <sup>21</sup>	S-AF45 glass	550	1.13 ± 0.05
C	8 · 10 <sup>21</sup>	CE2000 glass	560	1.73 ± 0.02
D	8 · 10 <sup>21</sup>	CE2000 glass	800	2.40 ± 0.09
E	5 · 10 <sup>21</sup>	S-AF45 glass	130	0.58 ± 0.04
F	5 · 10 <sup>21</sup>	S-AF45 glass	400	2.03 ± 0.04

The relative change in resistance of the samples is determined as function of applied differential pressure. An increase of the applied differential pressure causes bulging and stretching of the NCD membrane (figure 5.10). A maximum differential pressure of 0.8 bar was applied to ensure

that no damage was caused to the membranes. After local removal of the substrate, the membranes are clearly wrinkled. The wrinkles become less pronounced upon the bulging of the membrane. After deflation the original wrinkle pattern reappears entirely both around the circumference and in the central part.

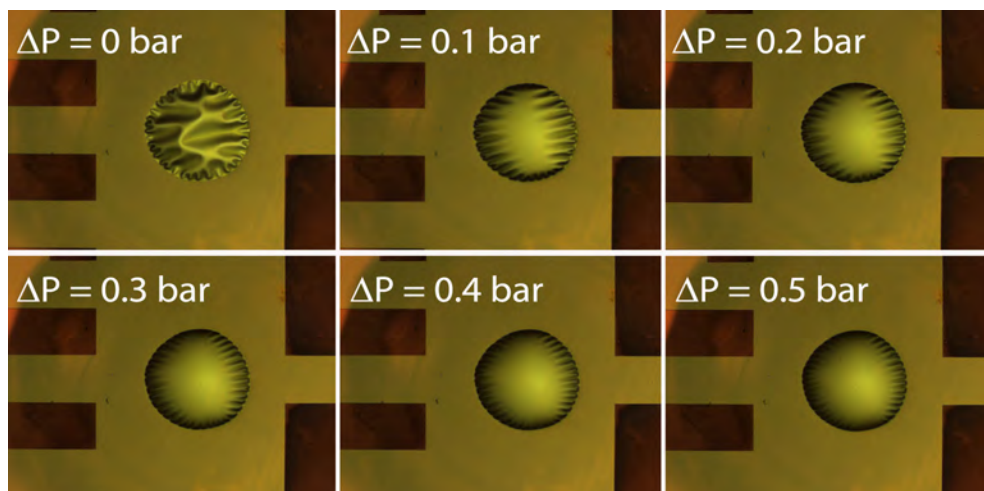


**Figure 5.10:** Optical images of sample C upon increase of the applied differential pressure. From top left to bottom right the differential pressure is 0, 0.1, 0.2, 0.3, 0.4, 0.5 bar respectively.

As expected, based on the piezoresistive effect, the resistance increases upon bulging of the membrane (figure 5.11).<sup>[151]</sup> For hydrogen-terminated nanocrystalline diamond (NCD:H) the piezoresistive increase is reasoned to originate directly from strain-induced changes in the resistivity of the grain boundaries.<sup>[168]</sup> For B:NCD membranes however, the influence of the grain boundaries on this increase in resistance remains unclear. Turner *et al.* showed that boron dopant atoms are incorporated to the same extent both in the diamond grains and in the grain boundaries.<sup>[42]</sup> In the grains, boron is incorporated substitutionally within the diamond lattice, while in the grain boundaries boron atoms are surrounded by amorphous carbon. What the exact influence of both types of boron incorporation on the conductivity and piezoresistivity of B:NCD is, remains a question, although Janssens *et al.* already showed that very small variations in boron

incorporation and number of grain boundaries are detectable by electric transport measurements.<sup>[61]</sup> In order to obtain a universal method of quantification for the piezoresistive effect, the pressure sensitivity  $S$ , was determined using the formula,

$$S = \frac{\Delta R}{R} \cdot \frac{1}{\Delta P} \quad (5.13)$$

where  $R$  is the resistance and  $\Delta P$  the change in differential pressure.<sup>[169]</sup> The resistivity of the samples depends on the measurement conditions, e.g. the state of the contacts, and is in the range of 1 to 17 k $\Omega$  for our samples. The obtained values for the relative change in resistivity were measured multiple times over a period of a month and have proven to be reproducible, although the absolute resistance varies with the state of the contacts. Other factors like exact grain structure and doping level may also play a role. Due to this variation in absolute resistance, when multiple samples are compared, the relative resistance was measured, which is a reproducible quantity. For the four membranes (A,B,C and D) studied in figure 5.11, the estimated boron content, as determined from Raman spectroscopy is  $8 \cdot 10^{21} \text{ cm}^{-3}$ , a value well over the Mott transition, rendering these films effectively into semi-metallic conductors.<sup>[170]</sup>

### **Substrate dependence of the sensitivity**

It is extremely difficult to produce membranes with the exact same diameter because the etch rates of the glasses are only estimates, influenced by local impurities, and once the diamond layer is reached, the membrane radius increases very fast. To assess the influence of the substrate on the sensitivity of the membrane, two membranes with comparable size, 550  $\mu\text{m}$  diameter and 560  $\mu\text{m}$  diameter on S-AF45 and CE 2000 glass (samples B and C), respectively, were fabricated and the relative change in resistance was compared (figure 5.11). With a change of the glass substrate from S-AF45 to CE2000, the sensitivity increases by 55%.

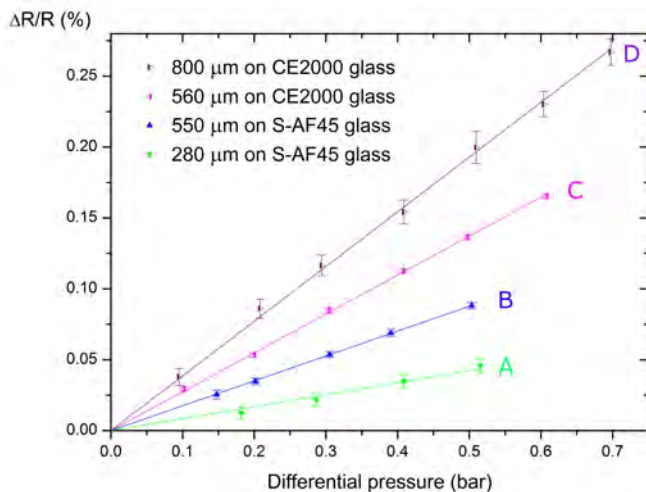


**Figure 5.11:** Relative change in resistance as a function of applied differential pressure for sample A, B, C and D.

This increase is attributed to the difference in stress in the resulting film caused by the aforementioned difference in thermal expansion coefficient of the two types of glass with respect to the thermal expansion coefficient of the diamond film. Wur and Davidson reported a similar dependence of the piezoresistivity of microcrystalline diamond films on the host substrate.<sup>[171]</sup> Depending on whether the thermal expansion coefficient of the underlying substrate is smaller or larger than that of diamond ( $1 \cdot 10^{-6} \text{ } ^\circ\text{C}^{-1}$ ) tensile or compressive stress, respectively, forms in the NCD film. The thermal expansion coefficients of S-AF45 glass is higher than that of CE2000 glass which leads to a higher amount of compressive stress in NCD layers grown on S-AF45 glass. This means that when the membrane is formed upon release of the substrate, a more compressed layer will have more surface area than a less compressed layer for the same hole diameter etched in the glass substrate. So higher compressive stress leads to larger membrane area and thus lower sensitivity, when the membrane is formed upon release of the substrate. For two membranes of 550  $\mu\text{m}$  diameter, the increase in surface area is about 150  $\mu\text{m}^2$  larger on S-AF45

than on CE2000. This area is calculated based on the expected size of the glass substrates at elevated temperature due to their thermal expansion coefficients. For instance, for a membrane of 550  $\mu\text{m}$  diameter on S-AF45 glass, the expected radius at 550  $^{\circ}\text{C}$  ( $R_f$ ) is:

$$R_f = R + \Delta R = R + \alpha \cdot R \cdot \Delta T = 275 \cdot (1 + 4.5 \cdot 10^{-6} \text{C}^{-1} \cdot 530^{\circ}\text{C}) = 275.66 \mu\text{m} \quad (5.14)$$

The corresponding surface area of a membrane with this radius is about  $238.72 \cdot 10^3 \mu\text{m}^2$ . Similarly the area of the four membranes (A, B, C and D) with the same doping level ( $8 \cdot 10^{21} \text{B} \cdot \text{cm}^{-3}$ ) was calculated and plotted as function of their sensitivity in figure 5.12. The sensitivity clearly increases with increasing surface area, and the effect will be explained in the next section.

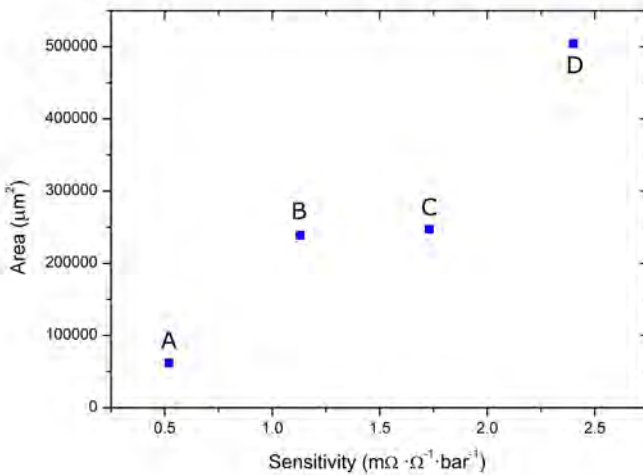


**Figure 5.12:** Relation between the calculated surface area of the B:NCD membranes and their sensitivity.

A side-effect of membrane formation related to this increase in surface area is the appearance of wrinkles, i.e. out-of-plane-deformations as the NCD membrane is confined to the (relatively smaller) rim of the glass substrate (which is described in more detail in section 5.3.2). In order to pro-

duce stress free, highly sensitive diamond layers for commercial applications an effort should be made to develop glasses that match the thermal expansion coefficient of diamond. In the development of lithium aluminosilicate glasses similar progress has been made already where glasses with tuneable viscosity and thermal expansion based on lithium oxide content were produced.<sup>[172]</sup> Nevertheless, the lowest thermal expansion coefficient reported was about  $4 \cdot 10^{-6} \text{ }^\circ\text{C}^{-1}$ . To our current knowledge, CE2000 glass is the best available borosilicate glass. Glasses with extremely low thermal expansion coefficients (e.g. ZERODUR®) exist as well, but such low coefficients would cause tensile stress that might lead to delamination. In previous experiments it was observed that the difference in thermal expansion coefficient between NCD and fused silica causes tensile stress and in turn, delamination of NCD layers thicker than 200 nm, as the thermal expansion coefficient of fused silica ( $0.5 \cdot 10^{-6} \text{ }^\circ\text{C}^{-1}$ ) is lower than that of diamond.<sup>[151]</sup> In addition, it is important to note that non-uniform stresses, e.g. uniaxial tensile stress, can also lead to wrinkling.<sup>[173]</sup>

### **Size-dependence of the sensitivity**

The dimensions of the membranes also influence their sensitivity; the thinner the membrane the higher its sensitivity.<sup>[174]</sup> Although the growth of pin-hole free diamond films of about 50 nm has been reported,<sup>[175]</sup> membranes thinner than 150 nm are too fragile for the fabrication method used in this work and possibly also for the pressure range used.<sup>[151]</sup> The relative change in resistance depends on the radius of the membranes as shown in figure 5.11. With an increase in the diameter of the membranes, there is a corresponding increase in sensitivity (see figure 5.13 and table 5.1). The larger the membrane, the bigger the relative change in resistance and the more sensitive the membrane is. This may be due to a larger amount of grain boundaries, which have been shown to be of primary importance for the piezoresistive behaviour of NCD membranes (see section 5.2.1).<sup>[168]</sup> We observed experimentally, however, that an increase

in membrane radius complicates the fabrication process, because bigger membranes tend to tear more easily. This is because the sample is mounted horizontally in the etching vessel and the etching fluid is on top of the membrane and the surrounding glass substrate, so the larger the membrane the more etching fluid it needs to carry. For comparison, commercially available piezoresistive silicon pressure sensors have reported sensitivities around  $10 \text{ m}\Omega \cdot \Omega^{-1} \cdot \text{bar}^{-1}$  for diaphragms with a size of  $2 \text{ mm} \times 2 \text{ mm} \times 15 \text{ }\mu\text{m}$ .<sup>[176]</sup> Although these commercial silicon sensors are more sensitive, diamond sensors are more suitable to withstand harsh environments.

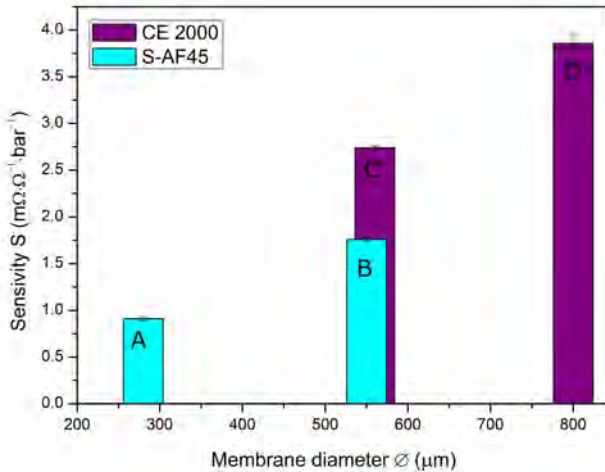


**Figure 5.13:** Pressure sensitivity ( $S$ ) in function of membrane diameter. The standard error was calculated by averaging various measurement points (120 points, i.e. 2 min and a measurement each second) at a certain inflation pressure.

In order to relate the sensitivity of the membranes with their diameter a mathematical derivation can be made starting from the gauge factor. For non-wrinkled membranes the gauge factor can be written as

$$\gamma = \frac{dR}{R} \frac{3}{2} \left( \frac{8 E \cdot t}{3 r d P} \right)^{\frac{2}{3}} \quad (5.15)$$

with  $R$ , the resistance;  $t$ , the membrane thickness;  $r$ , the membrane ra-

dus;  $E$ , the Young's modulus of the NCD:H film;  $dP$ , the differential pressure, as derived in section 5.2.1.<sup>[168]</sup> For finite changes in differential pressure and resistance, equation 5.13 can be inserted into equation 5.15,

$$\gamma \left( \frac{1}{\Delta P} \right)^{\frac{1}{3}} = S \frac{3}{2} \left( \frac{8 E \cdot t}{3 r} \right)^{\frac{2}{3}} \quad (5.16)$$

and the following is derived:

$$\frac{S_1}{S_2} = \left( \frac{r_1}{r_2} \right)^{\frac{2}{3}} \quad (5.17)$$

For wrinkled membranes, however, experimentally a power  $> 2/3$  and close to 1 is observed. With increasing membrane radius, the wrinkled area becomes relatively smaller compared to the central part of the membrane and thus a change in dependence of the sensitivity on the membrane radius would be expected. Previously, it was shown that the resistance is independent of the size of the membrane by approximating a membrane with an infinitesimal amount of rectangular prisms with length  $l(x)$  and width  $d(x)$ , with  $x$  the distance from the prism to the centre of the membrane. The change in resistance of a membrane upon inflation however does depend on the size of the membranes. For each prism the following equation holds:

$$R = \rho \cdot \frac{L}{A} = \rho \cdot \frac{L}{t \cdot x} \quad (5.18)$$

with  $R$ , the resistance;  $L$ , the length;  $A$ , the cross-sectional area;  $x$ , the width of the rectangular prism, and  $t$  and  $\rho$  the thickness and intrinsic resistivity of the diamond layer, respectively. Assuming that  $\rho$  is constant and that the change in length is a manifold of the change in cross-sectional area  $A$ , i.e.  $A$  is considered as a constant and the following can be written

$$\Delta R = \rho \cdot \frac{\Delta L}{A} = \rho \cdot \frac{\Delta L}{t \cdot x} \quad (5.19)$$



with

$$\Delta L = \frac{\sigma \cdot L_0}{E} \quad (5.20)$$

upon straining of the membrane,

$$\Delta R = \rho \cdot \frac{\Delta L}{A} = \rho \cdot \frac{\Delta L}{t \cdot x} = \rho \cdot \frac{\sigma \cdot L_0}{E} \quad (5.21)$$

follows, which explains the dependence of the change in resistivity on the diameter ( $L_0$ ) of the membranes and relates it to the tensile stress induced upon straining under the assumptions above. Nevertheless, the membrane radius is not the only determining factor, since wrinkled membranes have more degrees of freedom, their Young's modulus might be lower and Poisson ratio higher, having an impact on their internal stress and thus sensitivity.<sup>[167]</sup> To gain more insight into the influence of increasing membrane size, flat, non-wrinkled membranes should be evaluated.

### **Dopant-dependence of the sensitivity**

In order to study the influence of the dopant concentration, two additional membranes (samples E and F) were fabricated on S-AF45 glass, with diameters of 135  $\mu\text{m}$  and 400  $\mu\text{m}$  and an estimated boron concentration of  $5 \cdot 10^{21} \text{ cm}^{-3}$ , as determined from Raman spectroscopy.<sup>[123]</sup> The boron incorporation can be influenced by lowering the methane concentration, which leads to lower growth rates at the same temperature. This induces fewer structural defects within the grains and grain boundaries, which have been shown to act as sites for local enhancement of B incorporation.<sup>[42,61]</sup> Here, a decrease in boron content was induced by an increased growth speed at slightly higher temperature.<sup>[177]</sup> Demlow *et al.* showed that for boron doping of diamond single crystals the incorporation rate of boron is not as fast as the growth rate at higher temperature, which means faster growth leads to lower boron concentrations.<sup>[177]</sup> In this work a corresponding increase in the sensitivity of the membranes is observed with a decrease in boron content, as shown in figure 5.14. The sensitiv-

ities are plotted normalised to the membrane diameter to show the effect of the dopant concentration only. In previous studies, a similar effect was observed for the piezoresistivity of both boron-doped diamond films and silicon pressure sensors.<sup>[178,179]</sup> Although the absolute resistance increases, the relative change in resistance is higher for lower doped materials. The increase in absolute resistance could potentially complicate the measurement, but this effect is relatively small for the small decrease in dopant concentration and can be considered negligible for measurement purposes.<sup>[61]</sup>

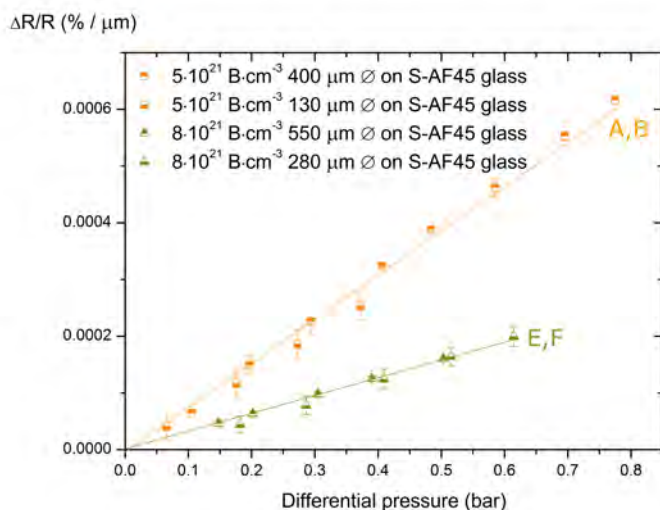


**Figure 5.14:** Relative change in resistance, normalised to the membrane diameter, as a function of applied differential pressure for four membranes with two different doping levels and different sizes. The relative change in resistance increases with decreasing doping level.

### 5.3.2 Characterisation

#### Scanning electron microscopy and Raman spectroscopy analysis

In order to analyse the fabricated membranes more thoroughly and clarify the wrinkling patterns, further characterization was conducted. To confirm the deposited layers consist of diamond and to estimate their dopant

level and quality, Raman spectroscopy was performed. The spectra show the presence of a diamond phase by the presence of the diamond optical phonon line ( $T_{2g}$  zone centre mode) at  $1332\text{ cm}^{-1}$ .<sup>[116]</sup> Moreover, the deconvoluted Lorentzian component of the broad band at  $500\text{ cm}^{-1}$  confirms the presence of boron dopant atoms above a concentration of  $10^{20}\text{ cm}^{-3}$ .<sup>[123]</sup> The diamond quality is often determined from the ratio between the diamond peak intensity and the peak intensity of the graphitic phase at  $1550\text{ cm}^{-1}$ . Using the formula proposed by Silva *et al.*<sup>[117]</sup>, the estimated graphitic phase in the diamond membranes is 2-3%. The exact location of the diamond Raman peak is known to shift to higher wavenumber under compressive stress.<sup>[116]</sup> However, in order to do a qualitative comparison, the influence of the doping level on the peak shift towards lower wavenumber has to be eliminated. To avoid distortion of the diamond lattice caused by dopant atoms which can influence the shift of the diamond Raman peak, the location of the diamond peak was measured for intrinsic NCD samples (grown under similar conditions as the B:NCD films from which the membranes were made, but in the absence of boron). (See table 5.2). For comparison, other factors that can influence the stress in the NCD film, e.g. growth conditions and grain size, are neglected as all samples were prepared and grown under identical conditions.

**Table 5.2:** Raman peak position (row 1) and shift (row 2) of the diamond peak with respect to the substrate. (The peak position for single crystal diamond is shown as a reference.) The thermal expansion coefficients of the substrates and estimated induced stresses in the diamond films based on the Raman peak shifts are given in row 3 and 4, respectively.

Substrate	S-AF45 glass	CE2000 glass	Silicon	Single crystal diamond
Diamond peak position ( $\text{cm}^{-1}$ )	$1337.0 \pm 0.5$	$1333.8 \pm 0.3$	$1333.9 \pm 0.5$	$1331.7 \pm 0.2$ <sup>[180]</sup>
Diamond peak shift wrt single crystal diamond	$5.3 \pm 0.5$	$2.1 \pm 0.4$	$2.2 \pm 0.5$	/
Thermal expansion coefficient $^{\circ}\text{C}^{-1}$	$4.5 \cdot 10^{-6}$ <sup>[181]</sup>	$3.2 \cdot 10^{-6}$ <sup>[182]</sup>	$2.6 \cdot 10^{-6}$ <sup>[183]</sup>	$1.0 \cdot 10^{-6}$ <sup>[184]</sup>
Estimated induced stress (GPa)	$3.0 \pm 0.3$	$1.2 \pm 0.2$	$1.2 \pm 0.3$	/

Based on the results, the dependence of the peak shift on the difference in thermal expansion coefficients does not seem to be linear. The small difference in peak position between NCD on CE2000 glass and NCD on silicon could be explained by the small difference in thermal expansion

coefficient, i.e.  $0.6 \cdot 10^{-6} \text{ } ^\circ\text{C}^{-1}$  (Table 5.2). For glass, however, the thermal expansion coefficient is higher than that of diamond causing compressive stress in the NCD layer. The biggest shift towards higher wavenumber is present for NCD films on S-AF45 glass confirming that these samples have the most compressive stress. For the B:NCD films used in this work, the Raman diamond peak position lies around  $1320 \text{ cm}^{-1}$  compared to the ideal value of  $1332 \text{ cm}^{-1}$ . In order to explain the low wavenumber peak position it is important to note that there are two contributions to the total stress, which are the growth-induced stress and the thermal stress.<sup>[185]</sup> The thermal stress is attributed to the difference in thermal expansion coefficient between the glass substrates and the diamond film. This effect will be discussed further on. The growth stress arises from defects and impurities, therefore the diamond peak shifts to lower wavenumber due to boron doping, as was reported by Wang *et al.*<sup>[122]</sup> Another possible explanation for peak positions at wavenumbers lower than  $1332 \text{ cm}^{-1}$  could be the grain boundary relaxation model, i.e. attractive interatomic forces across the grain boundaries induce stress in the grains due to a constrained relaxation.<sup>[186]</sup>

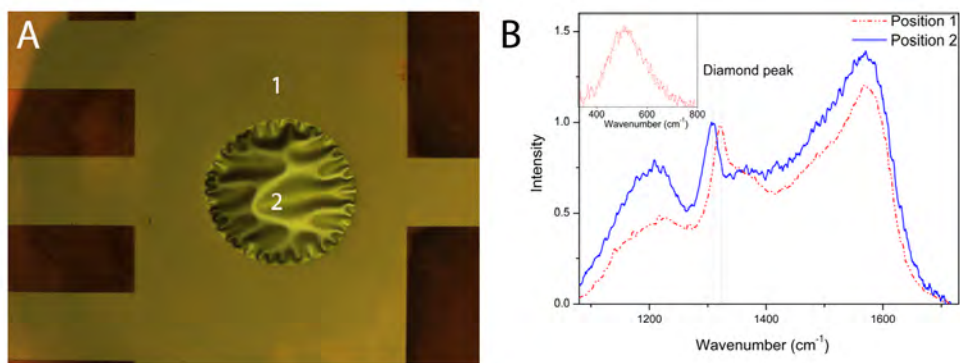


**Figure 5.15:** a) Optical image of an NCD membrane on CE glass with  $560 \mu\text{m}$  diameter. b) Raman spectrum of the NCD film attached to the CE glass substrate (Position 1) and released to form a membrane (Position 2). The spectra shown are representative spectra, for each position (1 and 2) measurements were done at least at three different spots.

In order to assess whether or not stress is released upon membrane formation because restrictions imposed by the underlying substrate are no longer present, the difference in the position of the diamond Raman peaks for B:NCD films still attached to the glass substrate (position 1) and those released as a membrane (position 2) was evaluated (figure 5.15).

The diamond Raman peak shifts to lower wavenumber ( $2.8 \pm 0.8 \text{ cm}^{-1}$ ) going from position 1 (NCD film attached to the glass substrate) to position 2 (membrane). This shift is similar to the difference in peak shift between single crystal diamond and NCD on CE2000 glass given in table 5.2 and confirms ( $1.2 \pm 0.2$ ) GPa compressive stress, within the diamond film imposed by the substrate is released upon detachment from the substrate.<sup>[187]</sup> To compare the stress of a non-inflated membrane with that

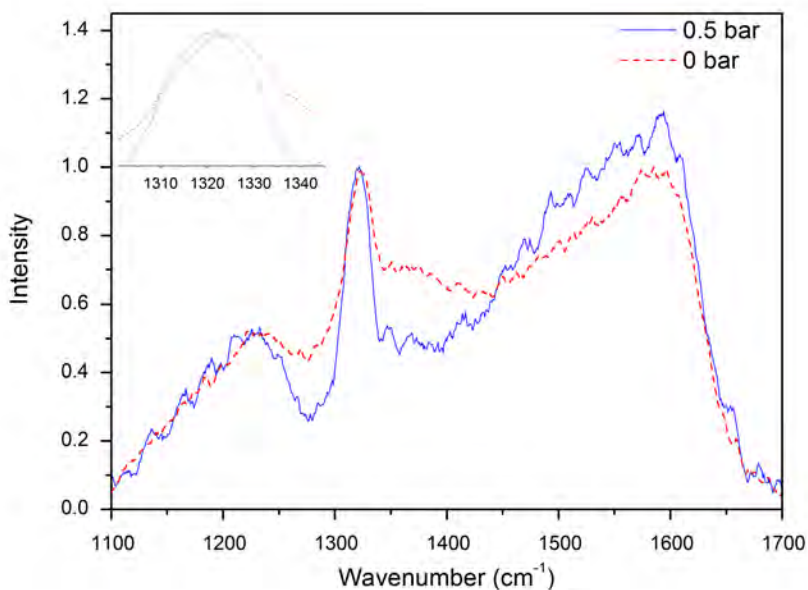


**Figure 5.16:** Raman spectra of a B:NCD membrane on CE2000 glass at 0.0 bar (red dotted) and at 0.5 bar (blue solid) differential pressure. The spectra were measured in the centre of the membranes, where the strain is the lowest and the smallest shift is expected to be measured. The inset shows the peak shift towards lower wavenumber under tensile stress caused by the inflation. The spectra shown are representative spectra, measurements both for inflated and non-inflated membranes were done at least at three different spots.

of an inflated one, their respective diamond Raman peak locations were analysed for a membrane on CE2000 glass (figure 5.16). The peak shifted from  $1322.5 \pm 0.4 \text{ cm}^{-1}$  to  $1320.9 \pm 0.6 \text{ cm}^{-1}$  when the differential pressure changed from 0 to 0.5 mbar, i.e. a shift to lower frequency of nearly  $2 \text{ cm}^{-1}$ , indicating tensile stress upon inflation. The tensile stress in the film caused by inflation is estimated to be around  $0.9 \pm 0.3 \text{ GPa}$  based on the peak shift,<sup>[188]</sup> this value has to be considered with care however, since this calculation doesn't take the presence of wrinkles into account.

### **Laser microscopy analysis**

With the aid of a laser microscope, two membranes of comparable size, i.e.  $550 \mu\text{m}$  diameter and  $560 \mu\text{m}$  diameter on S-AF45 and CE 2000 glass were used to compare the extent of wrinkling of membranes on the different types of glass, i.e. to evaluate the influence of stress on the wrinkled area (figure 5.17). Vandeparre *et al.* showed that thin sheets under boundary confinement, such as a clamped membrane, spontaneously generate a universal self-similar hierarchy of wrinkles regardless of the material of the thin sheet.<sup>[189]</sup> The authors described wrinkled patterns by the appearance of wrinklons, a localized transition zone in the merging of two wrinkles (5.17c). A wrinklone is therefore simply the transition of two wrinkles into one wrinkle at a further distance. The boundary condition in the case of our NCD membranes is the requirement that the membranes remain flat at the edges, while in the centre they are allowed to relax which causes wrinkle and thus wrinklone formation. Argon *et al.* have reported similar wrinkles and wrinklons that lead to a hierarchical pattern for the blistering of thin films adhering on a thick substrate due to compressive stress.<sup>[190]</sup> Similar patterns have also been observed for the detachment of amorphous silicon films from  $\text{SiO}_2/\text{Si}$  wafers.<sup>[191]</sup> Vella *et al.* suggested that for membranes wrinkling would occur in case of compressive stress, i.e. the membrane radius is confined to a smaller hoop.<sup>[192]</sup> The out-of-plane relaxation of NCD membranes into wrinkled patterns as observed upon

membrane formation is most likely due to the residual compressive stress in the layer.<sup>[193]</sup> In case of substantial residual compressive stress, the membranes start wrinkling. Otherwise the fabricated membrane remains flat, which would happen if there is no or a small difference in thermal expansion coefficient between a substrate and an NCD layer and no significant growth stress is induced. A higher thermal expansion coefficient for S-AF45 glass compared to CE2000 glass, explains a higher number of wrinkles for the films on S-AF45 glass. As a first comparison the number of wrinkles along the circumference of the membrane was counted. Indeed the density of the wrinkles is higher, i.e. the wavelength of the wrinkles is shorter, for the membranes on S-AF45 glass. On average the wavelength of the wrinkles is 33  $\mu\text{m}$  for membranes on S-AF45 glass and 42  $\mu\text{m}$  for membranes on CE2000 glass. Yan *et al.* predicted a similar effect, i.e. an increase in the number of wrinkles when the Young's modulus of the surrounding film becomes increasingly larger compared to that of the central membrane.<sup>[194]</sup> Moreover, laser interferometry experiments demonstrate the emergence of first generation wrinkles, which are the wrinkles appearing at the rim, by clearly showing out-of-plane deformations. The height of these deformations is indicated by the double arrow in figure 5.17a and 5.17b. Furthermore, merging of the first generation wrinkles into the second by the formation of wrinklons is indicated by the dotted lines (figure 5.17a and 5.17b).

We found that this wrinklone formation, i.e. transition of first into second generation wrinkles, takes place closer to the edge for the membranes on S-AF45 compared to those on CE2000 glass, which means that both the wrinkles and wrinklons are shorter on S-AF45 substrates. Vandeparre *et al.* derived that tensile stress along the x-direction (similar to the x-direction of figure 5.17) increases the length of the wrinklons.<sup>[189]</sup> Based on this we postulate that higher residual compressive stress in the membranes, as determined by Raman, leads to shorter wavelengths of the wrinkles and wrinklons in their respective NCD membranes.

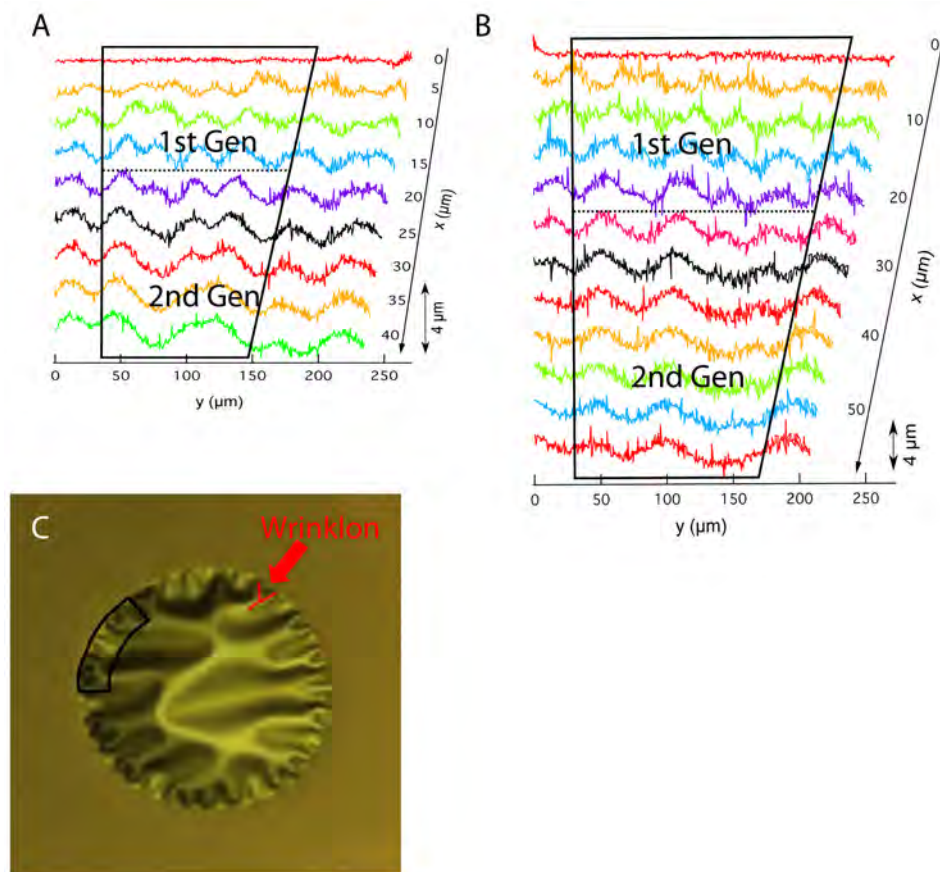


**Figure 5.17:** Topographic line profiles of the membranes a) B (550  $\mu\text{m}$  on S-AF45 glass) and b) C (560  $\mu\text{m}$  on CE2000 glass). (The x- and y- axes are at the same scale: for figure (a) a shorter length in the x-direction was sufficient to show to the the second generation wrinkles.) c) Optical image showing the transition of the first generation wrinkles into the second, i.e. the so-called wrinklon (red Y-shape), which takes place between the dotted line and the bottom black line in (a) and (b). The dotted line indicates the maximum amplitude for the maximum number of wrinkles, while at the lower black line only half of the original number of wrinkles are present.  $x = 0$  is the edge of the membrane,  $x > 0$  is in the direction of the centre of the membrane.  $y$  follows the rim of the membrane, and was converted into a straight line. The black trapezoid is the analysed area of the membrane as shown in c. The height profile, i.e. amplitude in z-direction, is shown by the double arrow indicating 4 micrometre.



### Temperature dependence of the wrinkles

As shown in figure 5.18, the wrinkles are less pronounced at 400 °C, i.e. closer to the diamond deposition temperature, and retain their original form after cooling again, which indicates that the B:NCD films are thermally stressed. To give additional proof that a major part of the residual compressive stress is due to the mismatch in thermal expansion coefficients the biaxial in-plane thermal stress  $\sigma(T)$  of the films were calculated, using the expression given in eq. 5.22,<sup>[122]</sup>

$$\sigma(T) = \frac{(\alpha_f - \alpha_s)\Delta T \cdot E}{1 - \nu} \quad (5.22)$$

where  $\alpha_f$  ( $1.0 \cdot 10^{-6} \text{ }^\circ\text{C}^{-1}$ ) and  $\alpha_s$  (given in Table 7.2) are the coefficients of linear thermal expansion of the film and the substrate, respectively,  $\Delta T$  is the temperature difference between the deposition temperature and room temperature,  $E$  and  $\nu$  are the Young's modulus (800 GPa) and Poisson ratio (0.2) of the B:NCD film respectively.<sup>[157,195]</sup>

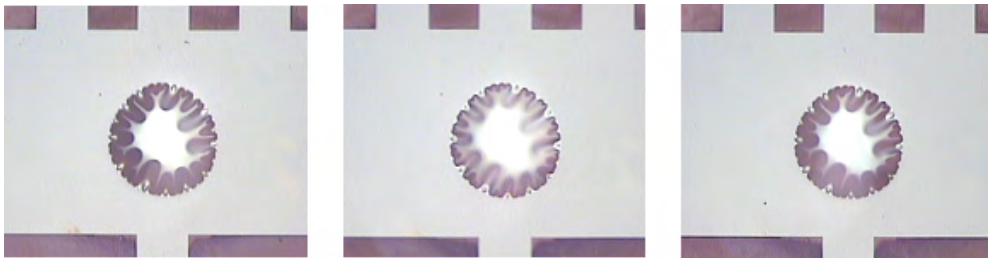


**Figure 5.18:** Optical image of the membrane of 560  $\mu\text{m}$  in diameter on CE 2000 glass at room temperature (left), at 400°C (centre) and at room temperature after cooling (right). After cooling the membrane retains its original wrinkling pattern.

The calculated thermal stress in the film is  $-(1.1 \pm 0.1)$  GPa and  $-(1.9 \pm 0.2)$  GPa for CE2000 and S-AF45, respectively, indicating that the compressive ( $\sigma(T) < 0$ ) stress in the B:NCD film on S-AF45 glass is about 60% higher than on CE2000 glass. As stated before, more wrinkles appear in more compressed membranes. In order to verify, the number of wrinkles of a membrane 560  $\mu\text{m}$  in diameter on CE2000 was compared at room temperature and at 400°C (figure 5.18). Due to our experimental set-

up, 400°C was the highest temperature within reach without graphitizing the diamond layer. There is no definite decrease in the number of wrinkles. However, as seen in the optical micrographs, the wrinkles are less individually resolved at room temperature due to the resolution of the images and light scattering of the membrane. At elevated temperature the membrane appears to be more flat, i.e. the incoming light is reflected more at the edges compared to at room temperature, which indicates less compressive stress. Lower induced compressive stress at elevated temperatures can be explained by the linear expansion of the glass substrate in every direction, leading to an increase in hole diameter of about 0.1% and thereby reducing the compressive stress by  $0.3 \pm 0.1$  GPa onto the diamond membrane as the B:NCD film does not expand to the same extent as the glass substrate.<sup>[196]</sup>

## 5.4 Conclusion

Diamond membranes on glass can be fabricated easily and show piezoresistive behaviour both for boron-doped and for hydrogen-terminated surface conductive nanocrystalline diamond films, which means they can be used as pressure sensors. For this purpose, more work on their fracture toughness needs to be performed in order to estimate how much strain they can handle. In this work, no irreversible damage to any of the diamond membranes was observed after performing multiple pressure cycles. Moreover, as differential pressure is measured, the sensor can be used in a wide pressure range with a maximum absolute pressure difference of 0.8 bar. In combination with a glass substrate, easy fabrication is possible and the resulting sensor is resistant to harsh environments.

In addition, the optimization of a robust and versatile pressure sensor, that is more resistant to a variety of media than commercially available silicon sensors, is reported. The sensitivity of the B:NCD membranes fabricated for this work is related to the residual stress in the diamond film. After

growth the B:NCD films contain both growth and thermal stress. The thermal stress of the film depends on the substrate material and more specific on its thermal expansion coefficient. For B:NCD on glass compressive stress is induced during growth leading to wrinkle formation induced by out-of-plane deformations which release stress upon removal of the substrate. The pressure sensitivity can be related to the amount of wrinkling, i.e. samples that are more wrinkled, because they were more compressed initially, need a bigger applied differential pressure for the same response as samples that are less wrinkled. Therefore the sensitivity is 55% higher for the membranes on CE2000 glass compared to membranes on S-AF45 glass. This is because the films on CE2000 glass are less compressed, due to a smaller difference in thermal expansion coefficient between this type of glass and the B:NCD film. These results show the potential of B:NCD films as pressure sensors for environments where silicon would not be suitable. The sensitivity can be enhanced easily by a decrease of the dopant concentration and clever choice of the substrate material: a substrate with a thermal expansion coefficient as close as possible to that of diamond or ideally even slightly smaller would ensure flat B:NCD layers, as long as delamination is not an issue. The sensitivity of these flat membrane devices is expected to be the highest possible, and the thermal expansion coefficient of the substrate material should be taken into account in the future design of B:NCD based pressure sensors. In hydrogen-terminated surface conductive diamond membranes a large piezoresistive effect is observed with inflation and deflation. A large instantaneous fraction is ascribed to piezoresistive hydrogenated amorphous carbon which is a major component of the grain boundaries. A time-dependent small part of the piezoresistive effect is due to charge trapping of charge carriers at grain boundaries. Piezoresistive measurements on NCD:H can reveal deeper insights in the complex electronic transport mechanism.

## **Part III**

# **Results and discussion: Diamond growth based on linear antenna technology**



## Chapter 6

# Low temperature diamond deposition

The deposition of diamond thin films at low temperatures (200 - 400 °C) would enable a wide range of novel applications such as diamond deposition on optical fibers, flat panel displays, plastics, and other temperature sensitive substrates. The crucial requirement to achieve diamond growth at low temperatures is a high plasma density at low gas pressure, leading to a low thermal load onto sensitive substrate materials and the chamber walls. Such conditions are not within reach for resonance cavity plasmas, which typically operate at pressures above 20 mbar. Recently, surface plasma wave reactors were used to deposit diamond films at pressures below 1 mbar.<sup>[98]</sup> For instance, linear antenna microwave delivery systems allow low pressure, large area growth over substrate diameters of 30 cm.<sup>[89]</sup> In addition, diamond growth at low temperatures leads to lower thermal heating of the surface and reactor walls, limiting the surface recombination of hydrogen atoms and CH<sub>3</sub> radicals, which ensures high concentrations of the species required for high quality diamond growth.<sup>[197]</sup> For commercialisation the possibility of large area deposition is of key importance. Upscaling remains an issue with common high pressure sys-

tems, since the plasma volume is rather small, i.e. limited to about 4-inch in diameter for homogeneous coverage. Since in linear antenna plasma systems the substrate area is determined by the number and length of the antennas, large area deposition is feasible. Large area deposition is also commonly performed by hot-filament CVD systems, but the filament deteriorates during deposition which leads to metal impurities. The filament can also be unstable which leads to changes in plasma chemistry. Moreover, the filament is sensitive to oxygen, so C/H/O chemistries cannot be used. And since for hot-filament CVD the reactive species are generated by thermal dissociation of the reaction gases at high temperatures, low temperature growth is difficult.<sup>[198]</sup> In addition, the current linear antenna system has the ability to be used in pulsed microwave mode, i.e. the required energy input is lower than in continuous mode, while the electron density remains very high, i.e. above  $5 \cdot 10^{11} \text{ cm}^{-3}$ , providing a high atomic hydrogen concentration allowing the deposition of high quality NCD films.<sup>[105]</sup> Nevertheless, the use of linear antenna microwave plasma enhanced chemical vapour deposition (LAMWPECVD) systems remains understudied, especially using pulsed microwaves. In order to use linear antenna technology for the deposition of diamond layers at low temperatures, the growth conditions need to be optimized first at more common temperatures. Therefore, this chapter describes the optimization of the growth parameters. For each parameter an experimental series was selected to highlight its influence. In the next sections, the results obtained in this thesis will be discussed in detail and compared to earlier findings.

## 6.1 Continuous wave mode

In the table below, a summary of all sample codes and their corresponding growth conditions is given. The parameters that are varied are pressure (samples 1a-1h), gas composition (samples 3a-3f and 5a-5b), distance be-

tween the sample and the antennas (samples 6a-6h), power (samples 8a-8f) and substrate temperature (samples 10a-10d).

**Table 6.1:** Summary of the samples with their corresponding growth conditions. [For samples deposited with the exact same conditions, multiple sample codes, such as 1f, 3c, 6f and 8d, were used to assign one and the same sample.]

Sample Code	H <sub>2</sub> (%)	CH <sub>4</sub> (%)	CO <sub>2</sub> (%)	O <sub>2</sub> (%)	Pressure (Torr)	Total flow (sccm)	Power (kW)	Temperature (°C)	Distance (cm)
1a	92	5	3	0	0.18	150	2.8	410	5
1b	92	5	3	0	0.30	300	2.8	410	5
1c	89	5	6	0	0.17	150	2.8	410	5
1d	89	5	6	0	0.20	150	2.8	410	5
1e	89	5	6	0	0.33	300	2.8	410	5
1f	91.5	2.5	6	0	0.17	150	2.8	410	5
1g	91.5	2.5	6	0	0.21	150	2.8	410	5
1h	91.5	2.5	6	0	0.30	300	2.8	410	5
3a	97.5	2.5	0	0	0.17	150	2.7	400	5
3b	94.5	2.5	3	0	0.17	150	2.8	420	5
3c	91.5	2.5	6	0	0.17	150	2.8	410	5
3d	95	5	0	0	0.17	150	2.8	420	5
3e	92	5	3	0	0.17	150	2.8	410	5
3f	89	5	6	0	0.17	150	2.8	410	5
5a	92.47	4.87	0	2.67	0.17	150	2.9	400	5
5b	94.13	2.67	3.2	0	0.17	150	2.9	405	5
6a	92	5	3	0	0.17	150	2.8	435	2.5
6b	92	5	3	0	0.17	150	2.8	410	5
6c	92	5	3	0	0.17	150	2.8	405	7
6d	92	5	3	0	0.17	150	2.8	380	9
6e	91.5	2.5	6	0	0.17	150	2.8	460	2.5
6f	91.5	2.5	6	0	0.17	150	2.8	410	5
6g	91.5	2.5	6	0	0.17	150	2.8	400	7
6h	91.5	2.5	6	0	0.17	150	2.8	380	9
8a	89	5	6	0	0.17	150	2.8	410	5
8b	89	5	6	0	0.17	150	1.9	350	5
8c	89	5	6	0	0.17	150	1.2	290	5
8d	91.5	2.5	6	0	0.17	150	2.8	410	5
8e	91.5	2.5	6	0	0.17	150	1.9	320	5
8f	91.5	2.5	6	0	0.17	150	1.2	280	5
10a	89	5	6	0	0.17	150	2.0	350	5
10b	89	5	6	0	0.17	150	2.0	400	5
10c	89	5	6	0	0.17	150	2.0	400	5
10d	89	5	6	0	0.17	150	2.0	400	5

### 6.1.1 Influence of pressure

Figure 6.1 shows SEM images of diamond films 1a-1h. It is evident that the morphology changes with decreasing pressure towards a more pronounced faceted crystalline phase, with an increase in average grain size. Above a certain pressure, enhanced renucleation is promoted, an effect that is most pronounced in sample 1e. Similar results have been reported



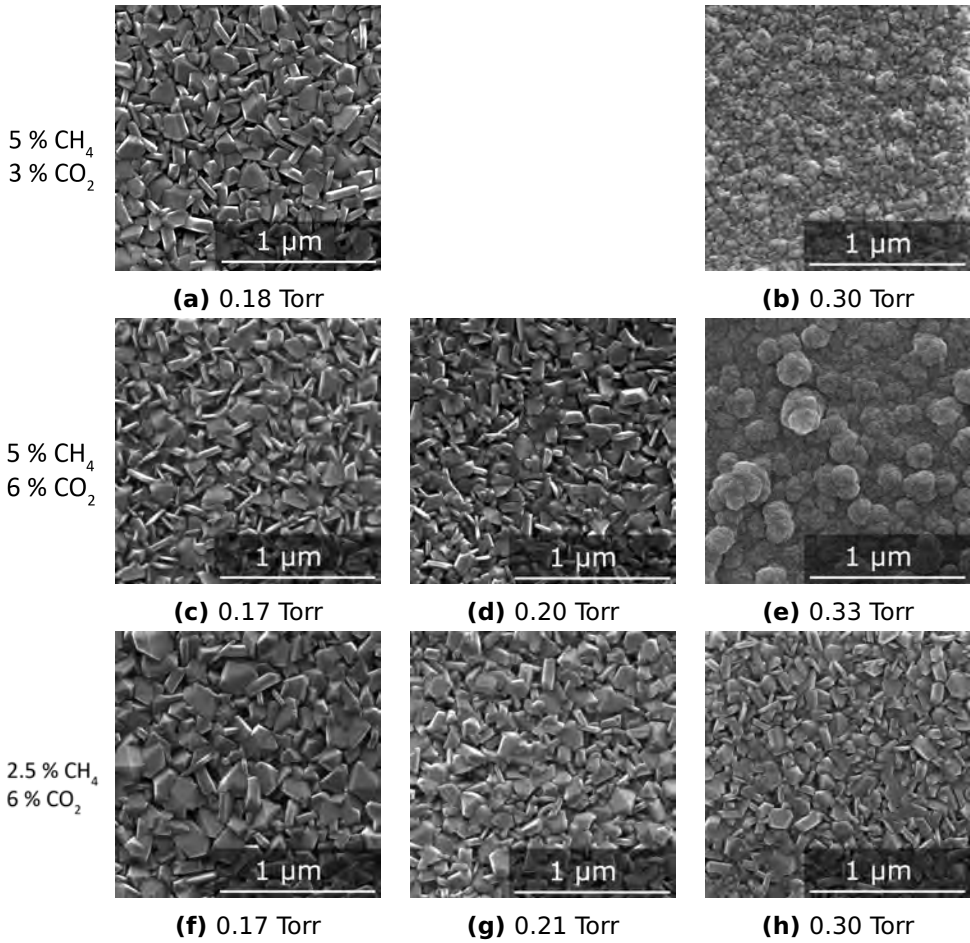


**Figure 6.1:** Series of SEM images showing the influence of pressure on the morphology of 130 nanometre thick NCD films deposited with the linear antenna system. See table 6.1 for the growth conditions.

by Kromka *et al.* and Potocký<sup>[96,98,199]</sup>: there is a transition in growth morphology from renucleated small grains to large faceted grains between 0.75 Torr and 0.075 Torr and for diamond films grown at 0.045 Torr, the facets were most pronounced.

The mean free path of the plasma species is longer at lower pressures because the plasma density decreases and the plasma expands towards the substrate surface, which enhances the reactions taking place at the substrate surface. Moreover the recombination rate of active species in-

creases with increasing pressure since the probability of collisions also increases.<sup>[200]</sup> So the pressure plays a distinctive role in the growth kinetics at the substrate surface.

In most cases Raman shows a sharp diamond peak and broad features related to  $sp^2$  phases, as shown in figure 6.2. For all gas compositions, an increase in pressure causes the bands related to  $sp^2$  phases to become more pronounced. The  $sp^3$  content (table 6.2) decreases for each gas composition, i.e. from 1a to 1b, from 1c to 1e and from 1f to 1h. The large errors are related to the fitting procedure, as described in section 3.6. For samples with a lower intensity of the diamond peak, the relative spread on single measurement points of the entire curve is larger. In addition, the more overlap there is between two bands the higher the uncertainty in the estimated surface area of these bands. This effect is most pronounced for sample 1e, in which the error is very large because of the very intense D band in the spectrum. Nevertheless, the trend for the  $sp^3$  content remains visible and lower pressures are beneficial for higher  $sp^3$  content because  $sp^2$  is suppressed. These results coincide with the re-

**Table 6.2:**  $sp^3$  fraction and growth rate of samples 1a to 1h. See table 6.1 for the growth conditions.

Sample Code	$sp^3$ fraction	Growth rate (nm/h)
1a	$0.99 \pm 0.04$	32
1b	$0.86 \pm 0.11$	43
1c	$0.96 \pm 0.36$	34
1d	$1.00 \pm 0.1$	33
1e	$0.5 \pm 1$	18
1f	$0.99 \pm 0.04$	6.5
1g	$0.99 \pm 0.4$	21
1h	$0.96 \pm 0.4$	25

sults reported by Kromka *et al.* although the overall quality obtained in this thesis is higher.<sup>[98]</sup> The Raman spectra published by Kromka *et al.* showed a characteristic diamond line only at very low pressures, i.e. 0.1 mbar (0.075 Torr), while we observed a diamond signal in the entire pressure range that was investigated. It should be noted that 0.075 Torr is the

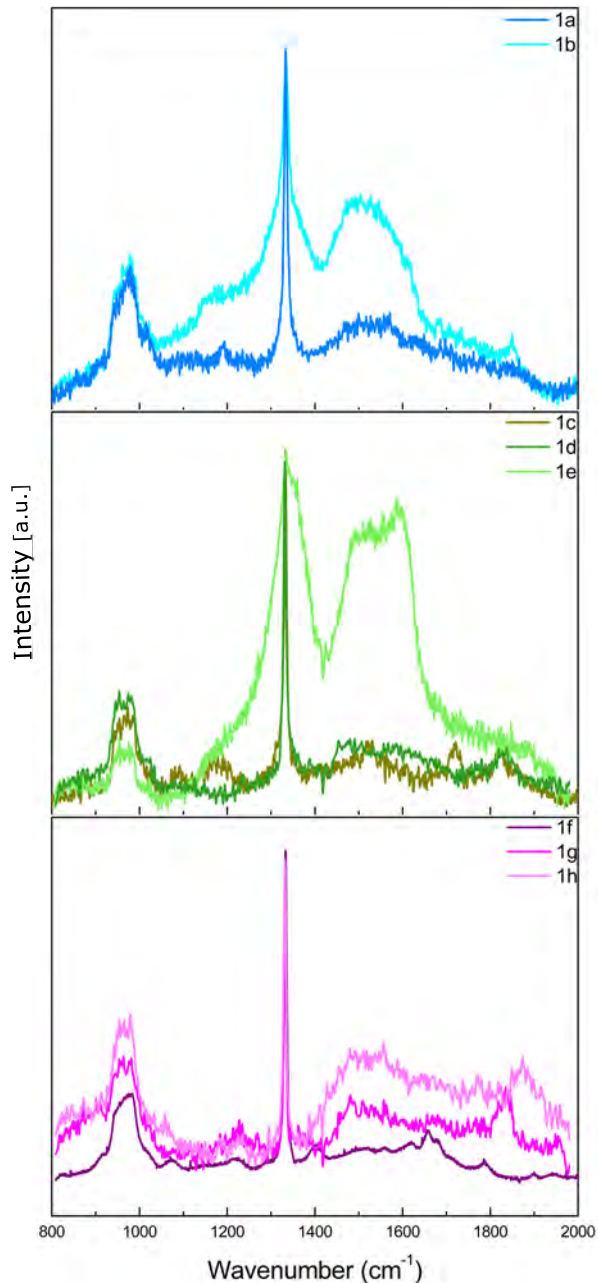


**Figure 6.2:** Raman spectra of samples 1a-1h showing the influence of pressure on the morphology of 130 nanometre thick NCD films deposited with the linear antenna system. See table 6.1 for the growth conditions.

lower limit of our current set-up due to the pump speed capacitance and the minimum flow of the flow controllers.

In case of faceted growth, the growth rate (table 6.2) is lower at lower pressures, i.e. larger crystals grow more slowly. For similar morphologies, the growth rate is more or less comparable, e.g. 20-30 nm/h. If we consider sample 1c and 1e, it is still unclear if renucleation processes enhance or limit the growth rate. The growth rates, however, could be related to the "cleanliness" of the quartz antennas, i.e. carbon material is deposited on the quartz tubes during growth. The plasma density generated at an equivalent input power is lower for quartz tubes coated with carbon material, which would also affect the growth rate (see section 2.4.1).

### **6.1.2 Influence of gas composition**

From figure 6.1, it was clear that the gas composition influences the diamond morphology. To evaluate the effect of the gas chemistry on the morphology, a matrix of samples (3a-3f) with varying methane and carbon dioxide ( $\text{CO}_2$ ) concentrations were deposited, as shown in figure 6.3. All layers show complete and homogeneous coverage without pinholes. The samples grown with lower methane concentration (upper row of figure 6.3) show larger grain sizes, an effect that has previously been reported in literature.<sup>[201]</sup> With higher methane concentrations more nucleation takes place, which leads to a larger number of smaller grains. The effect of oxygen on the morphology is evident. Without  $\text{CO}_2$  in the gas phase, there is a lot of renucleation. Increasing amounts of  $\text{CO}_2$  lead to faceting and an increase in grain size. It is widely known that oxygen plays an important role for diamond deposition processes at low temperature, because -OH groups are formed in the plasma. These -OH groups are a more efficient etchant for  $\text{sp}^2$  carbon material than atomic hydrogen. In addition, atomic oxygen abstracts surface hydrogen atoms effectively.<sup>[86]</sup> With optical emission spectroscopy it has been confirmed that the concentration of atomic hydrogen increases with  $\text{CO}_2$  addition due to the abstraction of H

atoms from molecular hydrogen by the present -OH groups.<sup>[112]</sup> Moreover, it has been shown that the nucleation density decreases with increasing CO<sub>2</sub> concentration,<sup>[90]</sup> which also leads to larger grains upon growth.

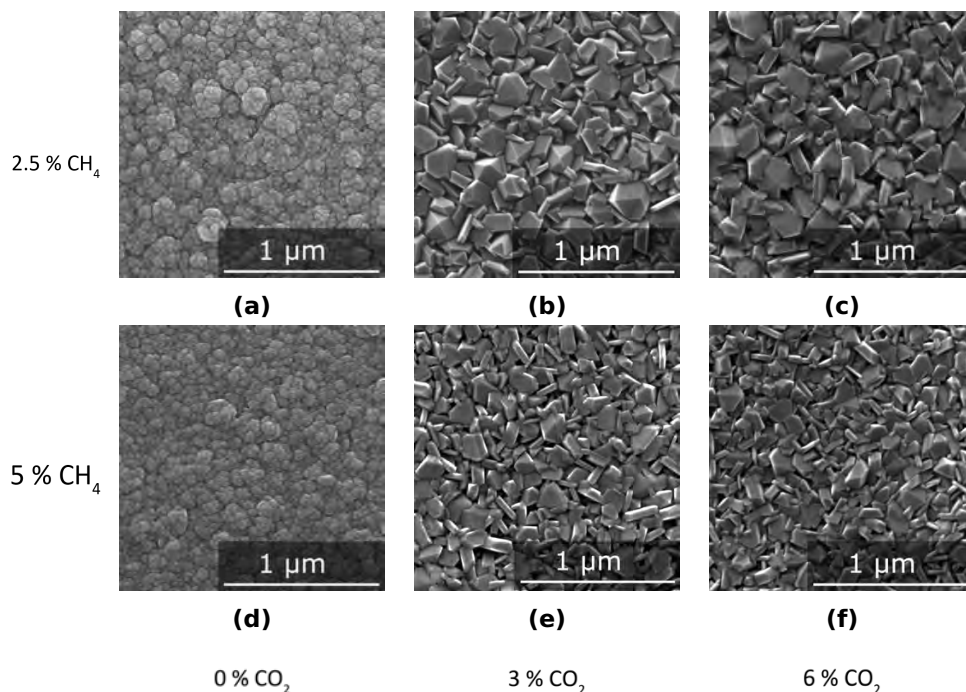


**Figure 6.3:** SEM images of samples 3a to 3f showing the influence of the gas composition on the morphology of 130 nanometre thick NCD layers. See table 6.1 for the growth conditions.

Raman spectroscopy (shown in figure 6.4) was used to evaluate the diamond quality. The addition of CO<sub>2</sub> to the gas phase leads to a significant improvement in the intensity of the diamond peak. The sp<sup>3</sup> content increases, as shown in table 6.3, and the diamond peak width decreases. The errors (see section 3.6) get increasingly bigger for samples with lower sp<sup>3</sup> content since the relative spread on the single measurement points of the entire curve is bigger, since the absolute intensity (of the diamond peak) is lower. Therefore the errors here are more an indication of the spread of the points than of the accordance between the fit and the actual curve. The improvement of the deposited layers at higher CO<sub>2</sub> concentra-

tions is related to the amount of -OH groups. As stated before, oxygen (together with hydrogen) acts as an etchant for  $sp^2$  phases and is responsible for the activation of the surface and for the creation of atomic hydrogen by the abstraction of hydrogen atoms. These findings are in agreement with results reported previously.<sup>[105,112]</sup> In addition, these reports showed that at even higher  $CO_2$  concentrations the  $sp^3$  content is found to decrease, presumably due to the drifting out of the diamond growth zone in the Bachmann triangle. Therefore we assume that we are close to the optimum for  $CO_2$  around 6 %.

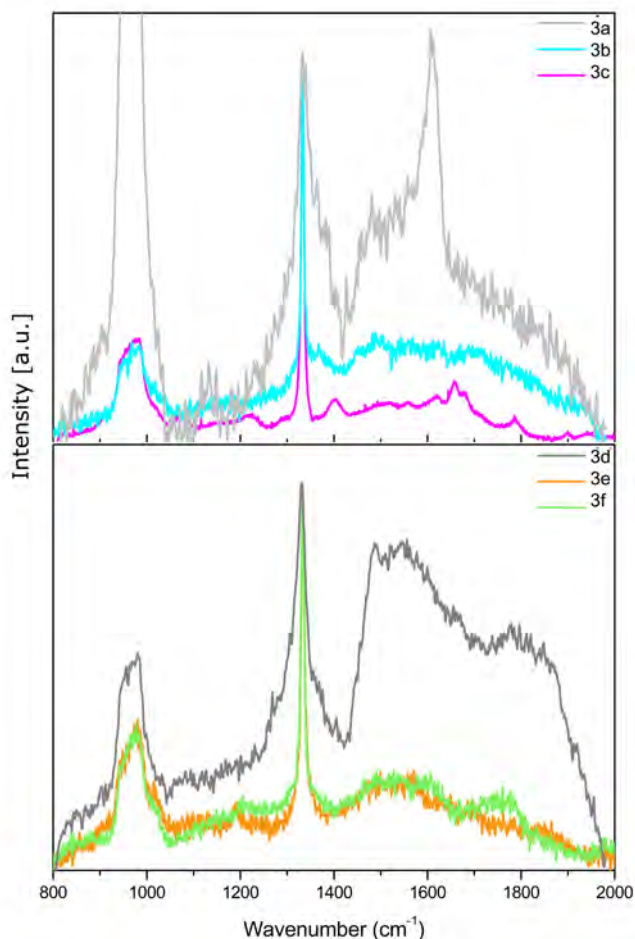


**Figure 6.4:** Raman spectra showing the influence of the gas composition on the morphology of samples 3a to 3f. See table 6.1 for the growth conditions.

As shown in table 6.3, there is no obvious trend to the growth rate. For low methane concentrations (2.5 % CH<sub>4</sub>) the growth rate remains more or less constant with CO<sub>2</sub> content; while for higher methane concentrations (5 % CH<sub>4</sub>) the growth rate increases with CO<sub>2</sub> concentration. In general the growth rates are higher at higher methane concentrations which is to be expected with higher carbon content. A possible explanation could follow from considering both the carbon and oxygen content. At lower methane concentrations, the influence of the addition of CO<sub>2</sub> on oxygen etching is bigger, which means the growth is dominated by etching, which causes the growth rate to decrease or remain constant. At higher methane concentrations, the influence of oxygen etching upon addition of CO<sub>2</sub> is still present but the total carbon content has a bigger impact on the growth rate and thus causes an increase with CO<sub>2</sub> addition.

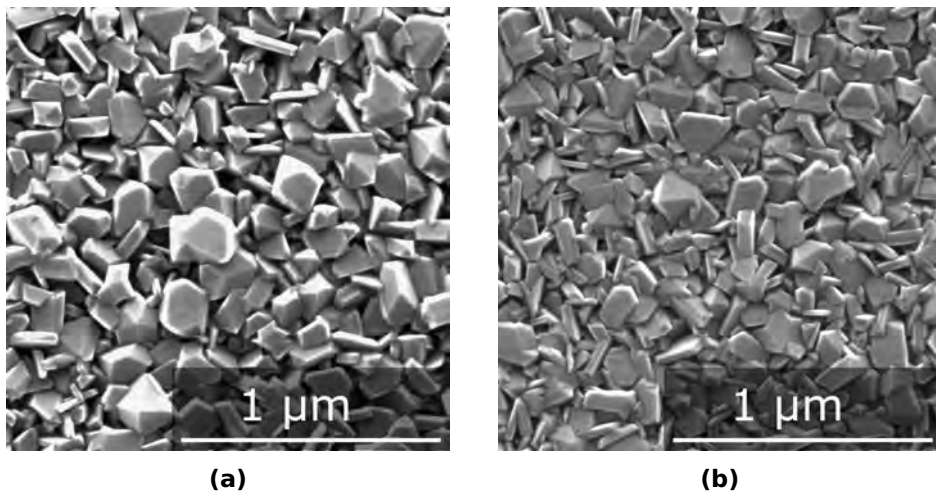
**Table 6.3:** sp<sup>3</sup> fraction and growth rate of samples 3a to 3f. See table 6.1 for the growth conditions.

Sample Code	sp <sup>3</sup> fraction	Growth rate (nm/h)
3a	0.82 ± 2.6	15
3b	0.98 ± 0.06	14
3c	0.99 ± 0.05	6.5
3d	0.95 ± 0.1	24
3e	0.99 ± 0.04	32
3f	0.99 ± 0.03	35

In order to verify the validity of the Bachmann triangle for this particular system, two samples grown with the same carbon-to-oxygen ratio, but with different gas compositions were compared. Only the carbon-to-oxygen ratio ( $\chi_C = 0.478$ ) was kept constant because of safety reasons. For safe laboratory practise, it is recommended to use a maximum of 4 % oxygen in hydrogen. From the SEM pictures (figure 6.5) it is evident that, independent of the source gas, a particular carbon-to-oxygen ratio leads to a certain morphology. Differences in grain size are explained by a difference in total carbon-flux. As stated above, a lower carbon content (sample 5a) leads to larger grains.

**Table 6.4:** Gas composition for sample 5a and 5b in figure 6.5.

	H <sub>2</sub> -flow sccm	CH <sub>2</sub> -flow sccm	CO <sub>2</sub> -flow sccm	O <sub>2</sub> -flow sccm
Sample 5a	138.7	7.3	/	4
Sample 5b	141.2	4	4.8	/

**Figure 6.5:** SEM images of a) sample 5a and b) sample 5b from table 6.1.

### 6.1.3 Influence of the distance to the antennas

The 'large' distance between the sample and the antennas is the key feature of the linear antenna growth system, which allows for low thermal load onto the substrate. It is however necessary to stay in the NCD or MCD growth regime, and not to lower the substrate table too much for renucleation to take place, as discussed in section 1.3.2, since for higher distances between the substrate and the antennas, the effective electron temperature decreases.<sup>[96]</sup> As mentioned in section 2.4.2, the electron temperature is highest close to the vacuum-to-atmosphere interface and decreases with distance.<sup>[93]</sup> This leads to crystalline, well-faceted layers at higher pressures close to the antennas than at further distances.<sup>[97]</sup> Since the effect of pressure has been discussed in section 6.1.1 we can conclude that closer distances are beneficial for nanocrystalline diamond



growth. On the other hand at our working pressures of 0.2 Torr, the mean free path between two interactions is about 5 cm (for air). These scattering events are important to even out the alternating cold and hot regions due to the standing waves, since the original velocity and momentum of the particles are averaged out by collisions. The uniformity can be improved by an increase in pressure, since the mean free path decreases. But it was shown in section 6.1.1 that this leads to a decrease in diamond quality. The mean free path is an important parameter to consider, but one has to keep in mind that the gas enters the plasma system with a certain velocity and in a certain direction. So it is important to consider all factors, and not only the mean free path. An equilibrium between the generation of active species (at close distance) and the evening out of the hot and cold regions of the plasma (at further distances) is important for high quality diamond growth.

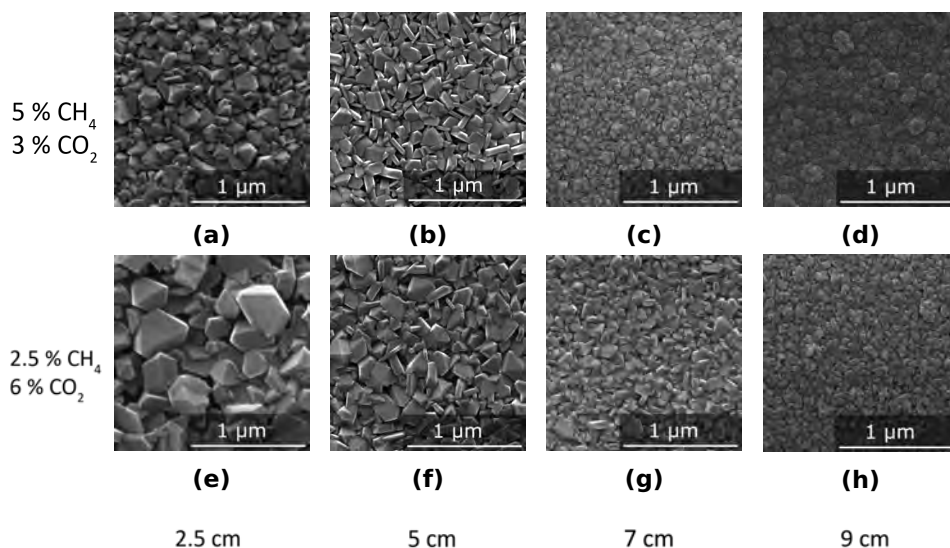


**Figure 6.6:** SEM images of samples 6a to 6h showing the influence of the sample-to-antenna-distance on the morphology of samples grown at varying distances of 2.5, 5, 7 and 9 cm from left to right respectively with temperatures dependent on the distance. See table 6.1 for the growth conditions.

In figure 6.6, the distance between the substrate and the antennas was varied (2.5 cm - 5 cm - 7 cm - 9 cm) for two gas compositions. For more

ideal gas composition (6 % CO<sub>2</sub> and 2.5 % CH<sub>4</sub> - samples 6e - 6h), the effect of the distance on the morphology is less distinct. At 7 cm the grain size has decreased but the faceted character remains. At 9 cm the electron temperature is too low for high quality diamond growth, which means the number of excited species, and in particular atomic hydrogen, will be lower, which leads to renucleation. For samples grown with 3 % CO<sub>2</sub> and 5 % CH<sub>4</sub> (top row of figure 6.6) renucleation starts to take place at 7 cm from the antennas, due to a lower oxygen content (cf. section 6.1.2) In addition, after close inspection of sample 6e, pinholes are observed, which means the diamond layer is not fully closed. A possible reason to explain this effect is that at such close distances the plasma temperature is higher and there is an increased etch rate caused by the presence of oxygen.<sup>[97]</sup> For sample 6a, it is still unclear why the morphology is different from that grown at further distances with the same gas composition or with lower CH<sub>4</sub> and higher CO<sub>2</sub> content at similar distances. Its corresponding Raman spectrum (figure 6.7) shows a higher contribution of sp<sup>2</sup> related peaks. Furthermore, Raman confirms the conclusions drawn from the SEM images. At higher distances from the antenna, the intensity of the diamond Raman signal decreases and the peak broadens. Higher concentrations of CO<sub>2</sub> and lower concentrations of CH<sub>4</sub> enhance the diamond character, as stated above. Nevertheless, very high sp<sup>3</sup> contents are obtained in particular for samples grown with 2.5 % CH<sub>4</sub> and 6 % CO<sub>2</sub> (6e - 6h), as shown in table 6.5. The growth rate distribution seems to be random for samples 6a - 6d (5 % CH<sub>4</sub> and 3 % CO<sub>2</sub>), possibly because of the efficiency of microwave penetration and excitation due to coverage of the quartz tubes (see section 2.4.1).

For samples 6e - 6h, the growth rate increases with increasing distance between the sample and the antennas, i.e. the growth rate decreases with the grain size. Oxygen etching is enhanced closer to the substrate table, which causes less renucleation to take place and allows the grains to develop but at a lower rate.

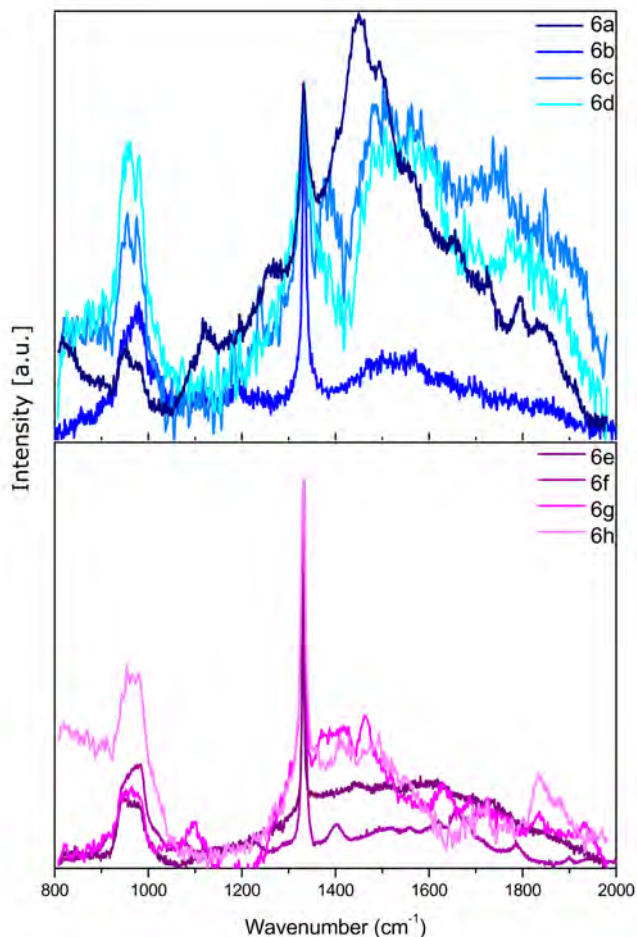


**Figure 6.7:** Raman spectra of samples grown at varying sample-to-antenna-distances of 2.5, 5, 7 and 9 cm from 6a to 6d and 6e to 6h with temperatures dependent on the distance. See table 6.1 for the growth conditions.

**Table 6.5:**  $sp^3$  fraction and growth rate of samples 6a to 6h with varying sample-to-antenna distance. See table 6.1 for the growth conditions.

Sample Code	$sp^3$ fraction	Growth rate (nm/h)
6a	$0.72 \pm 0.3$	27
6b	$0.99 \pm 0.04$	32
6c	$0.71 \pm 1.9$	23
6d	$0.97 \pm 0.3$	22
6e	$0.99 \pm 0.01$	7
6f	$0.99 \pm 0.05$	6.5
6g	$1.00 \pm 0.3$	21
6h	$0.99 \pm 0.3$	28

### 6.1.4 Influence of power

The influence of the applied power was probed with two series of samples grown with different gas compositions. Three power settings were probed: 2.8 kW, 1.9 kW and 1.0 kW. The supplied power is needed to ensure a high gas temperature, which means a high amount of activated species. At higher powers, more gas species are activated and in particular the atomic hydrogen concentration is higher. This is because atomic hydrogen is mainly created via plasma activated processes, e.g. electron impact, which occurs more frequently at higher powers. Since surface wave plasmas are characterised by a low gas temperature, thermal dissociation of active species is negligible.<sup>[93]</sup> This increased amount of atomic hydrogen at higher powers, created by electron impact, etches away  $sp^2$  more readily, which leads to an increase in grain size and diamond quality.

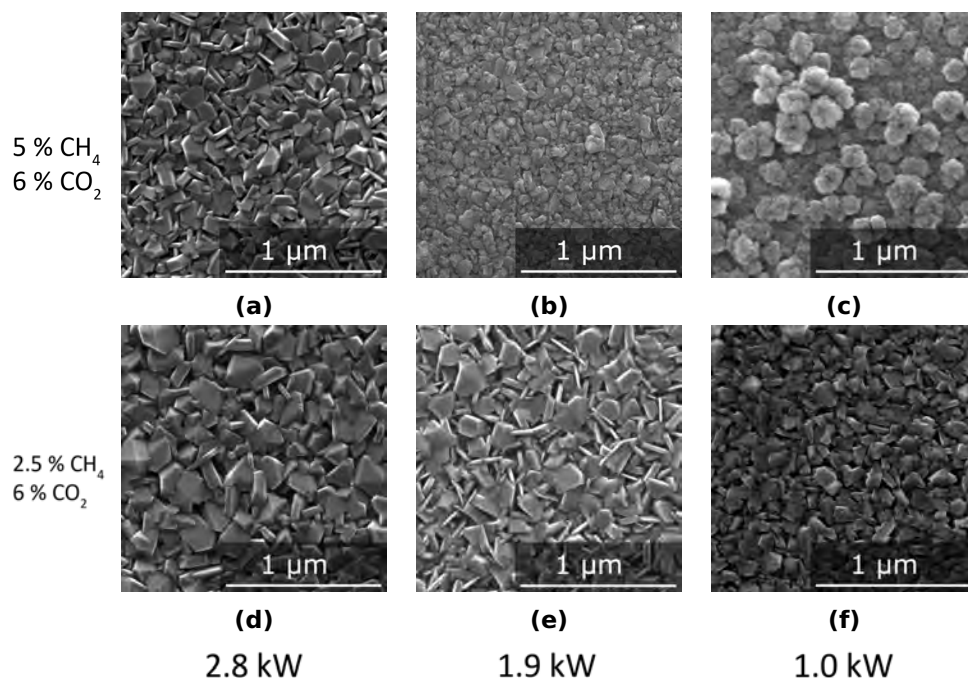


**Figure 6.8:** SEM images of samples 8a to 8f showing the influence of the power on the morphology of diamond films. See table 6.1 for the growth conditions.

The morphologies are shown in figure 6.8 and it is clear that higher powers are beneficial for the diamond grain size and the level of faceting. At 1.0 kW the amount of active species is not high enough for high quality NCD growth. Of course, an increase in power leads to an increase in temperature too, because more energy is supplied. The effect of externally applied heat by means of the substrate heater will be explained in more detail in the next section.

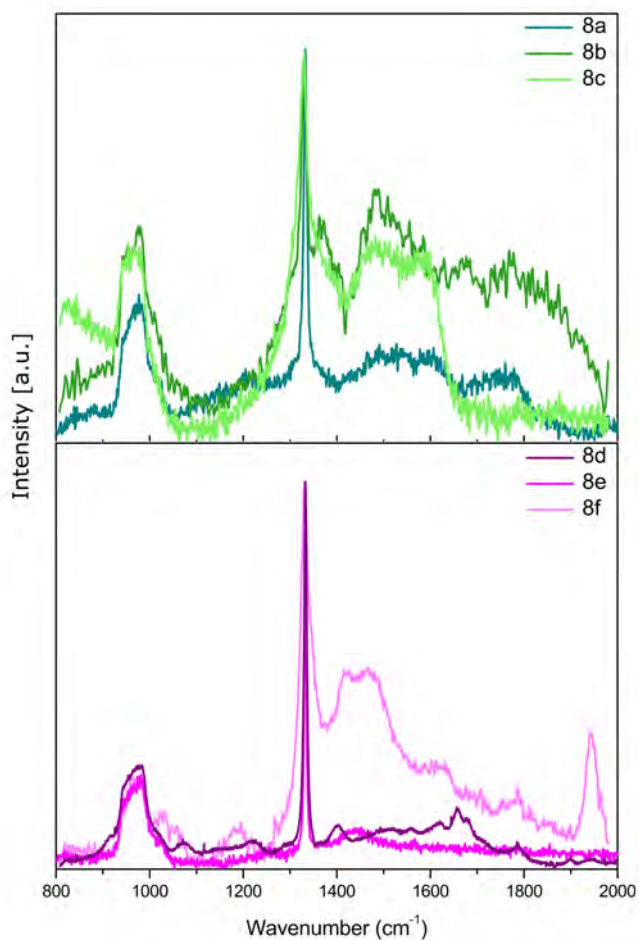


**Figure 6.9:** Raman spectra of samples 8a to 8f grown with the power varying from 2.8, 1.9 to 1.0 kW. See table 6.1 for the growth conditions.

The obtained Raman spectra are shown in figure 6.9 and confirm the trends observed with SEM. Table 6.6 shows that, for samples 8d - 8f, the

**Table 6.6:**  $sp^3$  fraction and growth rate of samples 8a to 8f with varying sample-to-antenna distance. See table 6.1 for the growth conditions.

Sample Code	$sp^3$ fraction	Growth rate (nm/h)
8a	$0.99 \pm 0.03$	35
8b	$0.96 \pm 6.6$	47
8c	$0.99 \pm 0.4$	37
8d	$0.99 \pm 0.05$	6.5
8e	$0.99 \pm 0.02$	15
8f	$0.97 \pm 1.2$	13

$sp^3$  content decreases with decreasing power because of a corresponding decrease in active species and more in particular atomic hydrogen. In addition, the growth rate increases first upon lowering the power and then decreases again. A possible explanation is the decrease in etching rate with lowering power which is at even lower power compensated by the slow renucleated growth mechanism.

### 6.1.5 Influence of substrate temperature

The substrate temperature is closely related to the applied power and the distance between the sample and the antennas. At 5 cm distance, the maximum safe power (2.8 - 2.9 kW) leads to temperatures around  $410 \pm 20$  °C. When the power is lowered to 1.8 - 1.9 kW, the temperature drops to about  $330 \pm 20$  °C, and at 1.1 - 1.2 kW the temperature is about  $280 \pm 20$  °C. These growth conditions and the respective morphology and characteristics have been discussed in the previous section. In addition, the linear antenna system is equipped with a heater inside the substrate table, as shown in figure 2.4. To investigate the influence of the temperature of the heater, four samples were grown at the same conditions (5 %  $CH_4$ , 6 %  $CO_2$ , 2.0 kW,  $T_{max} = 350 \pm 10$  °C), one without heating (sample 10a) and three with heating. However, the samples were heated in different ways. For sample 10b the temperature was set to 400 °C in steps of 20 °C after the growth had started and the substrate was already at 320 °C by microwave heating. Sample 10c was heated gradually in steps of 20

°C from the start, so simultaneously with microwave heating. And sample 10d was first heated to 250 °C, then the microwaves were switched on and within a couple of minutes 400 °C was reached. To explain the obtained morphology, shown in figure 6.10, a closer look at the gas chemistry is needed. The gas species can be activated electronically (through electromagnetic radiation; in this case microwave excitation- related to the input power - as discussed in the previous section) and thermally (by conduction from the heater and/or convection in the gas flow). If the heater (substrate table) is set to 400 °C, reactive species gain extra thermal energy which allows adsorbed species to migrate around on the diamond surface and find a stable position to complete the lattice and an improvement in the NCD layer quality is expected. Without externally supplied heat this migration is limited and the species bond to the surface wherever they reach it, which might not be the correct position/orientation to propagate the diamond lattice, i.e. renucleation occurs. Thermal dissociation of hydrogen becomes important only at high gas temperatures (around 3000 K) and is not considered here.<sup>[202]</sup>

The difference in morphology between sample 10a and 10b can be explained as follows. For sample 10b, without initial heating, the first stages of growth led to a similar layer as sample 10a. So if the heat is only supplied after the start of the growth, there will be a conversion towards more faceted growth, i.e. certain crystals will become larger and dominate the appearance. This conversion is still ongoing in sample 10b. During gradual heating, there is a continuous supply of heat, so electronically activated species become more mobile and surface and plasma chemistry leads to a faceted morphology. Sample 10c (figure 6.10c) shows a larger average grain size than samples 10a and 10b. Similar results were expected for sample 10d, and although the layer is less faceted than 10c, it has a more crystalline appearance than 10a and 10b. The very subtle improvement in layer quality can be explained by two possible reasons. The first option is the stability of the plasma, the same settings can show a slight variation in supplied microwaves, i.e. maybe the power was slightly lower for

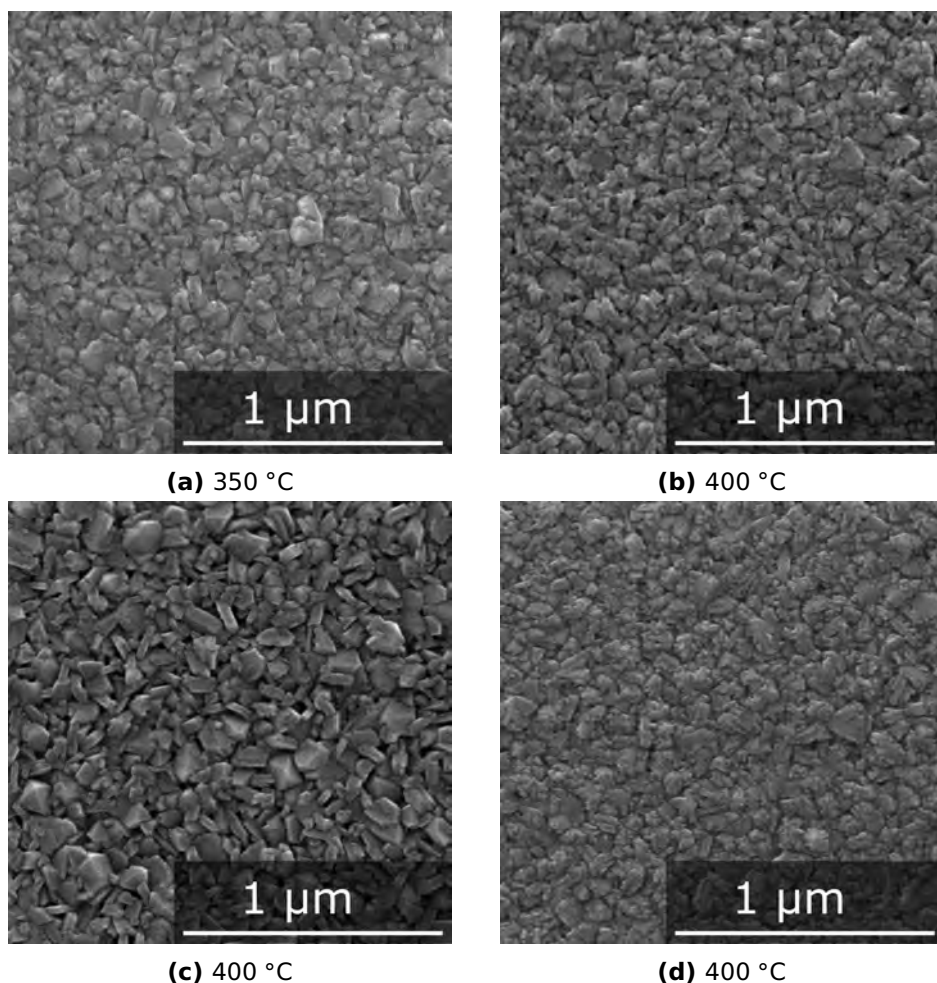


**Figure 6.10:** SEM images showing the influence of external heating on the morphology of samples 10a, 10b, 10c and 10d. Sample 10a was not heated externally and samples 10b, 10c, and 10d were heated in three different ways. For sample 10b the temperature was set to 400 °C in steps after the growth had started and the substrate was already at 320 °C by microwave heating. Sample 10c was heated gradually in steps of 20 °C from the start, so simultaneously with microwave heating. And sample 10d was first heated to 250 °C, then the microwaves were switched on and within a couple of minutes 400 °C was reached.

sample 10d. The second option is that the quartz tubes were slightly more covered and there was less microwave penetration and excitation of the plasma, this is the memory effect, as explained in section 2.4.1. Because we are working in such a small temperature window, i.e. only 50 degrees difference, it is difficult to make any real conclusions concerning sample



10d.

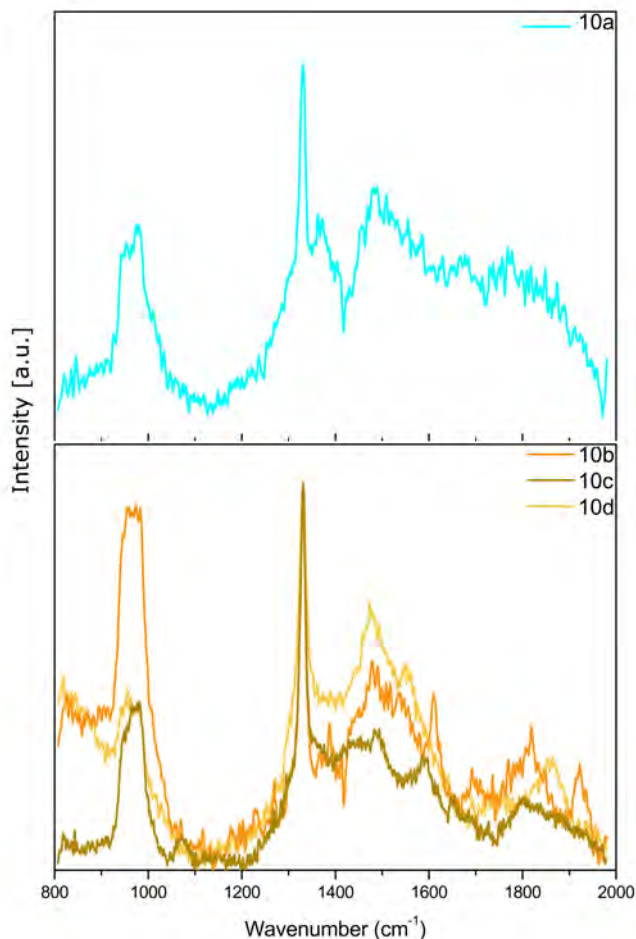


**Figure 6.11:** Raman spectra of samples 10a, 10b, 10c and 10d. Sample 10a was not heated externally and samples 10b, 10c, and 10d were heated in three different ways. For sample 10b the temperature was set to 400 °C in steps after the growth had started and the substrate was already at 320 °C by microwave heating. Sample 10c was heated gradually in steps of 20 °C from the start, so simultaneously with microwave heating. And sample 10d was first heated to 250 °C, then the microwaves were switched on and within a couple of minutes 400 °C was reached.

The Raman spectra in figure 6.11 confirm the results of the SEM analysis. Sample 10c, clearly has the most pronounced diamond peak (highest intensity and smallest width), and the other three spectra look very similar. The  $sp^3$  content (table 6.7) doesn't show a trend; this is probably

**Table 6.7:**  $sp^3$  fraction and growth rate of samples 10a, 10b, 10c and 10d. Sample 10a was not heated externally and samples 10b, 10c, and 10d were heated in three different ways. For sample 10b the temperature was set to 400 °C in steps after the growth had started and the substrate was already at 320 °C by microwave heating. Sample 10c was heated gradually in steps of 20 °C from the start, so simultaneously with microwave heating. And sample 10d was first heated to 250 °C, then the microwaves were switched on and within a couple of minutes 400 °C was reached.

Sample Code	$sp^3$ fraction	Growth rate (nm/h)
10a	$0.96 \pm 6.6$	47
10b	$0.93 \pm 0.4$	39
10c	$0.99 \pm 0.3$	46
10d	$1.00 \pm 0.3$	36

due to large errors on the calculated values. The main conclusion from this section, if we compare sample 10c to sample 11a (from the previous section), is that heat supplied from an external heat source and not by the microwave power is not able to excite molecules to the same energy levels and thus leads to less faceted, renucleated type of morphologies.

## 6.2 Pulsed wave mode

As explained in detail in section 2.4.3, diamond growth can also be performed using pulsed microwaves, which should lead to a very high diamond quality. Based on the findings that the frequency influences the diamond quality and the optimal growth conditions obtained in continuous mode, two series of samples were grown, one series without the use of the substrate heater and one series with external heating. The growth conditions of all the samples grown for this section are summarised in table 6.8. We used the substrate heater to ensure a similar substrate temperature for all the samples in the second series in order to eliminate the temperature as a varying parameter even though it was stated in section 6.1.5 that external heat is not able to excite reactive species. Each series represents a matrix of parameters: for different peak powers, the pulse off-time is varied with a constant on-time of 10  $\mu$ s, which leads to three

different frequencies: i.e. 20, 30 and 40 kHz. Although a lower methane concentration, i.e. 2.5 % CH<sub>4</sub>, leads to a better diamond quality, the samples were grown with 5 % CH<sub>4</sub> and 6 % CO<sub>2</sub> at 0.17 Torr because of the corresponding increase in growth rate (see section 6.1.2). Table 6.8 summarizes the conditions of the varied parameters. The outliers in terms of conditions were not grown: 5 kW peak power at 25 kHz leads to a very low average power, at which no high quality diamond growth is expected based on the results obtained in section 6.1.4. 10 kW at 40 % duty cycle is impossible with the current set-up (the maximum allowed average power is 3.5 kW and 10 kW peak power with a duty cycle of 40 % leads to an average power of 4.0 kW).

**Table 6.8:** Summary of the samples grown in pulsed mode with their corresponding growth conditions. For the second series (samples 14a-14f), the temperature was kept constant. The samples that were heated externally to reach this temperature are indicated with an asterisk. The samples of series 14 that were not heated are identical to sample series 12, e.g. samples 12b and 14b are identical.

Sample Code	On-time ( $\mu$ s)	Off-time ( $\mu$ s)	Frequency (kHz)	Duty cycle (%)	Peak Power (kW)	Average Power (kW)	Temperature °C
12a	10	20	32	32	5	1.6	240
12b	10	15	40	40	5	2.5	380
12c	10	30	25	25	7	1.8	270
12d	10	20	32	32	7	2.2	325
12e	10	15	40	40	7	2.9	380
12f	10	30	25	25	10	2.6	325
12g	10	20	32	32	10	3.0	360
14a	10	20	32	32	5	1.6	380*
14b	10	15	40	40	5	2.5	380
14c	10	30	25	25	7	1.8	380*
14d	10	20	32	32	7	2.2	380*
14e	10	15	40	40	7	2.9	380
14f	10	30	25	25	10	2.6	380*
14g	10	20	32	32	10	3.0	360

These samples were grown with 5% CH<sub>4</sub>, 6 % CO<sub>2</sub> at 0.17 Torr and 5 cm sample-to-antenna distance.

Unfortunately, for our experiments no improvement of the diamond quality was obtained compared to continuous mode. Similar results were obtained by Monéger *et al.* in 2007 using a bell jar reactor.<sup>[203]</sup> In their experiments the renucleation rate was always higher for pulsed mode and the resulting grain size smaller than for continuous wave mode. Nevertheless, we can draw some conclusions from the obtained results.

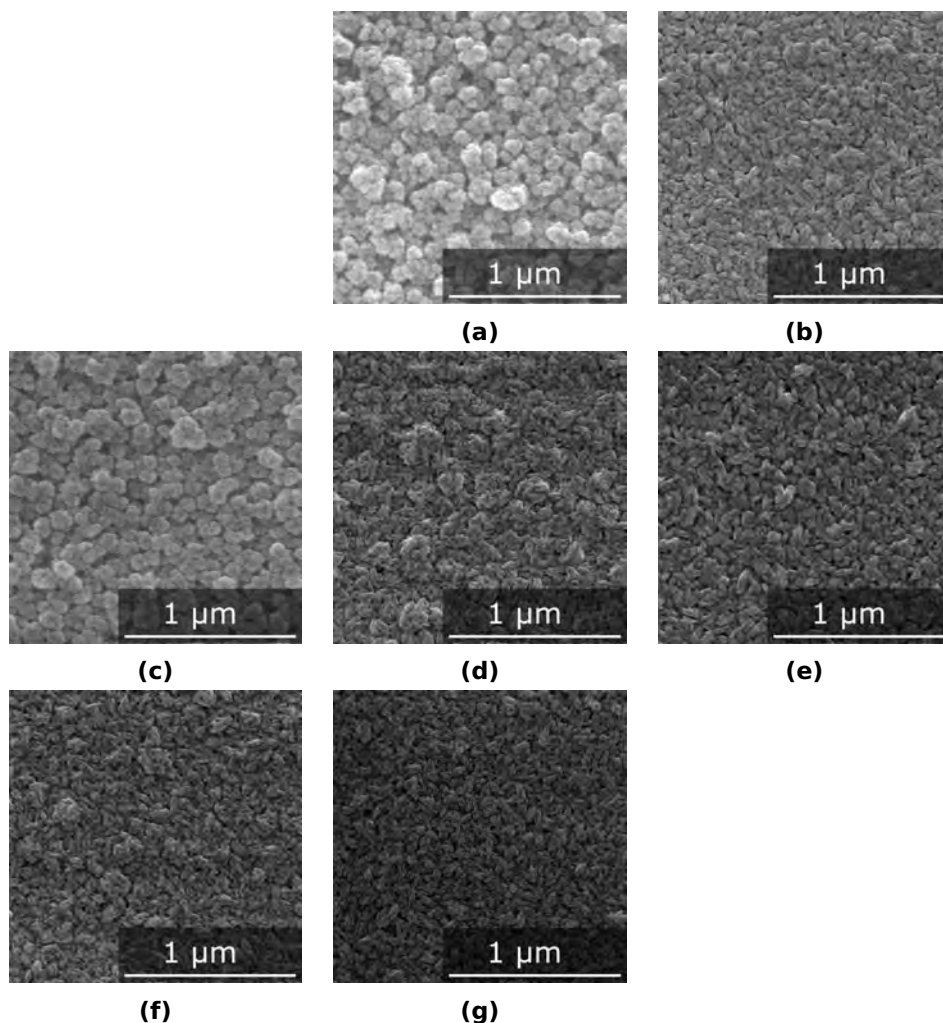


**Figure 6.12:** SEM images of samples 12a to 12g showing the influence of the pulse settings on the morphology. The growth conditions are summarised in table 6.8.

First of all, the morphological difference between the samples grown without (see figure 6.12) and with substrate heater (see figure 6.13), is most evident if sample 12d is compared to 14d, and 12f to 14f. The increase in temperature shifts the obtained morphology from renucleated to more cauliflower-like, i.e. there is an increase in surface roughness. This means that active species are activated or excited by means of the applied power and not because of the supplied heat from the substrate stage, as con-

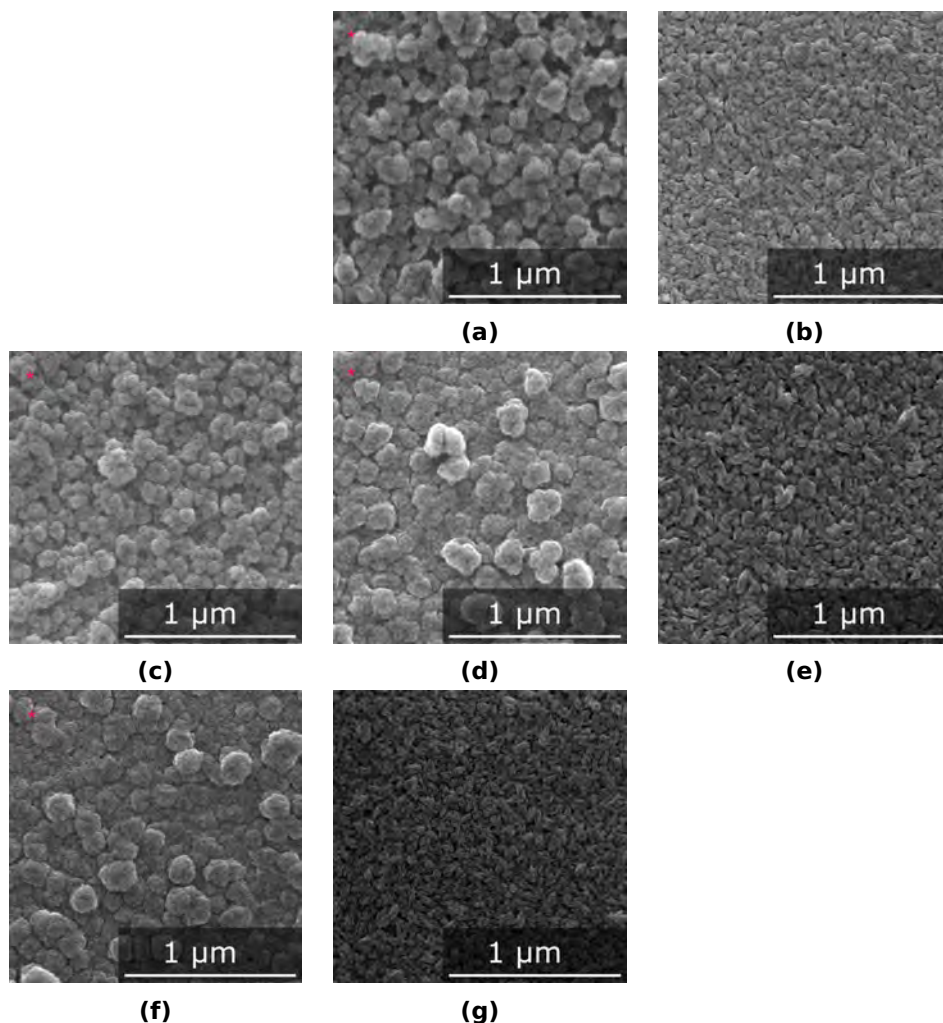


**Figure 6.13:** SEM images of samples 14a to 14g grown with constant temperature showing the influence of the pulse settings on the morphology. The growth conditions are summarised in table 6.8. The samples that were heated externally to obtain this temperature are indicated with a pink asterisk.

cluded in section 6.1.5. Moreover, the increase in substrate temperature causes a decrease in growth speed. A second trend that we can see is that the morphology is similar for samples grown with similar average powers, i.e. 12a and 12c; 12b, 12d and 12f; and 12e and 12g. This trend is unexpected since the average power is reported to be responsible for substrate and chamber wall heating only, while the amount of active

species depends on the maximum peak power.<sup>[203]</sup> Thirdly, the morphology goes from cauliflower type to flat more crystalline layers with a small level of faceting (in sample 12c, 12d and 12e) upon increase of the duty cycle (with a corresponding increase in average power) for the same peak power.

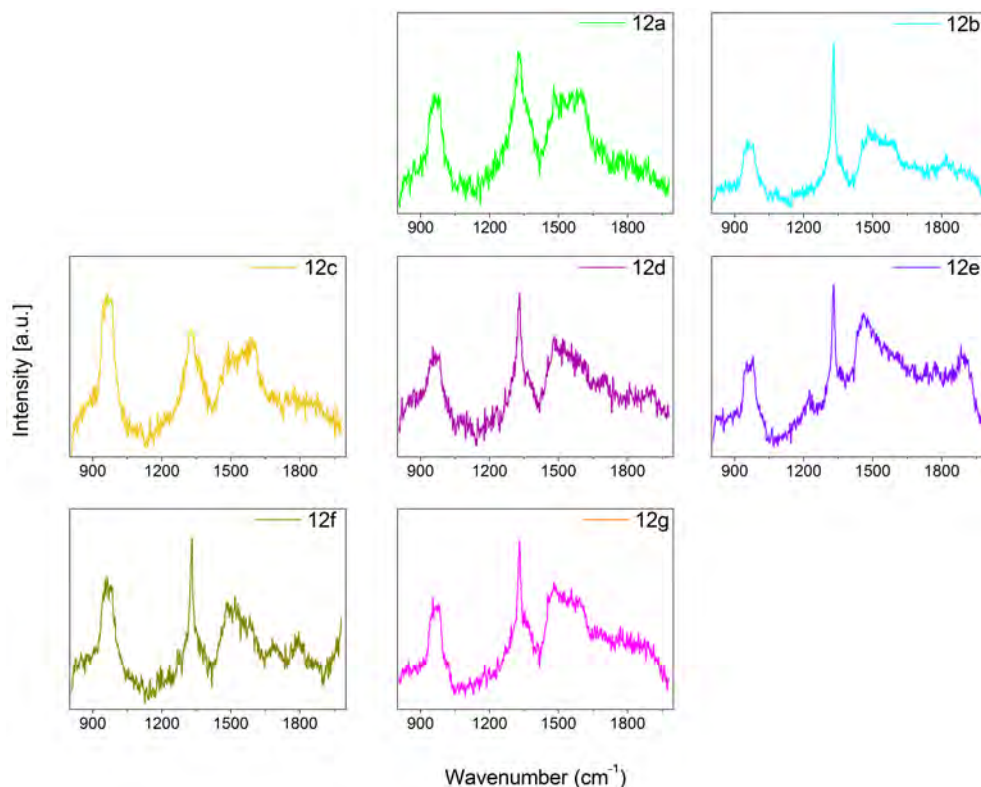


**Figure 6.14:** Raman spectra of samples 12a to 12g showing the influence of the pulse settings.

Analysis of the Raman spectra shown in figure 6.14 and 6.15 gives some more information on the diamond quality. The estimated  $sp^3$  fractions are shown in table 6.9 and table 6.10 and confirm the trends discussed based on the SEM images. With the use of the substrate heater the diamond Raman peak widens, and the D band increases. The highest quality was obtained for sample 12b grown at 40 kHz, 40 % and 5 kW peak power.

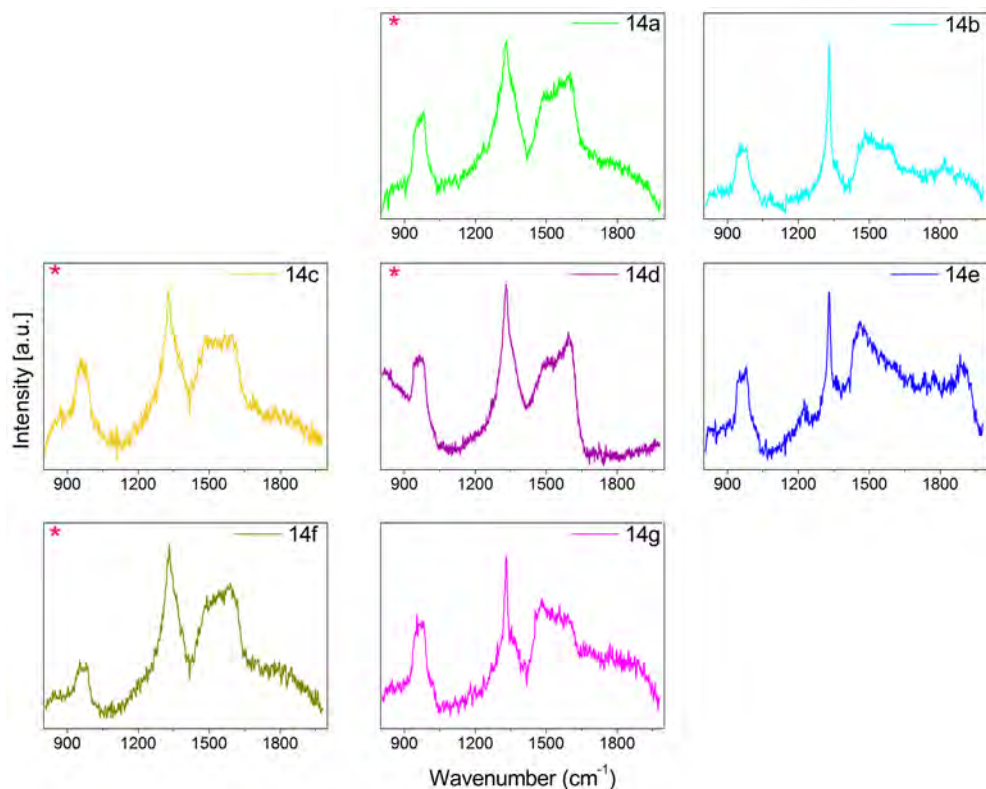


**Figure 6.15:** Raman spectra of samples 14a to 14g grown with constant temperature showing the influence of the pulse settings. The samples that were heated externally to obtain this temperature are indicated with a pink asterisk.

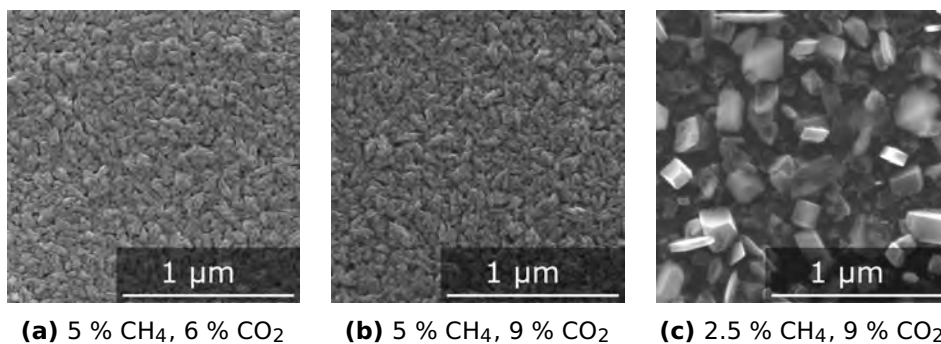
**Table 6.9:**  $sp^3$  fraction and growth rate of samples 12a to 12g. See table 6.8 for the growth conditions.

Sample Code	$sp^3$ fraction	Growth rate (nm/h)
12a	$0.99 \pm 0.6$	28
12b	$0.98 \pm 0.4$	22
12c	$0.99 \pm 0.4$	26
12d	$0.98 \pm 0.8$	31
12e	$0.99 \pm 0.7$	25
12f	$0.98 \pm 0.7$	36
12g	$0.90 \pm 1.2$	46

**Table 6.10:**  $sp^3$  fraction and growth rate of samples 14a to 14g. See table 6.8 for the growth conditions.

Sample Code	$sp^3$ fraction	Growth rate (nm/h)
14a	$0.99 \pm 0.1$	18
14b	$0.98 \pm 0.4$	22
14c	$0.98 \pm 0.4$	22
14d	$0.99 \pm 0.5$	25
14e	$0.99 \pm 0.7$	25
14f	$0.99 \pm 0.1$	23
14g	$0.90 \pm 1.2$	46

Based on the results of Taylor *et al.*, an increase in  $CO_2$  concentration could possibly shift the diamond morphology towards bigger and more faceted grains.<sup>[105]</sup> Therefore, first the amount of  $CO_2$  was increased and then the relative carbon concentration was decreased by a reduction in  $CH_4$ , for samples 16a, 16b and 16c. The SEM images of these samples, shown in figure 6.16, demonstrate a clear increase in grain size and faceting upon increase of the  $CO_2$  and decrease of the  $CH_4$  concentration. As shown in figure 6.17, Raman spectroscopy confirms a very high quality was obtained for sample 16c. However, it seems like the layer still contains pin-holes.

**Figure 6.16:** SEM images of samples 16a, 16b and 16c grown at 40 kHz, 40 % duty cycle, 5 kW peak power, 2.5 kW average power and around 380 °C.

During the pulse on-time, reactive species are activated, and it has been shown that the concentration of atomic hydrogen is higher in pulsed mode



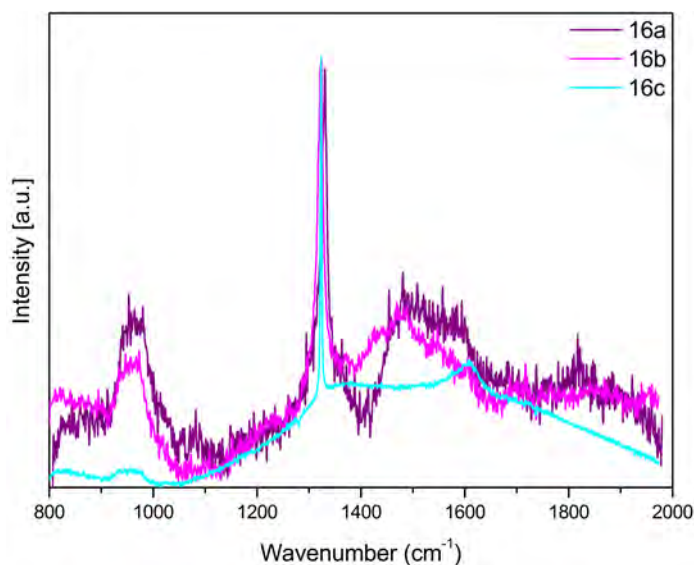


**Figure 6.17:** Raman spectra of samples 16a to 16c. The growth conditions are shown in figure 6.16.

than in continuous mode and, in addition, increases with duty cycle. So, based on the atomic hydrogen concentration only, an improvement in the layer quality is expected in pulsed mode at the frequencies and duty cycles used here.<sup>[100,105]</sup> This was not the case, because we haven't considered the growth radical. The creation of the CH<sub>3</sub> radical depends on the thermal dissociation of CH<sub>4</sub>, which is influenced by the average power. Therefore, it is argued that multiple growth windows exist for good quality diamond. As long as the pulse settings match the growth conditions, and thus both atomic hydrogen and methyl radicals are present in a ratio that leads to the perfect synergy of nucleation and etching, high quality grains are obtained. In order to fully understand and explain the growth mechanism, infrared laser absorption spectroscopy and Langmuir probe measurements should be used estimate to the CH<sub>3</sub> radical concentration and to gain insight on the plasma electron density and electron temperature.

### 6.3 Diamond membranes

The key to making sensitive pressure sensing membranes is the minimisation of thermal stress within the deposited diamond films, as discussed in the previous chapter. Equation 5.22 shows that diamond growth at low temperatures ensures a lower degree of thermal stress. This section will therefore discuss membrane fabrication from diamond films grown on glass at low temperatures with linear antenna technology. 200 nm thick nanocrystalline diamond films were deposited both on S-AF45 and CE2000 glass. The growth conditions were the following: 2,5 % CH<sub>4</sub> and 6 % CO<sub>2</sub>, 410°C, 0,18 Torr, 2,7 kW. The morphology, characteristic for NCD grown at low temperatures with linear antenna technology, is shown in figure 6.18 and will be discussed in detail in chapter 7.

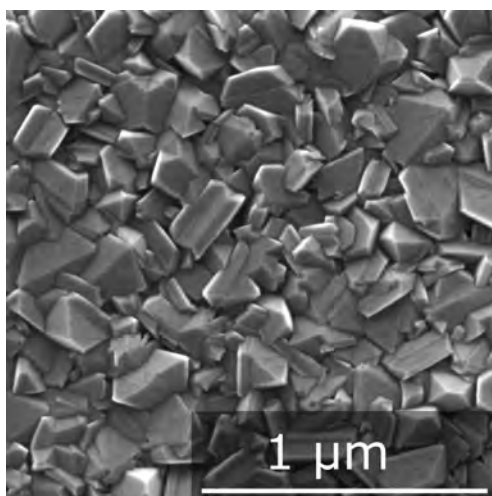


**Figure 6.18:** SEM image showing the morphology of NCD grown at 2,5 % CH<sub>4</sub> and 6 % CO<sub>2</sub>, 410°C, 0,18 Torr, 2,7 kW.

The fabrication of membranes of these NCD films is more difficult compared to NCD films grown in ASTeX systems, presumably due to their particular morphology. The thin, flat plates are weak spots for the etching fluid. From cross-sectional view (see chapter 7, figure 7.1e), it is clear that the films have empty voids close to these plates which can cause the film to collapse once the diamond is reached, as shown in figure 6.19a.

Therefore, for future membrane fabrication it is recommended to use the deposition conditions of sample 6a, (see figure 6.6) to avoid plate formation, although the temperature is higher at 2.5 cm distance between the antennas and the sample.

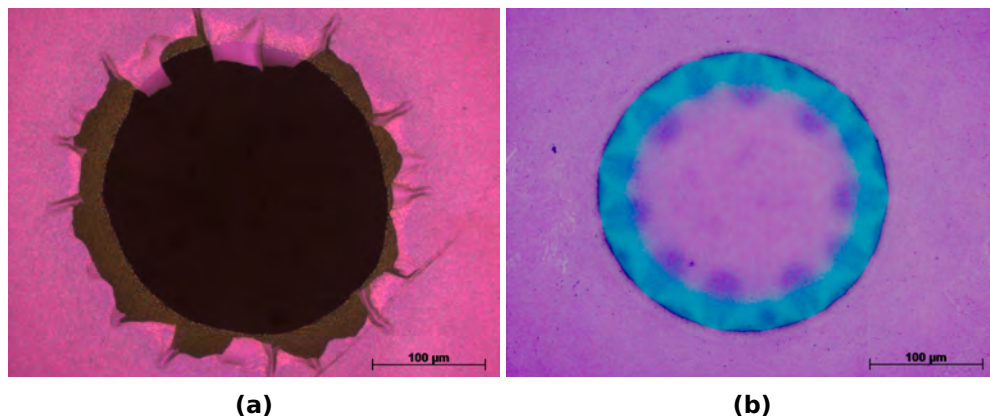


**Figure 6.19:** Optical image of a) a broken NCD (pink) membrane on CE2000 glass (brown) and b) an NCD membrane 255  $\mu\text{m}$  diameter on S-AF45 glass, both grown with linear antenna technology at 410°C.

Nevertheless, one membrane with a diameter of 255  $\mu\text{m}$  on S-AF45 glass was fabricated successfully as shown in figure 6.19b. Compared to the membranes previously made on S-AF45 glass in chapter 5, this membrane appears to be less wrinkled, i.e. the wrinkles are less pronounced. If the circumference of the membrane is divided by the number of wrinkles along the circumference, however, it is found that the wavelength of the wrinkles is about 29  $\mu\text{m}$ , which is shorter than the previously reported 33  $\mu\text{m}$  of B:NCD membranes on S-AF45 glass, indicating that, although the growth was performed at lower temperature, the membrane grown in the linear antenna system contains more compressive stress. Similar to the results in chapter 5, the underlying glass substrate is responsible for compressive stress. With Raman spectroscopy, the diamond peak position was evaluated and compared for position 1, i.e. attached to the glass substrate and position 2, released as a membrane, as shown in figure 6.20. The diamond Raman peak shifts to lower wavenumber ( $3.1 \pm 0.5 \text{ cm}^{-1}$ ) going

from position 1 (NCD film attached to the glass substrate) to position 2 (membrane). The corresponding estimated compressive stress in the diamond film imposed by the substrate is  $(1.8 \pm 0.3)$  GPa, which is higher than the compressive stress for B:NCD membranes on S-AF45 glass, i.e.  $(1.2 \pm 0.5)$  GPa. The location of the diamond peak at values around  $1332 \text{ cm}^{-1}$  compared to values around  $1320 \text{ cm}^{-1}$  in chapter 5 clearly shows the effect of boron doping on the peak position. This low temperature membrane is undoped and boron doping of the previous samples lead to tensile stress, i.e. irrespective of the thermal compressive stress. For working pressure sensing devices boron doping is required and feasible, since Taylor *et al.* have reported dopant concentrations around  $2 \cdot 10^{21} \text{ cm}^{-3}$  leading to a conductivity of  $20 \text{ S} \cdot \text{cm}^{-1}$  using linear antenna technology for temperatures below  $650 \text{ }^\circ\text{C}$  and B/C ratios of 15 000 ppm in the gas phase.

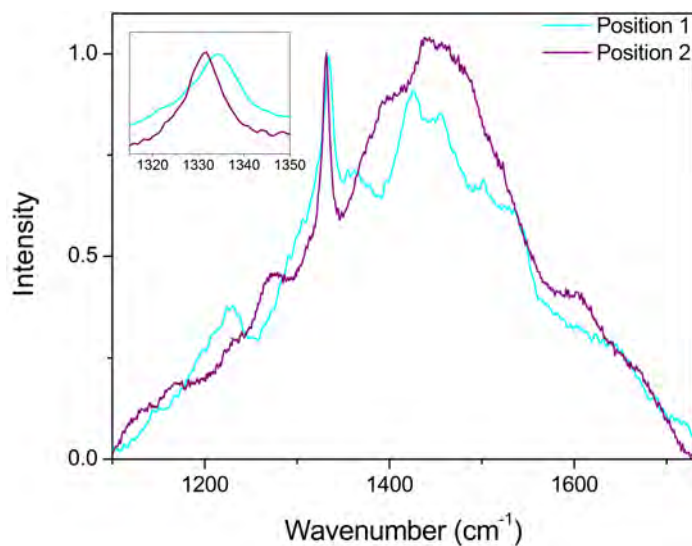


**Figure 6.20:** Raman spectrum of the NCD film attached to the S-AF45 glass substrate (Position 1) and released to form a membrane (Position 2). The spectra shown are representative spectra, for each position (1 and 2) measurements were done at three different spots.

### 6.3.1 Stress dependence of the morphology

In order to determine how this particular morphology, i.e. containing flat diamond plates influences the stress in the diamond layers, the stress level was evaluated for four different NCD layers by means of Raman spectroscopy and surface curvature measurements. For the morphologies shown in the SEM images in figure 6.21, the stress determined via surface curvature measurements was plotted versus the diamond Raman peak position in figure 6.22. The particular morphology, i.e. plates versus

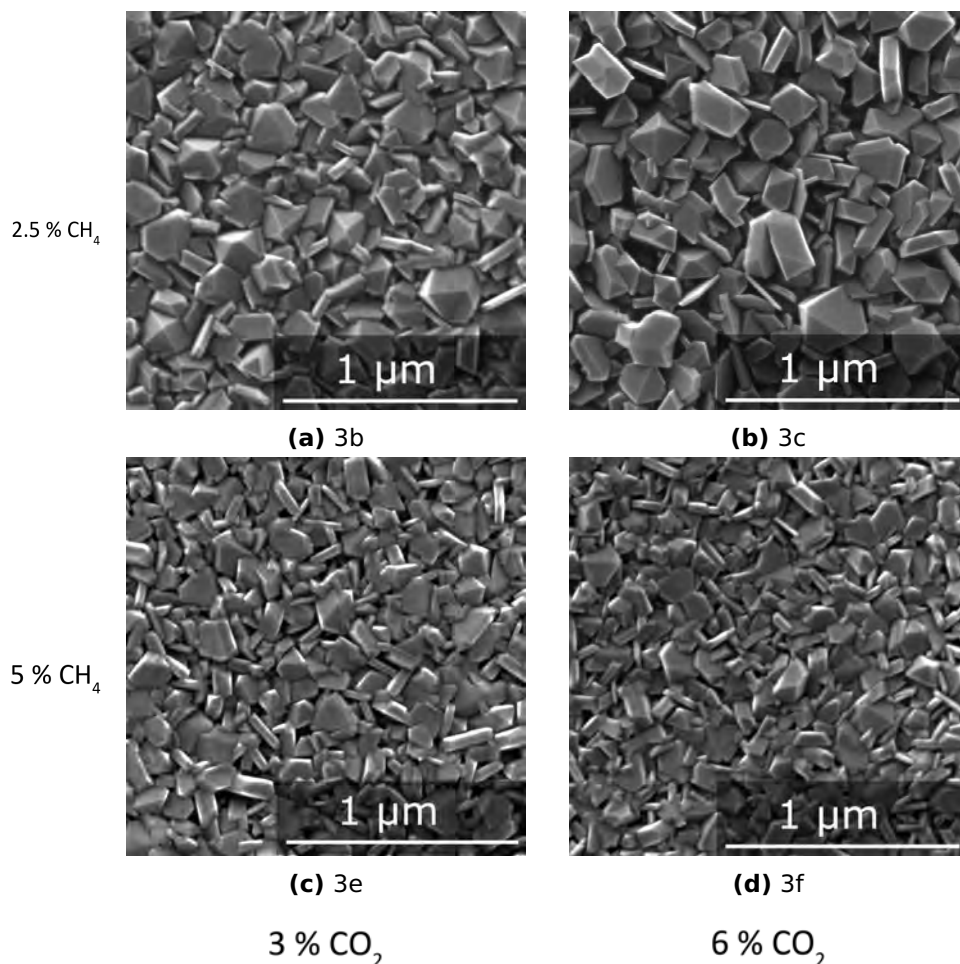


**Figure 6.21:** SEM images of samples 3b, 3c, 3e and 3f. Their corresponding growth conditions can be found in table 6.1.

octahedral particles, and the size of the grains is controlled by careful selection of the deposition parameters. These results confirm that the NCD layers are compressed due to the difference in thermal expansion coefficient between Si and diamond. Moreover there is an influence of the morphology on the stress level. Normally it is expected that the stress increases with the grain size, here, however, the stress is lowest in sample 3c (figure 6.21) with the largest grain size.

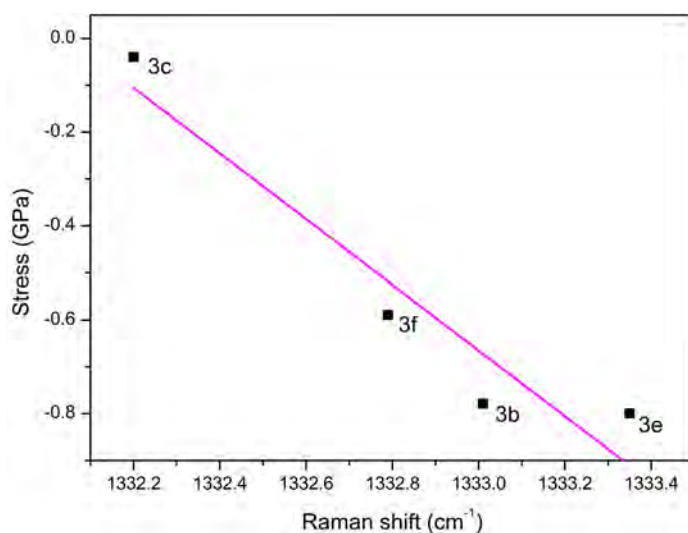


**Figure 6.22:** Plot of the diamond Raman peak position versus the calculated stress from surface curvature measurements for samples 3b, 3c, 3e, and 3f and Their corresponding growth conditions can be found in table 6.1.

From X-ray diffraction some additional information on the diamond layer can be gained (see figure 6.23). Traditionally, diffraction spectra of nanocrystalline diamond films show  $\langle 111 \rangle$ ,  $\langle 220 \rangle$ ,  $\langle 311 \rangle$  and  $\langle 400 \rangle$  reflections clearly, which indicates a crystalline diamond phase with a distribution of crystal orientations over the diamond grains. In a diffraction spectrum of a sample in which co-deposition of diamond plates and octahedral grains occurred, only peaks for  $\langle 220 \rangle$  and  $\langle 311 \rangle$  reflections are observed. Since TEM clearly confirms the presence of  $\{111\}$  terminating facets for the plate type morphology (see next chapter), their absence in the diffraction spectrum can be interpreted as the plates being mostly ori-

ented normal to the substrate surface, i.e. XRD insensitive. Hence the plates have a preferred vertical orientation onto the substrate. Moreover there is a shift for both the  $\langle 220 \rangle$  and  $\langle 311 \rangle$  reflections in opposite direction. Shifts in XRD spectra can be related to stress, since the scattering angle  $\theta$  depends on the unit cell, i.e. distance between the atoms. When a material is strained, the crystal lattice is compressed or stretched, which changes the inter-planar spacing of the  $hkl$  lattice planes and causes a shift in the diffraction spectrum. Based on Bragg's law (equation 3.4), a shift towards higher (lower) scattering angle is expected upon compression (stretching) of the lattice.<sup>[204]</sup>

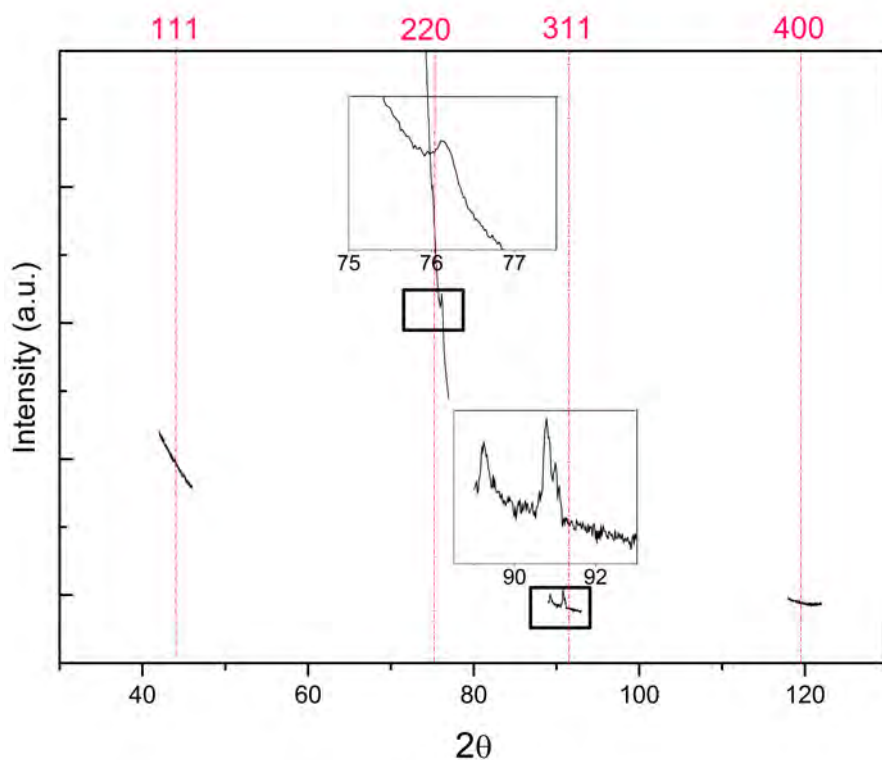


**Figure 6.23:** XRD spectrum of a 130 nanometre thick sample grown with 2.5 %  $\text{CH}_4$  and 6 %  $\text{CO}_2$ , at 410 °C, 2.8 kW and 5 cm substrate table-antenna distance (sample 3c in figure 6.21). The pink dotted lines indicate the theoretical location of the labelled diffraction lines.

In the particular case where an opposite shift takes place for the present crystal orientations, it could mean that one crystal orientation is elongated at the cost of the compression of another. In our case the  $\langle 220 \rangle$  direction is compressed while the  $\langle 311 \rangle$  orientation is elongated. For gold, the stress of the film has been reported to depend on the ratio of the diffraction peaks of  $\langle 200 \rangle$ -oriented grains and  $\langle 111 \rangle$ -oriented grains.<sup>[205]</sup> Films with (200)-oriented grains show the lowest compressive stress, while those with  $\langle 111 \rangle$ -oriented grains have the highest tensile stress. By varying the ratio of  $\langle 111 \rangle$  versus  $\langle 200 \rangle$  grains, the stress could be changed from tensile to compressive. Similarly, the ratio of various crystallographically oriented grains is thought to be responsible for a decrease in stress with an increase in grain size in NCD samples with co-deposition of plates and octahedral grains.

## 6.4 Conclusion

The different growth regimes of renucleated and faceted NCD growth can be related to the deposition conditions; pressure, gas composition, sample-to-antenna distance, power and temperature. The main findings of this chapter are listed here:

- Lower pressures ( $< 0.23$  Torr) are beneficial for the growth of faceted, crystalline NCD layers with low  $sp^2$  content, because the plasma is more extended towards the substrate and the recombination rate of active species is reduced compared to higher pressures. Further improvements could be made by replacement of the pump and/or flow controllers, since now we are controlling the pressure by the incoming flow at maximum pumping speed. An increase in flow and available active species could have a tremendous effect on the plasma chemistry and growth rates.
- Adding oxygen to the gas phase allows for the growth of high quality diamond films with linear antenna technology due to its benefit in



achieving low gas pressure and low temperature.

- Low methane concentrations (2.5 %) and high CO<sub>2</sub> concentration (6 %) show an optimal interplay between nucleation (both sp<sup>3</sup> and sp<sup>2</sup>) and etching of sp<sup>2</sup> phases leading to faceted layers with large average grain sizes (50-60 nm).
- The distance between the sample and the antennas needs to be optimised for particular growth conditions so etching doesn't lead to pinholes, but is efficient enough for high quality diamond growth, since at further distances the amount of active species decreases.
- At higher powers, more gas species are activated, which means the atomic hydrogen concentration is higher and this leads to an increase in grain size and faceting.
- Externally supplied heat in the form of a substrate heater is not able to excite molecules to the same energy levels as the input microwave power and thus leads to a less faceted, renucleated type of morphology.
- The linear antenna system is very sensitive to carbon deposition on the quartz tubes. These deposits can limit microwave penetration and microwave coupling to the plasma which leads to lower plasma density of the same settings. In addition, a silicon carbide layer is necessary to prevent extreme etching of the quartz tubes and with the addition of oxygen into the chamber.
- Pulsing shows great potential to grow high quality layers with a lower energy input and heating of the substrate table, thereby reducing the thermal load onto sensitive substrate materials. However, a pinhole free high quality layer has not been obtained up to now. The obtained morphologies are similar for identical average powers, but an increase in duty cycle and peak power seems to lead to more faceting and less cauliflower-like morphologies. Nevertheless, the best results

were obtained for a sample grown with only 5 kW peak power at 40 kHz and a duty cycle of 40%. A further increase in CO<sub>2</sub> content leads to well-defined crystals with large crystal sizes, however without complete coverage.

In summary, pulsed wave modes have great potential towards a better diamond quality at low temperatures with low thermal loads onto the substrate, because of a non-linear microwave absorption.

Up to now diamond membranes made from samples grown at low temperatures with linear antenna technology appear to be more difficult to prepare and more compressed than those deposited with ASTeX technology. This is presumably due to the plates within the NCD film. In addition, there is a dependence of the stress in the film on the morphology, contrary to what is expected based on grain size, i.e. the stress can be controlled by the deposition conditions. For future work, films without the presence of diamond plates can be prepared, to facilitate the fabrication process and assess the stress level for this morphology. In addition, B:NCD films can be prepared in the Czech Republic in order to fabricate sensitive pressure sensing devices.



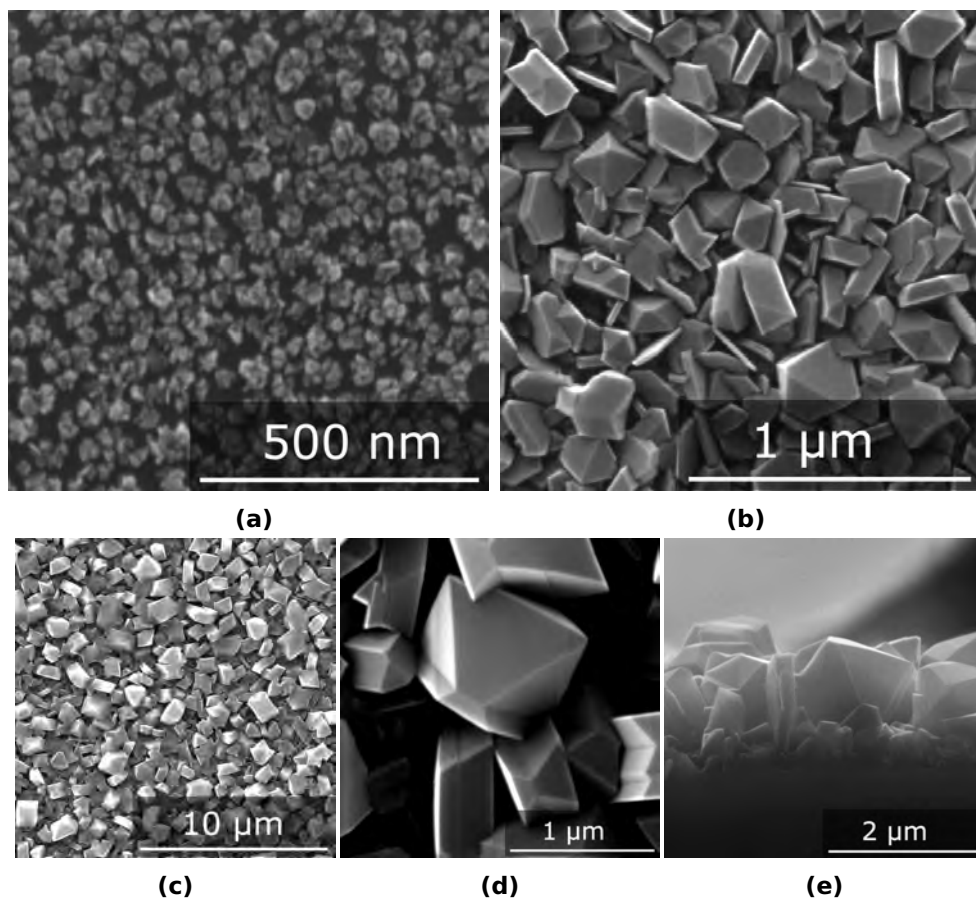
## Chapter 7

# Co-deposition of diamond plates and octahedral grains

This chapter addresses the co-deposition of high quality plate-like and octahedral diamond grains in nanocrystalline films with the use of the linear antenna system. In contrast to previous reports claiming the need of high temperatures ( $T \geq 1000 \text{ }^\circ\text{C}$ ),<sup>[129,130,132,133]</sup> low temperatures ( $320 \text{ }^\circ\text{C} \leq T \leq 410 \text{ }^\circ\text{C}$ ) were sufficient to deposit diamond plate structures. According to Butler *et al.*, once a three-atom bridge is formed it isomerises rapidly between the boat and chair conformation until it is locked in either of the two positions by the addition of a fourth carbon, as described in chapter 4. The created nucleus has almost 50 % chance of being a stacking fault because of the similarity in energy. Although, Butler *et al.* postulate that this is probably the only mechanism for twin formation during growth of diamond by CVD, other possible mechanisms will be introduced and discussed in this chapter.

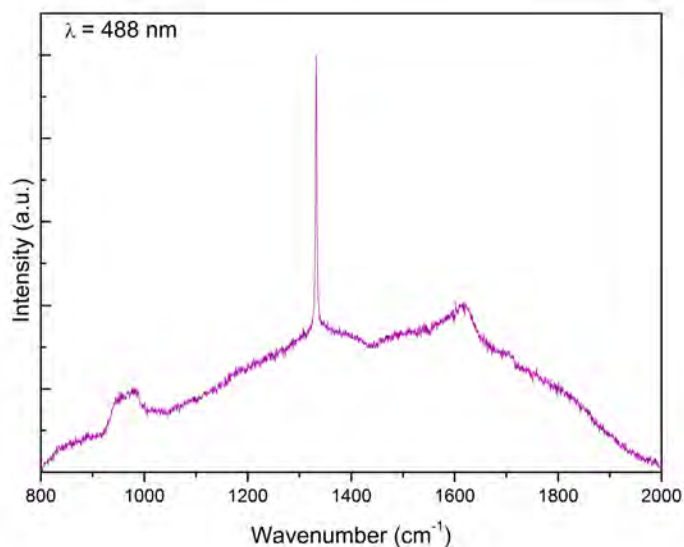
## 7.1 Characterisation

Figure 7.1b shows the surface morphology of an NCD covered Si sample grown for 18h in the LA system (410 °C, 0.17 Torr, 2.8 kW CW power, 2.5 % CH<sub>4</sub> and 6 % CO<sub>2</sub>, no external heating).



**Figure 7.1:** SEM images of samples grown at 410 °C, 0.17 Torr, 2.8 kW CW power, 2.5 % CH<sub>4</sub> and 6 % CO<sub>2</sub> without external heating. a) Initial stages (1h) of growth: the development of plate structures has started already. b) A 130 nm thick NCD layer (18h growth time) consists of both octahedral and plate-type diamond grains. c) A 1.5 μm thick NCD layer (64h of growth) still consists of both octahedral and plate-type diamond grains. Prolonged growth times give rise to similar morphologies with larger grains. d) Zoom of (c), e) Cross-sectional view which clearly demonstrates the plate structures are present at the first stages of growth and continue to grow.

The resulting 130 nanometre thick NCD layer is faceted and consists of both octahedral and plate-like diamond grains with a homogeneous distribution. The diamond plates are oriented away from the Si substrate, i.e. the plates are not parallel to the substrate but found in a variety of orientations. Both the plates and the octahedral particles are faceted, suggesting their crystalline nature. Each plate shows a uniform shape with a high length-to-width or aspect ratio, i.e. between 5 and 15. If the growth is interrupted after a short time (1h), some features with a high aspect ratio seem to have started to develop as shown in figure 7.1a, i.e. the plates develop at the start of the growth, together with octahedral diamond particles. If the growth is continued for 64h, the layer evolves into microcrystalline diamond (figure 7.1c-e). In order to confirm the nanocrystalline layer consists of diamond Raman measurements were performed (figure 7.2).



**Figure 7.2:** Raman spectrum of a 130 nm thick NCD sample grown at 410 °C, 0.17 Torr, 2.8 kW CW power, 2.5 % CH<sub>4</sub> and 6 % CO<sub>2</sub> without external heating.

The intense signal around  $1332\text{ cm}^{-1}$  and the very low intensity of peaks situated around  $1480$  and  $1550\text{ cm}^{-1}$ , confirm that a high quality diamond layer with a very low amount of  $\text{sp}^2$  bonded carbon was deposited. The estimated  $\text{sp}^3/\text{sp}^2$  ratio is  $(0.98 \pm 0.05)$ .<sup>[117]</sup>

The NCD layer was further analysed via TEM to characterise its crystallography and morphology. Similar to the SEM images, plan view annular dark field (ADF) and bright field (BF) TEM (figure 7.3) show the co-existence of both octahedral and plate structure diamond grains.

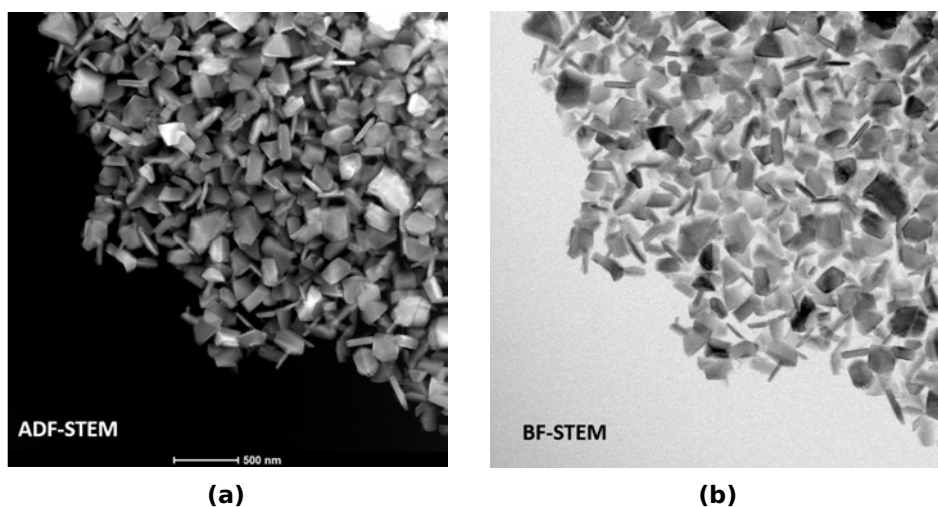


**Figure 7.3:** a) Plan view annular dark field and b) bright field scanning TEM image of a 130 nm thick NCD layer deposited with an LA MW PE CVD system showing the presence of both octahedral and plate diamond grains.

Cross-sectional BF TEM studies reveal both plates and octahedral particles (figure 7.4a). High resolution TEM shows that the plates are terminated by large  $\{111\}$  surface facets (figure 7.4b). The inset in figure 7.4b shows the corresponding selected area diffraction (SAD) pattern. This diffraction pattern corresponds to the diffraction pattern of cubic diamond when the grain is imaged in the  $[011]$  zone axis. This plate diamond grain (with  $\{111\}$  terminating facets) is connected to the next grain via a  $\{111\}$  plane. The octahedral grain in region c mainly has  $\{111\}$  terminating facets. This grain also contains a lot of stacking faults, which can be recognised by the lines in the fast fourier transform (FFT) pattern from that area

(7.4c left inset). The less faulted part of that grain shows a cubic diamond SAD pattern in the  $[011]$  zone axis (figure 7.4c right inset), and the larger fuzzy dots pattern<sup>1</sup> in the HRTEM image are an indication of stress in the grain.

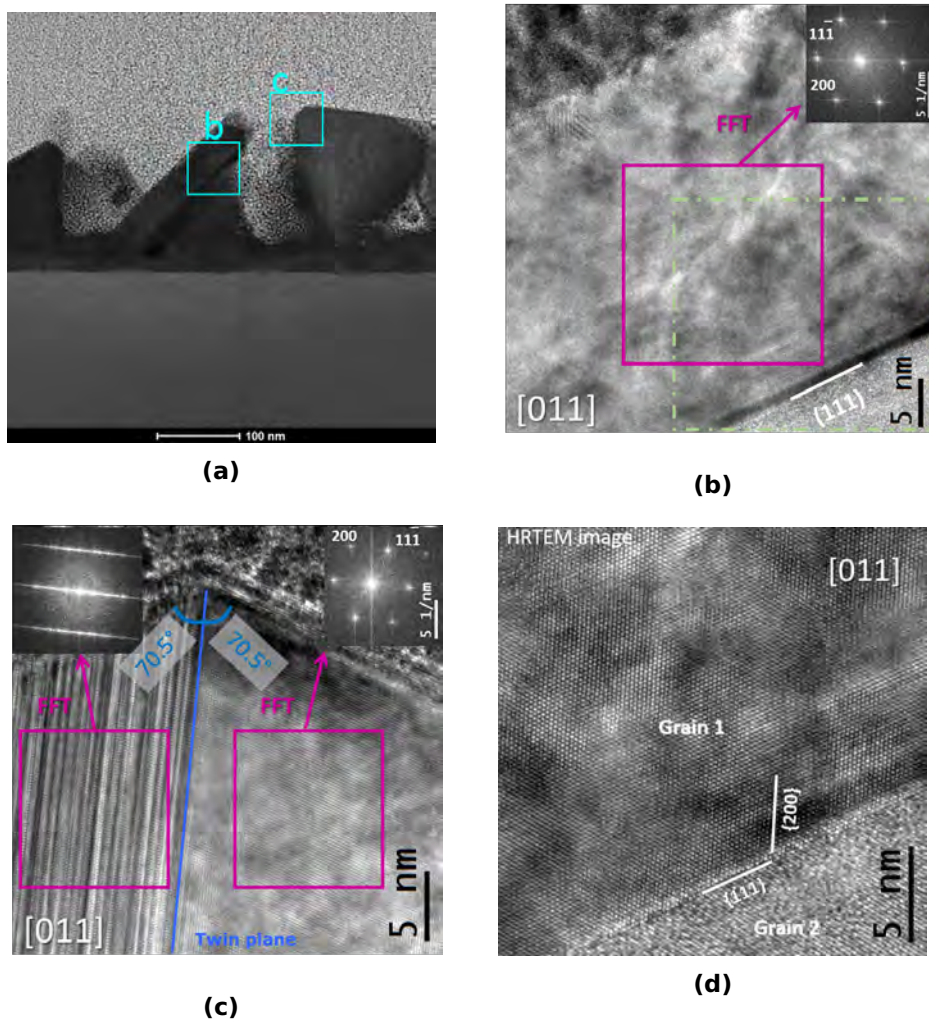


**Figure 7.4:** a) Bright field TEM image. The blue squares indicate the zones examined in (b) and (c), but rotated 20° clockwise. b) High resolution TEM image of a plate grain. c) High resolution TEM images of an octahedral grain. d) Zoomed HRTEM image of the area indicated by the dotted green rectangle in (b).

<sup>1</sup>Bend contours: the TEM specimen is slightly bent at various positions, which means Bragg's law is not fulfilled at these spots and this leads to a difference in diffraction contrast.



The different areas are joint by a twin plane, indicated in blue, which demonstrates how two  $\{111\}$  planes at the edge of a grain appear to have a  $141^\circ$  angle, that is actually the sum of two  $70.53^\circ$  angles between the twin plane and the edge plane.

Figure 7.4d, shows that the plate grain lays straight in the  $[110]$  zone axis, while the neighbouring grain has a different orientation. Moreover, the grain boundaries are shown to be quite sharp, which is an indication of very little disorder in between the grains.

A simplified model of the diamond plate structure is given in figure 7.5. The model shows the diamond structure in the bulk material at the twin planes. The structure of the ridge edge of the plates is a mixture of  $\{100\}$ ,  $\{110\}$  or  $\{111\}$  (or others) depending on the angle these planes make with the twin planes (see table 3.2). The angle a  $\{111\}$  plane makes with the  $\{111\}$  twin plane, for instance, is  $70.53^\circ$ . In order to visualise how this model leads to diamond plates, figure 7.5b shows the stacking of twinned  $\{111\}$  planes in the  $[110]$  viewing direction. From this figure it can be understood how twinning along  $\{111\}$  faces can lead to an atomic stacking as shown in figure 7.5c.

The composition and atomic structure of the diamond plates was examined with electron energy loss spectroscopy (EELS) characterisation, as shown in figure 7.6. The near-edge structure of the carbon K-edge in EELS (figure 7.6c) confirms that the grains are indeed diamond, i.e. in an  $sp^3$  chemical bonding state. Moreover there is a very small shoulder at 285 eV at the edge of the grain corresponding to the  $\pi^*$  orbital of  $sp^2$  carbon, i.e. there is a very low amount of  $sp^2$  in the grain boundary. Thus, EELS confirms that the grains consist of high quality diamond and that the grain boundaries are very clean and sharp with a very low amount of  $sp^2$  bonded carbon. Elemental mapping of the NCD layers via EELS reveals that the grains consist of diamond, but that they are covered with a silicon dioxide layer. The amorphous carbon layer on top of the diamond layer is due to sample preparation.

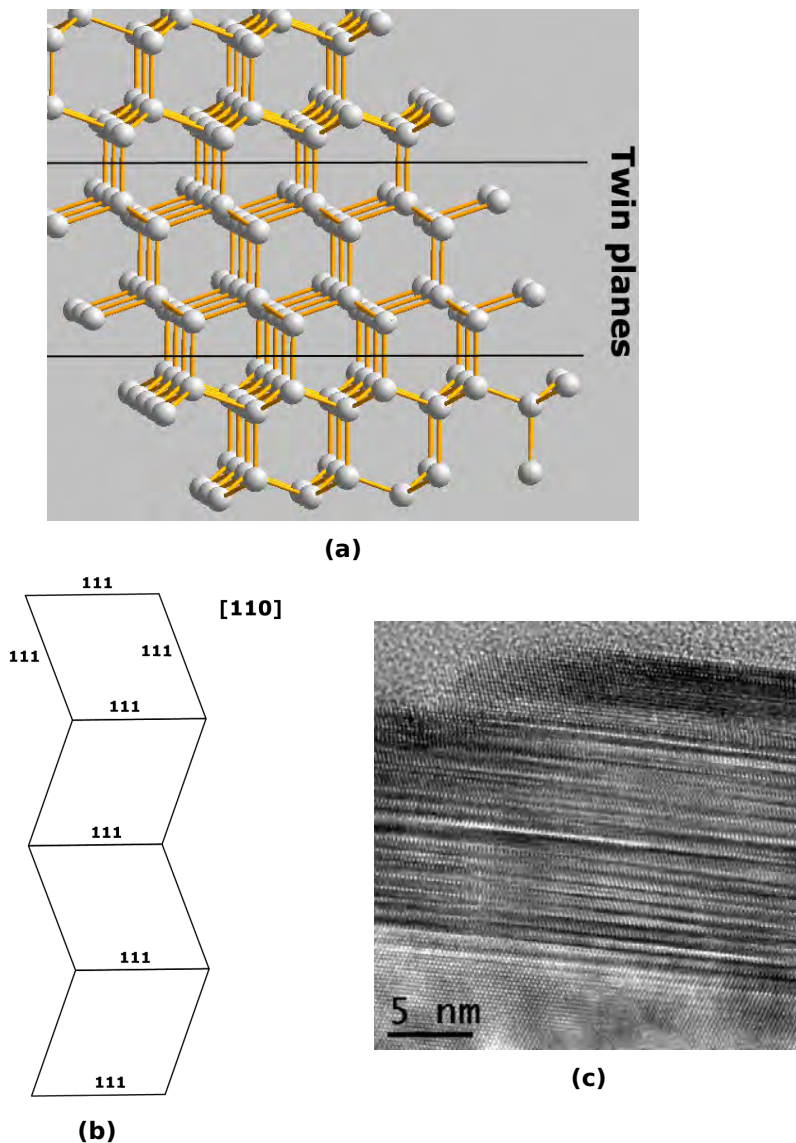


**Figure 7.5:** a) Simplified model of the faulted plate structure based on a very limited number of carbon atoms. Hydrogen atoms are not shown here, but are present at surface carbons after growth. The cubic diamond structure is interrupted by twin planes, i.e. hexagonal diamond layers, that give rise to plate-like grains. b) Schematic view of  $\{111\}$  planes in the  $[110]$  direction, showing parallel twin planes. c) HRTEM image of a faulted diamond region, showing stacked  $\{111\}$  planes.

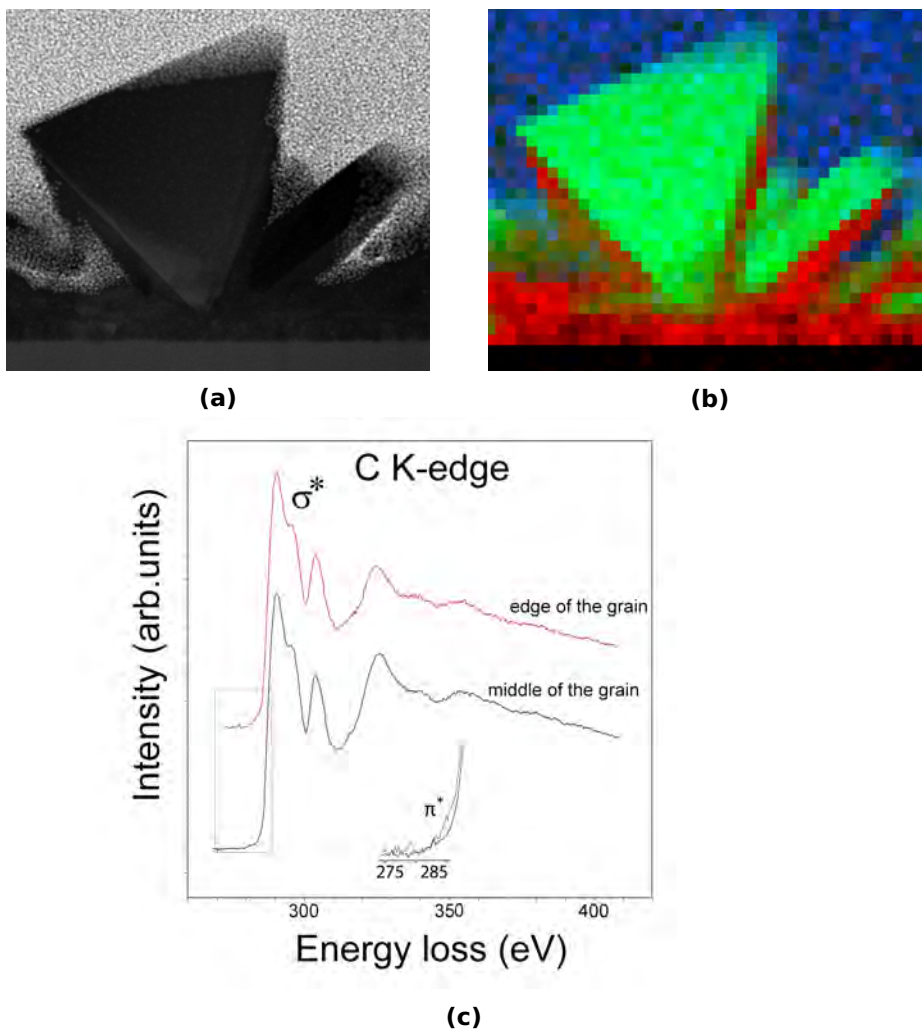


**Figure 7.6:** a) ADF-STEM image of an octahedral grain and a plate, and b) corresponding EELS map showing amorphous carbon (blue), diamond (green) and oxygen, related to silicon dioxide (red). c) Near-edge structure of the carbon K-edge in EELS showing a very small  $sp^2$  contribution at the edge of the grain.

Energy-dispersive X-ray spectroscopy (EDX) mapping, in figure 7.7, confirms that the diamond particles are clearly covered with a silicon dioxide layer. This layer can originate either from the Si substrate, that is being resputtered during sample preparation or it is co-deposited with the diamond layer and is then probably coming from the quartz tubes, surrounding the antennas. In order to clarify the origin of Si, an NCD layer

was prepared on a molybdenum substrate. EDX mapping also shows the presence of a Si layer on a Mo substrate (figure 7.7e), which means Si is most probably being etched from the quartz tubes in oxygen-rich growth conditions, i.e. in presence of CO<sub>2</sub>, and is co-deposited with the NCD layer.

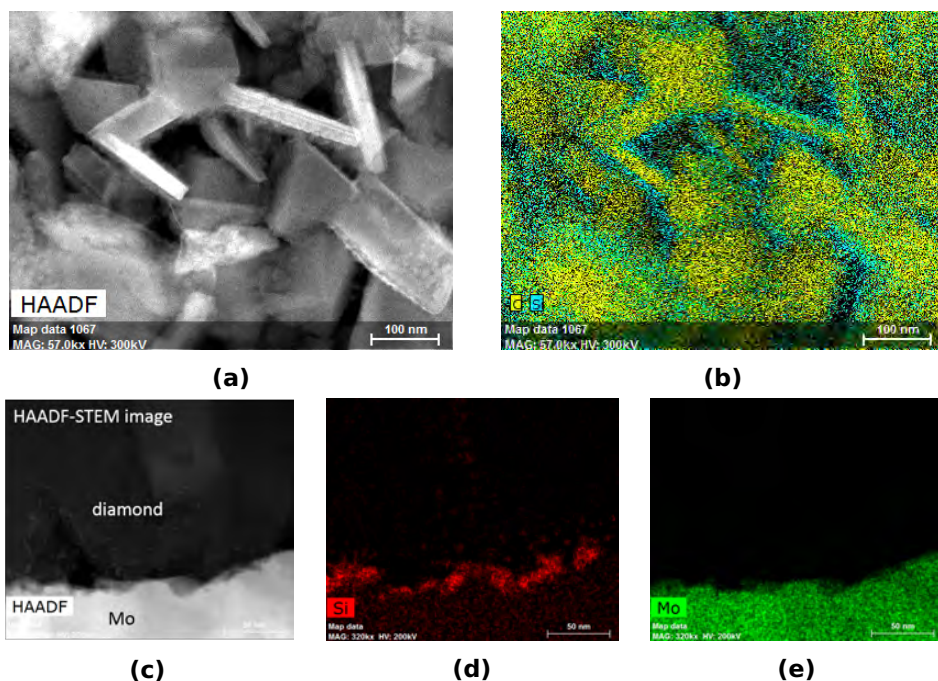


**Figure 7.7:** a) High-angle annular dark-field image of an NCD film on Si showing octahedral grains and diamond plates, b) corresponding EDX map, c) cross-sectional high-angle annular dark-field image of an NCD film on Mo showing octahedral grains and diamond plates, d) corresponding EDX map showing the Si content and e) corresponding EDX map showing the Mo content.

## 7.2 Proposed mechanism for the initial stages of the development of plates

### 7.2.1 Impurity induced formation of stacking faults

As discussed in chapter 4, stacking faults at the start of the deposition process are the driving force behind the development of the anisotropic plate morphology, since they create self-perpetuating growth steps. Nevertheless, it is still unclear why these stacking faults develop. As shown in figure 7.8, diamond plates can be grown under conditions with a high amount of excited species and at high temperatures, in previous experiments performed in Hasselt with an ASTeX PDS-17 system. The plates formed on a

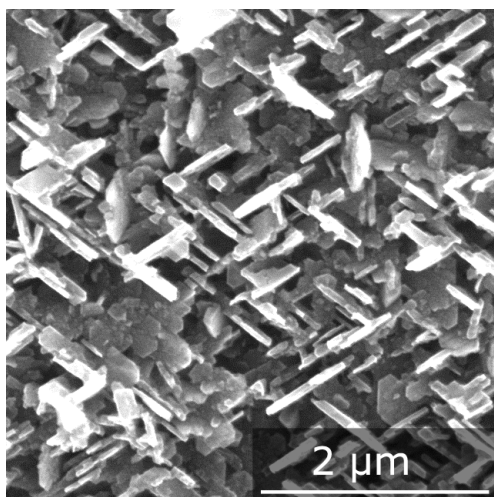


**Figure 7.8:** SEM image of a layer deposited with an ASTeX resonant cavity MW PE CVD system at a temperature above 1150 °C with the presence of 500 ppm PH<sub>3</sub> and 1 % CH<sub>4</sub> in H<sub>2</sub> on a (110) HPHT diamond single crystal substrate polished with a 10° off-angle towards (100).

diamond single crystal (110) HPHT substrate polished with a 10° off-angle towards (100) at temperatures above 1150 °C with a CH<sub>4</sub> concentration of 1 % and 500 ppm PH<sub>3</sub>/CH<sub>4</sub>, with the latter gas added to achieve n-type conductivity via P-doping. The plates in this sample make an angle of 70° with each other; thereby confirming that these plates also have {111} ter-

minating facets. And although the growth of {111} facets on (110) crystals has been reported before, the obtained plate morphology is distinctly different from {111}-oriented microfacets that lead to a rough appearance.<sup>[206,207]</sup> These microfacets are induced by polishing of (110) prior to growth, because diamond preferentially chips along the (111) cleavage planes.<sup>[207]</sup> A first suggestion for the development of stacking faults in the presented low temperature experiments is that the conditions used in the linear antenna deposition system resemble the high temperature and low methane concentrations, used in Hasselt as discussed above and previously reported.<sup>[129-133,140,141]</sup> In fact, the LA system can achieve a high electron density ( $>10^{11} \text{ cm}^{-3}$ ), leading to a large amount of active species.<sup>[91]</sup>

Other plausible explanations are based on further analysis of the obtained crystal structure. A first mechanism for the development of these diamond plates is proposed, since a stacking fault consists of one or more layers of hexagonal diamond and the formation mechanism of hexagonal diamond is known. It is important to note that the actual existence of hexagonal diamond is being questioned and it has never been reported to exist as a separate, pure material.<sup>[208]</sup> Németh *et al.* offer experimental evidence to show that what has been considered as hexagonal diamond up to now, is actually faulted and twinned cubic diamond, i.e. comparable to the plates obtained in this work but with a higher degree of faults. This means the proposed mechanism of hexagonal diamond by Kang *et al.* could be considered as a mechanism for the development of faulted cubic diamond.<sup>[209]</sup> Therefore, this model could explain the development of diamond plates in our experiments. In the experiments of Kang and co-workers the deposition is performed on a layer of Al/Ni/Al, which is annealed prior to growth to form nanoparticles. These nanoparticles act as a catalyst for the formation of stacking faults. During the first growth steps, an amorphous carbon film covers the nanoparticles. More specifically, as shown from XRD data, a fullerene encapsulates the nanoparticle. Al nanoparticles are known to improve the formation of fullerenes.<sup>[210]</sup> This

fullerene keeps developing, i.e. adding layers like onion shells, but since at this size nano-diamond structures are more stable than fullerenes, an  $sp^3$  nucleus starts to develop.<sup>[211,212]</sup> The orientation of the plate depends on the location on the fullerene shell where the diamond phase nucleates. If the atom bonds on top, the plate will be (almost) parallel to the substrate, in case of nucleation close to the base of the fullerene, i.e. close to the substrate surface, the plate will be perpendicular to the surface. With this model it is still unclear why the nucleation on a fullerene results in a hexagonal diamond layer instead of a cubic diamond one. Therefore, a closer look into the crystallographic structure is necessary. Simulations of high pressure transformations from hexagonal  $sp^2$  into  $sp^3$  carbon have shown that in order to form cubic diamond a buckling and slipping mechanism of adjacent graphitic layers needs to take place, while for hexagonal diamond no buckling takes place.<sup>[213]</sup> Therefore, at certain interlayer distances it is energetically more favourable to form hexagonal instead of cubic diamond. Experimental results supporting these simulations have been reported by Zhang *et al.*<sup>[214]</sup> Based on these reports and our current results, it could be argued that a similar transition from fullerene to diamond can occur in CVD processes as well.<sup>[215,216]</sup> The assumption that foreign atoms are important for this mechanism to occur is based on the literature reports of diamond plates up to now. Many of the papers that discuss diamond plate formation report the presence of a foreign material during the deposition conditions (see table 7.1).

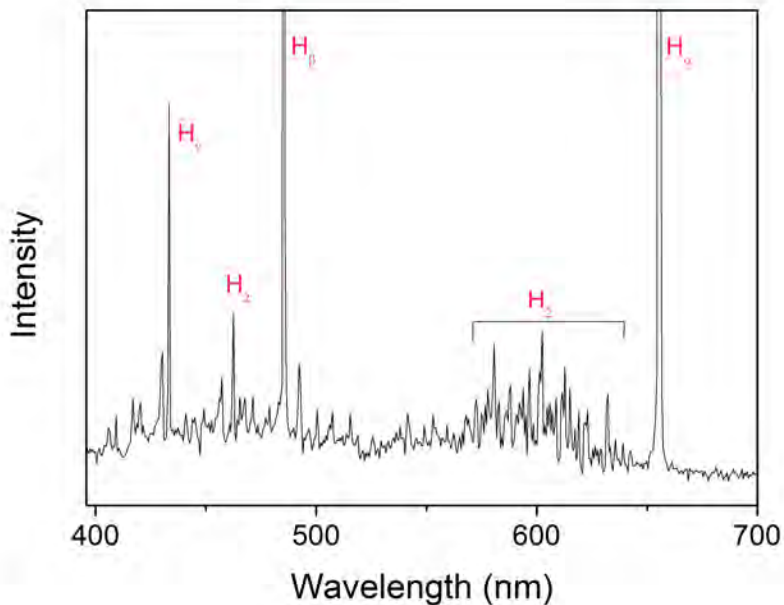
**Table 7.1:** Summary of the important factors for the development of diamond plates.

	Temperature	[CH <sub>4</sub> ]	Foreign material	Deposition system
Angus1992 <sup>[129]</sup>	850 °C	1 %	/	ASTeX PDS 16 MW PE CVD
Lu2004 <sup>[130]</sup>	> 1000 °C	0.667 %	Fe	2.45 GHz ASTeX MW PE CVD
Chen2004 <sup>[140]</sup>	> 1000 °C	3 %	Ni	2.45 GHz ASTeX MW PE CVD
Chen2005 <sup>[132]</sup>				
Lu2005 <sup>[131]</sup>	> 1150 °C	0.667 %	/	2.45 GHz ASTeX MW PE CVD
Chen2008 <sup>[141]</sup>	> 1000 °C	1-3 %	Au/Ge nanodiamond	2.45 GHz ASTeX MW PE CVD
Alekseev2016 <sup>[133]</sup>	1000 - 1100 °C	3 %	/	Direct current discharge PE CVD

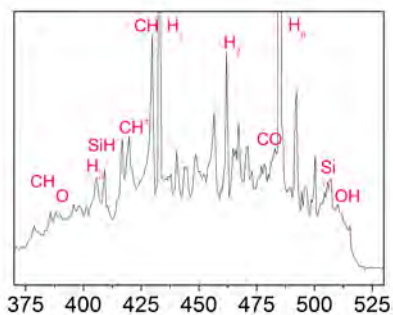
A foreign atom cluster catalyses the formation of a fullerene which later transforms easily into hexagonal diamond because of the lattice similarities of the stacked graphene layers with hexagonal diamond.<sup>[210,217]</sup> However, both cubic and hexagonal diamond nuclei can form because at these sizes diamond is more stable than fullerene.<sup>[211,212]</sup> In this way, cubic diamond with hexagonal stacking faults can develop.

From EDX and EELS, it was clear that Si is present between the diamond grains, which means the quartz tubes are being etched during growth. In addition, the presence of aluminium in the gas phase is very likely, since the chamber walls consist of aluminium and there is a typical content of about 15 ppm of aluminium inside the quartz tubes.<sup>[88]</sup> Optical emission spectroscopy is a powerful tool to reveal the plasma characteristics that might be responsible for the growth mechanisms behind this particular morphology. However, the signals of the elements of interest, Al and Si, are either out of the range of our current set-up or are in a range in which it is difficult to distinguish between other species. Si shows a very strong signal at 288 nm, but the lower range of our set-up is about 320 nm.<sup>[218]</sup> There are some peaks between 409 and 422, that could be assigned to SiH\* as shown in figure 7.9.<sup>[219,220]</sup> In combination with proof for the presence of Si from EDX and EELS, it is very likely that these peaks can be assigned to SiH\*. In addition, the presence of Si in a similar set-up has been shown by Taylor *et al.*, even demonstrating the growth of SiC layers.<sup>[221,222]</sup> For aluminium, the characteristic peak is located at 632 nm, but the peak at this location in the spectrum in figure 7.9a is due to the laser used for in-situ thickness measurements ( $\lambda = 632$  nm).<sup>[218]</sup> Spectra recorded without the presence of the laser only show a very small signal with a low intensity at 632 nm (see spectrum 7.9c), which could be related to the presence of Al. However, this is only speculation since the molecular hydrogen band covers the entire range from 570 - 640 nm.<sup>[93,223]</sup> In addition, a double signal around 395 nm, characteristic for Al, was found in an oxygen etching plasma, possibly confirming the presence of aluminium in oxygen containing atmosphere.<sup>[224]</sup>

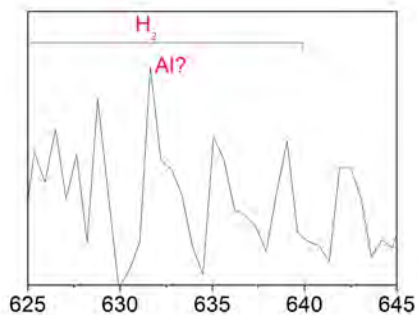




(a)



(b)



(c)

**Figure 7.9:** a) Optical emission spectrum of the plasma with deposition conditions 410 °C, 0.17 Torr, 2.8 kW CW power, 2.5 % CH<sub>4</sub> and 6 % CO<sub>2</sub> without external heating with the use of the laser. b) Zoom of the range between 370 and 530 nm, and c) zoom of the range between 625 and 645 nm without the use of the laser for in-situ thickness measurements.

The presence of impurities is very likely to be the cause of plate formation, but there are some other possibilities next to the catalytic behaviour of atom clusters.

### **7.2.2 Impurity induced blocking layer for the growth of a crystal facet**

A first alternative is the formation of a growth blocking layer on one crystal orientation. This blocking layer can be formed preferentially at one crystal facet because of a better match between the spacing of the available carbon atoms and/or a higher surface energy of that particular facet. The density of surface atoms depends on the crystal facet; i.e. there are  $1.83 \cdot 10^{15}$  surface atoms  $\text{cm}^{-2}$  on  $\{111\}$ ,  $2.23 \cdot 10^{15}$   $\text{cm}^{-2}$  on  $\{110\}$  and  $1.56 \cdot 10^{15}$   $\text{cm}^{-2}$  on  $\{100\}$ .<sup>[225]</sup> These surface atoms can bond with a foreign atom like silicon, which is also a group IV element with a radius of 117.6 pm. The formation of a silicon terminated (100) diamond surface, for instance, has been achieved by the deposition of a silicon adlayer and subsequent annealing.<sup>[226]</sup> The surface energy of the crystal facets depends on the deposition temperature. At lower temperatures,  $\{100\}$  is the most stable and  $\{111\}$  is the most reactive, while at higher temperatures the stabilities are inversed and  $\{111\}$  becomes the most stable crystal facet.<sup>[225]</sup> The exact location of this inversion point depends on the pressure and specific growth conditions, nevertheless in the case that the  $\{111\}$  crystal facets have the highest surface energy they are the most likely planes to bond with Si, thereby forming a capping layer which impedes further growth of this plane and leads to the growth of diamond plates. Similar mechanisms are known to take place during the growth of crystals with the use of CVD techniques and during solution based growth in presence of a surfactant.<sup>[227]</sup>

### 7.2.3 Impurity enhanced etching of a crystal facet

The second alternative for the development of diamond plates is based on enhanced etching of a particular crystal facet. The direct oxidation and corrosion of  $\{111\}$  planes has been reported to occur more easily than that of  $\{110\}$  planes.<sup>[228]</sup> In addition, impurities can be responsible for the formation of surface compounds that are easily removed from the growing diamond crystal and thereby removing carbon atoms. Similar to the assumption made above, if  $\{111\}$  crystal facets have the highest surface energy they are the most likely planes to bond with Si. If the formed surface compounds are etched easily, this will lead to the formation of plates. A possible route for the removal of surface carbon atoms is similar to the beta-scission reaction, i.e. when a methyl radical first binds to the diamond lattice followed by the addition of a  $\text{SiH}_3$  radical. The abstraction of a hydrogen atom can lead to a reaction similar to the beta-scission reaction and a methylenesilane can split off. Once  $\text{SiH}_3$  is covalently bonded to a singly bonded carbon atom at a lattice site, an atomic hydrogen abstracts a hydrogen to form a radical at Si and via a beta-scission reaction a methylenesilane is released into the plasma and a radical is left at the surface. This mechanism would lead to enhanced etching of  $\{111\}$  facets, which can account for the formation of diamond plates.

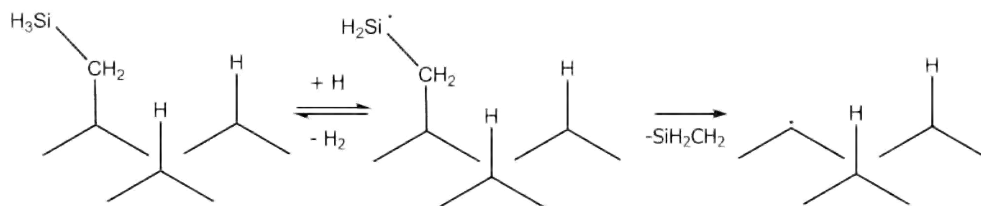


**Figure 7.10:** Adapted beta-scission reaction upon addition of a  $\text{SiH}_3$  radical. Based on the model proposed by Butler *et al.*<sup>[144]</sup>

## 7.3 Conclusion

We report the co-deposition of diamond plates with a high aspect ratio together with octahedral diamond grains with LA MW PE CVD technology at low temperatures (320 - 410 °C). The diamond plate structure has only been reported a few times up to now, and the initiation of the growth mechanism still remained unclear. Based on the current results, it is proposed that either LA MW PE CVD technology mimics the conditions, i.e. active species and electron temperature, obtained at high temperatures in common CVD systems, or the formation of plates is attributed to the presence of foreign atoms. They can catalyse the formation of fullerenes that encapsulates foreign atom clusters, which at a certain point turns into diamond since diamond is more stable at the nanoscale, and because of the similarities in lattice parameters between graphene layers (of the fullerene) and hexagonal diamond, some hexagonal diamond nuclei are formed next to the cubic nuclei. Once a faulted, hexagonal diamond nucleus is formed it will continue to exist because of its regenerative nature. The growth of the eventual plate is an interplay between fast  $\{100\}$  growth (compared to slow  $\{111\}$ ) and enhanced twin growth (at hexagonal diamond nuclei). Since both Al and Si are present, and they can both catalyse the formation of fullerenes,<sup>[210]</sup> both materials can induce plate growth formation. Alternative suggestions are that foreign atoms preferentially bond to  $\{111\}$  planes because of better lattice matching and a higher surface energy of this facet, thereby leading to either enhanced etching of  $\{111\}$  facets or a growth blocking layer at  $\{111\}$  planes, which both lead to the formation of diamond plates.



# Conclusion and future perspectives

In order to make sensitive pressure sensing membranes, it is necessary to identify all parameters that have an influence on the final pressure sensitivity of the membrane. To this end, nanocrystalline diamond membranes were fabricated on glass and their pressure sensing properties were related to their internal stress levels, which was described in chapter 5. The piezoresistive behaviour of boron-doped and hydrogen-terminated surfaces conductive nanocrystalline diamond films was shown and pressure sensors were fabricated. For hydrogen-terminated surface conductive diamond membranes, a large piezoresistive effect is also observed with inflation and deflation, as described in chapter 5. The piezoresistive hydrogenated amorphous carbon of the grain boundaries is responsible for a large instantaneous jump. Charge trapping at grain boundaries leads to a small time-dependent piezoresistive effect. More evidence that the band gap of SCD:H narrows when it is strained needs to be provided in future work. In order to confirm the proposed model and to further clarify the transport mechanisms and the origin of the piezoresistive effect in NCD:H, piezoresistive effect measurements on SCD:H should to be performed to separate grain and grain boundary contributions. At this point, processing single crystal diamond to fabricate a device to measure the piezoresistive effect in SCD:H is rather complex although not impossible in the near future.<sup>[229,230]</sup>

Then, we presented a guideline for the optimisation of B-doped nanocrystalline membranes, and other materials based on the same design. The sensitivity of pressure sensing membranes is found to increase with decreasing doping level and increasing membrane size. In addition, there is an influence of the underlying substrate, i.e. B:NCD membranes contain a certain stress level after deposition because of the mismatch in thermal expansion coefficients between the diamond layer and the substrate. For B:NCD membranes on glass, compressive stress is induced during growth leading to wrinkle formation induced by out-of-plane deformations which release stress upon removal of the substrate. The sensitivity of the corresponding pressure sensors can be related to the amount of wrinkles, i.e. samples that are more wrinkled, because they were more compressed initially, are less sensitive to the pressure difference, as they need to dewrinkle first before they can start to inflate. The sensitivity is found to be 55% higher for the membranes on CE2000 glass compared to membranes on S-AF45 glass. This is because the films on CE2000 glass are less compressed, due to a smaller difference in thermal expansion coefficient between this type of glass and the B:NCD film. This means that the sensitivity depends on the choice of the substrate material: a substrate with a thermal expansion coefficient similar to, and ideally slightly smaller than, diamond would ensure flat membranes. For future work, other glass substrates with lower thermal expansion coefficients should be tested. For optimal sensitivity, which means a match in thermal expansion coefficients between substrate and the sensing layer, and to eliminate the effect of the grain boundaries on transport measurements, efforts could be made to develop single crystal diamond membranes. In addition, it remains important to focus on the adhesion and stability during the development of these pressure sensors to ensure that delamination is not an issue. Moreover, more insight in the fatigue and fracture toughness needs to be gained to estimate how much strain they can handle and to develop stable and robust sensors.

Theoretically, diamond deposition at lower temperatures leads to lower compressive stress. Therefore, the second part of this thesis focused on low temperature growth of nanocrystalline diamond layers with novel linear antenna technology. In chapter 6, it was shown that the diamond morphology depends highly on the deposition parameters, which are pressure, gas composition, sample-to-antenna distance, power and temperature. The optimal conditions are reached at low pressures, low-to-medium distance between the sample and the antennas, low CH<sub>4</sub> and high CO<sub>2</sub> concentration, medium-to-high power and without the use of the substrate heater.

In addition the use of pulsed microwaves offers the potential to grow nanocrystalline diamond layers with a lower energy input and lower heating of the substrate, thereby reducing the thermal load onto sensitive substrate materials. Although one very high quality layer was obtained, conditions for pinhole free layers have not yet been met. Membrane fabrication based on diamond films deposited in the linear antenna system was not very successful yet, presumably due to the particular morphology obtained. Therefore, layers deposited at lower temperatures to minimise the difference in expansion between different materials and thus thermal stress in the film, should be grown in conditions that don't give rise to plate formation, which seems to be at very close distance between the sample and the antennas to ensure fully closed nanocrystalline diamond layers.

B-doped membranes grown in collaboration with A. Taylor and A. Kromka with low temperature linear antenna technology, in conditions that don't give rise to plate formation, are expected to show high sensitivities. In addition, efforts could be made to grow crystalline layers at temperatures below 300 °C, in order to minimise thermal stress.

In the final chapter the co-deposition of diamond plates with a high aspect ratio together with octahedral diamond grains was reported. The plate diamond morphology is quite rare, and has only been reported a couple of times. In contrast to previous reports claiming the need of high temper-



atures ( $T > 1000$  °C), in this work low temperatures ( $320$  °C  $\leq T \leq 410$  °C) were sufficient to deposit diamond platelet structures. Cross-sectional HRTEM studies show that these plates are terminated by large  $\{111\}$  surface facets. Raman and electron energy loss spectroscopy both confirm that diamond quality is very high. Up to now, literature reports have focused on the characterisation of these plates and multiple growth models have been proposed. These models start from an initial diamond structure that contains many stacking faults, i.e. layers of hexagonal diamond, and account for the development of plates by preferential growth sites or by the relative growth rates of crystal facets. Nevertheless, in none of the previous reports has an explicit reason for the presence of these stacking faults been given. Here a model was proposed that accounts for the initial development of these plates full of stacking faults and the growth of this morphology at low temperatures. This model is based on the presence of foreign atoms, which can enhance the growth of diamond plates in various ways; the impurities induce the formation of stacking faults, they block a certain crystal facet from further growth, or they ensure enhanced etching of a crystal facet. A combined effect of the first option with one of the latter two is of course possible as well.

Optical emission spectroscopy revealed some of the plasma characteristics that might be responsible for the growth mechanisms behind this particular morphology. To gain more insight into the plasma chemistry and the active species of interest, a mass spectrometer could be connected to the exhaust. In addition, infrared laser absorption spectroscopy could estimate the  $\text{CH}_3$  radical concentration, which is interesting because optical emission spectroscopy is insensitive to the main reactive species responsible for diamond growth. In addition, knowledge of the plasma electron density and electron temperature could confirm the conclusions drawn above, therefore Langmuir probe measurements would be an interesting addition.

# Bibliography

- [1] "Schematic view of the hybrid orbital model. <http://virtuallaboratory.colorado.edu/CLUE-Chemistry/chapters/chapter3txt-3.html>. [Accessed on: 2016-08-01]."
- [2] "Diamond. <http://www.chm.bris.ac.uk/webprojects2003/shanley/carbonallotropes/diamond.htm>. [Accessed on: 2016-08-01]."
- [3] "Lonsdaleite. <http://thefutureofthings.com/3953-harder-than-diamond/> [Accessed on 2016-08-01]."
- [4] "Hot Electrons in Carbon -Graphite behaves like a semiconductor. [https://www.mbi-berlin.de/en/research/highlights/highlight\\_graphite.html](https://www.mbi-berlin.de/en/research/highlights/highlight_graphite.html). [Accessed on: 2016-08-01]."
- [5] B. Van der Bruggen, "The Separation Power of Nanotubes in Membranes: A Review," *ISRN Nanotechnol.*, vol. 2012, pp. 1–17, 2012.
- [6] "Buckyball. <http://www.technovelgy.com/ct/Science-Fiction-News.asp?NewsNum=1388>. [Accessed on: 2016-08-01]."
- [7] "Amorphous Carbon. [https://commons.wikimedia.org/wiki/File:Amorphous\\_Carbon.png](https://commons.wikimedia.org/wiki/File:Amorphous_Carbon.png). [Accessed on: 2016-08-01]."
- [8] Mc Diamantfibel, "The CVD diamond booklet. [http://www.diamond-materials.com/downloads/cvd\\_diamond\\_booklet.pdf](http://www.diamond-materials.com/downloads/cvd_diamond_booklet.pdf). [Accessed on: 2016-08-01]."

## BIBLIOGRAPHY

---

- [9] R. Narayan, ed., *Diamond-based materials for biomedical applications*. Woodhead Publishing, 1 ed., 2013.
- [10] P. W. May, "Diamond thin films: a 21st-century material," *Philos. Trans. R. Soc. A Math. Phys. Eng. Sci.*, vol. 358, no. 1766, pp. 473–495, 2000.
- [11] P. Bridgman, "Synthetic diamonds," *Sci. Am.*, vol. 193, no. 5, pp. 42–46, 1955.
- [12] F. Bundy, H. Hall, H. Strong, and R. Wentorf, "Man-Made Diamonds," *Nature*, vol. 176, pp. 51–55, 1955.
- [13] F. P. Bundy, "The P,T phase and reaction diagram for elemental carbon, 1979," *J. Geophys. Res.*, vol. 85, no. B12, p. 6930, 1980.
- [14] M. Akaishi, H. Kanda, and S. Yamaoka, "High Pressure Synthesis of Diamond in the Systems of Graphite-Sulfate and Graphite-Hydroxide," *Jpn. J. Appl. Phys.*, vol. 29, no. Part 2, No. 7, pp. L1172–L1174, 1990.
- [15] S. Hong, M. Akaishi, and S. Yamaoka, "Nucleation of diamond in the system of carbon and water under very high pressure and temperature," *J. Cryst. Growth*, vol. 200, no. 1, pp. 326–328, 1999.
- [16] Y. N. Pal'yanov, A. G. Sokol, Y. M. Borzdov, A. F. Khokhryakov, and N. V. Sobolev, "Diamond formation from mantle carbonate fluids," *Nature*, vol. 400, no. 6743, pp. 417–418, 1999.
- [17] M. Akaishi and S. Yamaoka, "Crystallization of diamond from C-O-H fluids under high-pressure and high-temperature conditions," *J. Cryst. Growth*, vol. 209, no. 4, pp. 999–1003, 2000.
- [18] M. Arima, Y. Kozai, and M. Akaishi, "Diamond nucleation and growth by reduction of carbonate melts under high-pressure and high-temperature conditions," *Geology*, vol. 30, no. 8, p. 691, 2002.

- [19] Y. N. Pal'yanov, A. Sokol, A. Khokhryakov, G. Pal'yanova, Y. M. Borzdov, and N. V. Sobolev, "Diamond and Graphite Crystallization in C-O-H Fluid at P-T Parameters of the Natural Diamond Formation," *Dokl. Akad. Nauk SSSR*, vol. 375, no. 9, pp. 1395–1398, 2000.
- [20] A. G. Sokol, A. A. Tomilenko, Y. N. Pal'yanov, Y. M. Borzdov, G. A. Pal'yanova, and A. F. Khokhryakov, "Fluid regime of diamond crystallisation in carbonate-carbon systems," *Eur. J. Mineral.*, vol. 12, no. 2, 2000.
- [21] M. Shaji Kumar, M. Akaishi, and S. Yamaoka, "Effect of fluid concentration on the formation of diamond in the CO<sub>2</sub>-H<sub>2</sub>O-graphite system under HPHT conditions," *J. Cryst. Growth*, vol. 222, no. 1, pp. 9–13, 2001.
- [22] A. Sokol, Y. Pal'yanov, G. Pal'yanova, A. Khokhryakov, and Y. Borzdov, "Diamond and graphite crystallization from C-O-H fluids under high pressure and high temperature conditions," *Diam. Relat. Mater.*, vol. 10, no. 12, pp. 2131–2136, 2001.
- [23] N. Pal'yanov, A. Sokol, M. Borzdov, and A. Khokhryakov, "Fluid-bearing alkaline carbonate melts as the medium for the formation of diamonds in the Earth's mantle: an experimental study," *Lithos*, vol. 60, no. 3, pp. 145–159, 2002.
- [24] L. Dobrzhinetskaya, A. Renfro, and H. Green, "Synthesis of skeletal diamonds: Implications for microdiamond formation in orogenic belts," *Geology*, vol. 32, no. 10, p. 869, 2004.
- [25] L. Dobrzhinetskaya and H. W. Green, "Experimental studies of mineralogical assemblages of metasedimentary rocks at Earth's mantle transition zone conditions," *J. Metamorph. Geol.*, vol. 25, no. 2, pp. 83–96, 2007.
- [26] L. F. Dobrzhinetskaya, "Microdiamonds - Frontier of ultrahigh-

- pressure metamorphism: A review," *Gondwana Res.*, vol. 21, no. 1, pp. 207–223, 2012.
- [27] W. Eversole, "Synthesis of diamond," *US Pat. no 3030187*, 1958.
- [28] B. Derjaguin, D. Fedoseev, V. Lukyanovich, B. Spitzin, V. Ryabov, and A. Lavrentyev, "Filamentary diamond crystals," *J. Cryst. Growth*, vol. 2, no. 6, pp. 380–384, 1968.
- [29] J. C. Angus, "Growth of Diamond Seed Crystals by Vapor Deposition," *J. Appl. Phys.*, vol. 39, no. 6, p. 2915, 1968.
- [30] B. Derjaguin, B. Spitsyn, L. Builov, A. Klochkov, A. Gorodetskii, and A. Smol'yanov, "Synthesis of diamond crystals on non-diamond substrates," *Sov. Phys.*, vol. 21, pp. 676–679, 1976.
- [31] S. Matsumoto, Y. Sato, M. Kamo, and N. Setaka, "Vapor Deposition of Diamond Particles from Methane," *Jpn. J. Appl. Phys.*, vol. 21, no. Part 2, No. 4, pp. L183–L185, 1982.
- [32] S. Matsumoto, Y. Sato, M. Tsutsumi, and N. Setaka, "Growth of diamond particles from methane-hydrogen gas," *J. Mater. Sci.*, vol. 17, no. 11, pp. 3106–3112, 1982.
- [33] M. Kamo, Y. Sato, S. Matsumoto, and N. Setaka, "Diamond synthesis from gas phase in microwave plasma," *J. Cryst. Growth*, vol. 62, no. 3, pp. 642–644, 1983.
- [34] Y. Saito, S. Matsuda, and S. Nogita, "Synthesis of diamond by decomposition of methane in microwave plasma," *J. Mater. Sci. Lett.*, vol. 5, no. 5, pp. 565–568, 1986.
- [35] "Hope Diamond - A Blue Legend. <http://www.naturallycolored.com/famous-diamonds/hope-diamond>. [Accessed on: 2016-08-01]."
- [36] M. Schreck, "Heteroepitaxial Growth," in *CVD Diam. Electron. Devices Sensors*, pp. 125–161, Chichester, UK: John Wiley & Sons, Ltd, 2009.

- [37] O. Williams, M. Daenen, J. D'Haen, K. Haenen, J. Maes, V. Moshchalkov, M. Nesládek, and D. Gruen, "Comparison of the growth and properties of ultrananocrystalline diamond and nanocrystalline diamond," *Diam. Relat. Mater.*, vol. 15, no. 4-8, pp. 654–658, 2006.
- [38] O. Williams, "Nanocrystalline diamond," *Diam. Relat. Mater.*, vol. 20, no. 5-6, pp. 621–640, 2011.
- [39] O. A. Shenderova and D. M. Gruen, *Ultrananocrystalline diamond : synthesis, properties, and applications*. William Andrew Pub, 2006.
- [40] S. Ri, K. Tashiro, S. Tanaka, T. Fujisawa, H. Kimura, T. Kurosu, and M. Iida, "Hall Effect Measurements of Surface Conductive Layer on Undoped Diamond Films in NO<sub>2</sub> and NH<sub>3</sub> Atmospheres," *Jpn. J. Appl. Phys.*, vol. 38, no. Part 1, No. 6A, pp. 3492–3496, 1999.
- [41] F. Maier, M. Riedel, B. Mantel, J. Ristein, and L. Ley, "Origin of Surface Conductivity in Diamond," *Phys. Rev. Lett.*, vol. 85, no. 16, pp. 3472–3475, 2000.
- [42] S. Turner, Y.-G. Lu, S. D. Janssens, F. Da Pieve, D. Lamoen, J. Verbeeck, K. Haenen, P. Wagner, and G. Van Tendeloo, "Local boron environment in B-doped nanocrystalline diamond films," *Nanoscale*, vol. 4, no. 19, pp. 5960–4, 2012.
- [43] J.-P. Lagrange, A. Deneuve, and E. Gheeraert, "Activation energy in low compensated homoepitaxial boron-doped diamond films," *Diam. Relat. Mater.*, vol. 7, no. 9, pp. 1390–1393, 1998.
- [44] B. Spitsyn, L. Bouilov, and B. Derjaguin, "Vapor growth of diamond on diamond and other surfaces," *J. Cryst. Growth*, vol. 52, pp. 219–226, 1981.
- [45] R. Samlenski, C. Haug, R. Brenn, C. Wild, R. Locher, and P. Koidl, "Characterisation and lattice location of nitrogen and boron in ho-

- moepitaxial CVD diamond," *Diam. Relat. Mater.*, vol. 5, no. 9, pp. 947–951, 1996.
- [46] R. Locher, J. Wagner, F. Fuchs, M. Maier, P. Gonon, and P. Koidl, "Optical and electrical characterization of boron-doped diamond films," *Diam. Relat. Mater.*, vol. 4, no. 5-6, pp. 678–683, 1995.
- [47] E. Bustarret, P. Achatz, B. Sacépé, C. Chapelier, C. Marcenat, L. Ortéga, and T. Klein, "Metal-to-insulator transition and superconductivity in boron-doped diamond," *Philos. Trans. A. Math. Phys. Eng. Sci.*, vol. 366, no. 1863, pp. 267–79, 2008.
- [48] E. A. Ekimov, V. A. Sidorov, E. D. Bauer, N. N. Mel'nik, N. J. Curro, J. D. Thompson, and S. M. Stishov, "Superconductivity in diamond," *Nature*, vol. 428, no. 6982, pp. 542–545, 2004.
- [49] A. S. Barnard and M. Sternberg, "Substitutional Boron in Nanodiamond, Bucky-Diamond, and Nanocrystalline Diamond Grain Boundaries," *J. Phys. Chem. B*, vol. 110, no. 39, pp. 19307–19314, 2006.
- [50] G. D. Fuchs, G. Burkard, P. V. Klimov, and D. D. Awschalom, "A quantum memory intrinsic to single nitrogen-vacancy centres in diamond," *Nat. Phys.*, vol. 7, no. 10, pp. 789–793, 2011.
- [51] S. Kajihara, A. Antonelli, J. Bernholc, and R. Car, "Nitrogen and potential n-type dopants in diamond," *Phys. Rev. Lett.*, vol. 66, no. 15, pp. 2010–2013, 1991.
- [52] E. B. Lombardi, A. Mainwood, and K. Osuch, "Interaction of hydrogen with boron, phosphorus, and sulfur in diamond," *Phys. Rev. B*, vol. 70, no. 20, p. 205201, 2004.
- [53] S. Koizumi, M. Kamo, Y. Sato, H. Ozaki, and T. Inuzuka, "Growth and characterization of phosphorous doped {111} homoepitaxial diamond thin films," *Appl. Phys. Lett.*, vol. 71, no. 8, p. 1065, 1997.

- [54] H. Kato, W. Futako, S. Yamasaki, and H. Okushi, "Homoepitaxial growth and characterization of phosphorus-doped diamond using tertiarybutylphosphine as a doping source," *Diam. Relat. Mater.*, vol. 13, no. 11, pp. 2117–2120, 2004.
- [55] E. Gheeraert, N. Casanova, A. Tajani, A. Deneuve, E. Bustarret, J. Garrido, C. Nebel, and M. Stutzmann, "n-Type doping of diamond by sulfur and phosphorus," *Diam. Relat. Mater.*, vol. 11, no. 3, pp. 289–295, 2002.
- [56] M. Nesládek, "Conventional n-type doping in diamond: state of the art and recent progress," *Semicond. Sci. Technol.*, vol. 20, no. 2, pp. R19–R27, 2005.
- [57] T. Kociniewski, J. Barjon, M.-A. Pinault, F. Jomard, A. Lusson, D. Ballutaud, O. Gorochoy, J. M. Laroche, E. Rzepka, J. Chevallier, and C. Saguy, "n-type CVD diamond doped with phosphorus using the MOCVD technology for dopant incorporation," *Phys. status solidi*, vol. 203, no. 12, pp. 3136–3141, 2006.
- [58] H. Kato, S. Yamasaki, and H. Okushi, "n-type doping of (001)-oriented single-crystalline diamond by phosphorus," *Appl. Phys. Lett.*, vol. 86, no. 22, p. 222111, 2005.
- [59] H. Kato, S. Yamasaki, and H. Okushi, "n-type conductivity of phosphorus-doped homoepitaxial single crystal diamond on (001) substrate," *Diam. Relat. Mater.*, vol. 14, no. 11-12, pp. 2007–2010, 2005.
- [60] H. Kato, T. Makino, S. Yamasaki, and H. Okushi, "n-type diamond growth by phosphorus doping on (001)-oriented surface," *J. Phys. D. Appl. Phys.*, vol. 40, no. 20, pp. 6189–6200, 2007.
- [61] S. D. Janssens, P. Pobedinskas, J. Vacik, V. Petráková, B. Ruttens, J. D'Haen, M. Nesládek, K. Haenen, and P. Wagner, "Separation



- of intra- and intergranular magnetotransport properties in nanocrystalline diamond films on the metallic side of the metal-insulator transition," *New J. Phys.*, vol. 13, no. 8, p. 083008, 2011.
- [62] F. A. Koeck, R. J. Nemanich, A. Lazea, and K. Haenen, "Thermionic electron emission from low work-function phosphorus doped diamond films," *Diam. Relat. Mater.*, vol. 18, no. 5-8, pp. 789–791, 2009.
- [63] M. Nesládek, K. Haenen, J. D'Haen, S. Koizumi, and H. Kanda, "N-type P-doped polycrystalline diamond," *Phys. Status Solidi*, vol. 199, no. 1, pp. 77–81, 2003.
- [64] S. N. Schauer, J. R. Flemish, R. Wittstruck, M. I. Landstrass, and M. a. Plano, "Phosphorus incorporation in plasma deposited diamond films," *Appl. Phys. Lett.*, vol. 64, no. 9, p. 1094, 1994.
- [65] S. Bohr, R. Haubner, and B. Lux, "Influence of phosphorus addition on diamond CVD," *Diam. Relat. Mater.*, vol. 4, pp. 133–144, 1995.
- [66] S. Ghodbane, F. Omnès, E. Bustarret, C. Tavares, and F. Jomard, "N-Type Phosphorus-Doped Polycrystalline Diamond on Silicon Substrates," *Diam. Relat. Mater.*, vol. 17, no. 7-10, pp. 1324–1329, 2008.
- [67] W. Janssen, S. Turner, G. Sakr, F. Jomard, J. Barjon, G. Degutis, Y.-G. Lu, J. D'Haen, A. Hardy, M. V. Bael, J. Verbeeck, G. V. Tendeloo, and K. Haenen, "Substitutional phosphorus incorporation in nanocrystalline CVD diamond thin films," *Phys. status solidi - Rapid Res. Lett.*, vol. 8, no. 8, pp. 705–709, 2014.
- [68] R. Ohtani, T. Yamamoto, S. D. Janssens, S. Yamasaki, and S. Koizumi, "Large improvement of phosphorus incorporation efficiency in n-type chemical vapor deposition of diamond," *Appl. Phys. Lett.*, vol. 105, no. 23, p. 232106, 2014.

- [69] Z. Vlčková Živcová, O. Frank, S. Drijkoningen, K. Haenen, V. Mortet, and L. Kavan, "n-Type phosphorus-doped nanocrystalline diamond: electrochemical and in situ Raman spectroelectrochemical study," *RSC Adv.*, vol. 6, no. 56, pp. 51387–51393, 2016.
- [70] M. Z. Othman, P. W. May, N. A. Fox, and P. J. Heard, "Incorporation of lithium and nitrogen into CVD diamond thin films," *Diam. Relat. Mater.*, vol. 44, pp. 1–7, 2014.
- [71] R. Kalish, A. Reznik, C. Uzan-Saguy, and C. Cytermann, "Is sulfur a donor in diamond?," *Appl. Phys. Lett.*, vol. 76, no. 6, p. 757, 2000.
- [72] G. Frangieh, M.-A. Pinault, J. Barjon, F. Jomard, and J. Chevallier, "Incorporation of arsenic in diamond grown by chemical vapor deposition," *Phys. status solidi*, vol. 205, no. 9, pp. 2207–2210, 2008.
- [73] J. Barjon, F. Jomard, and S. Morata, "Arsenic-bound excitons in diamond," *Phys. Rev. B*, vol. 89, no. 4, p. 045201, 2014.
- [74] J. te Nijenhuis, G. Cao, P. Smits, W. van Enkevort, L. Giling, P. Alkemade, M. Nesládek, and Z. Remeš, "Incorporation of lithium in single crystal diamond: diffusion profiles and optical and electrical properties," *Diam. Relat. Mater.*, vol. 6, no. 11, pp. 1726–1732, 1997.
- [75] H. Liu and D. S. Dandy, "Studies on nucleation process in diamond CVD: an overview of recent developments," *Diam. Relat. Mater.*, vol. 4, no. 10, pp. 1173–1188, 1995.
- [76] W. Kern and D. A. Puotinen, "Cleaning solutions based on hydrogen peroxide for use in silicon semiconductor technology," *RCA Rev.*, vol. 31, no. 2, pp. 187–206, 1970.
- [77] O. A. Williams, O. Douhéret, M. Daenen, K. Haenen, E. Ósawa, and M. Takahashi, "Enhanced diamond nucleation on monodispersed nanocrystalline diamond," *Chem. Phys. Lett.*, vol. 445, no. 4-6, pp. 255–258, 2007.

- [78] M. Daenen, O. A. Williams, J. D'Haen, K. Haenen, and M. Nesládek, "Seeding, growth and characterization of nanocrystalline diamond films on various substrates," *Phys. Status Solidi*, vol. 203, no. 12, pp. 3005–3010, 2006.
- [79] S. Yugo, T. Kanai, T. Kimura, and T. Muto, "Generation of diamond nuclei by electric field in plasma chemical vapor deposition," *Appl. Phys. Lett.*, vol. 58, no. 10, p. 1036, 1991.
- [80] J. Robertson, "Mechanism of bias-enhanced nucleation and heteroepitaxy of diamond on Si," *Diam. Relat. Mater.*, vol. 4, no. 5-6, pp. 549–552, 1995.
- [81] Y. Lifshitz, T. Köhler, T. Frauenheim, I. Guzman, A. Hoffman, R. Q. Zhang, X. T. Zhou, and S. T. Lee, "The mechanism of diamond nucleation from energetic species," *Science*, vol. 297, no. 5586, pp. 1531–3, 2002.
- [82] J. Gerber, S. Sattel, H. Ehrhardt, J. Robertson, P. Wurzinger, and P. Pongratz, "Investigation of bias enhanced nucleation of diamond on silicon," *J. Appl. Phys.*, vol. 79, no. 8, p. 4388, 1996.
- [83] J. E. Butler, R. L. Woodin, L. M. Brown, and P. Fallon, "Thin Film Diamond Growth Mechanisms [and Comment]," *Philos. Trans. R. Soc. A Math. Phys. Eng. Sci.*, vol. 342, no. 1664, pp. 209–224, 1993.
- [84] J. E. Butler, Y. A. Mankelevich, A. Cheesman, J. Ma, and M. N. R. Ashfold, "Understanding the chemical vapor deposition of diamond: recent progress," *J. Phys. Condens. Matter*, vol. 21, no. 36, p. 364201, 2009.
- [85] J. Stiegler, T. Lang, M. Nygård-Ferguson, Y. von Kaenel, and E. Blank, "Low temperature limits of diamond film growth by microwave plasma-assisted CVD," *Diam. Relat. Mater.*, vol. 5, no. 3-5, pp. 226–230, 1996.

- [86] B. Sun, X. Zhang, Q. Zhang, and Z. Lin, "Effect of atomic hydrogen and oxygen on diamond growth," *J. Appl. Phys.*, vol. 73, no. 9, p. 4614, 1993.
- [87] P. K. Bachmann, D. Leers, and H. Lydtin, "Towards a general concept of diamond chemical vapour deposition," *Diam. Relat. Mater.*, vol. 1, no. 1, pp. 1–12, 1991.
- [88] "Datasheet Quartz Tubes LA MW PE CVD system - QSIL-ilmasil-PN\_e. [http://www.qsil.com/files/online/Material/QSILilmasilPN\\_e.pdf](http://www.qsil.com/files/online/Material/QSILilmasilPN_e.pdf). [Accessed on: 2016-05-30]," 2015.
- [89] M. Liehr and M. Dieguez-Campo, "Microwave PECVD for large area coating," *Surf. Coat. Technol.*, vol. 200, pp. 21–25, 2005.
- [90] T. Izak, A. Sveshnikov, P. Demo, and A. Kromka, "Enhanced spontaneous nucleation of diamond nuclei in hot and cold microwave plasma systems," *Phys. Status Solidi*, vol. 250, no. 12, pp. 2753–2758, 2013.
- [91] K. Tsugawa, M. Ishihara, J. Kim, M. Hasegawa, and Y. Koga, "Large-Area and Low-Temperature Nanodiamond Coating by Microwave Plasma Chemical Vapor Deposition," *New Diam. Front. Carbon Technol.*, vol. 16, no. 6, pp. 337–346, 2007.
- [92] K. Tsugawa, M. Ishihara, J. Kim, Y. Koga, and M. Hasegawa, "Nanocrystalline diamond film growth on plastic substrates at temperatures below 100 °C from low-temperature plasma," *Phys. Rev. B*, vol. 82, no. 12, p. 125460, 2010.
- [93] K. Tsugawa, S. Kawaki, M. Ishihara, J. Kim, Y. Koga, H. Sakakita, H. Koguchi, and M. Hasegawa, "Nanocrystalline diamond growth in a surface-wave plasma," *Diam. Relat. Mater.*, vol. 20, no. 5-6, pp. 833–838, 2011.

- [94] F. M. Cerio and W. A. Weimer, "Electrostatic probe measurements for microwave plasma-assisted chemical vapor deposition of diamond," *Appl. Phys. Lett.*, vol. 59, no. 26, p. 3387, 1991.
- [95] T. Sharda, D. Misra, D. Avasthi, and G. Mehta, "Dissociation kinetics of molecular hydrogen in a microwave plasma and its influence on the hydrogen content in diamond films," *Solid State Commun.*, vol. 98, no. 10, pp. 879–883, 1996.
- [96] Š. Potocký, M. Čada, O. Babchenko, T. Ižák, M. Davydova, and A. Kromka, "Perspectives of linear antenna microwave system for growth of various carbon nano-forms and its plasma study," *Phys. Status Solidi*, vol. 250, no. 12, pp. 2723–2726, 2013.
- [97] O. Babchenko, Š. Potocký, T. Ižák, K. Hruška, Z. Bryknar, and A. Kromka, "Influence of surface wave plasma deposition conditions on diamond growth regime," *Surf. Coatings Technol.*, vol. 271, pp. 74–79, 2015.
- [98] A. Kromka, O. Babchenko, T. Izak, K. Hruska, and B. Rezek, "Linear antenna microwave plasma CVD deposition of diamond films over large areas," *Vacuum*, vol. 86, no. 6, pp. 776–779, 2012.
- [99] Š. Potocký, O. Babchenko, M. Davydova, T. Izak, M. Čada, and A. Kromka, "Growth of carbon allotropes and plasma characterization in linear antenna microwave plasma CVD system," *Jpn. J. Appl. Phys.*, vol. 53, no. 5S1, p. 05FP04, 2014.
- [100] J. Vlček, F. Fendrych, A. Taylor, I. Kratochvílová, L. Fekete, M. Nesládek, and M. Liehr, "Novel Concepts for Low-pressure, Low-temperature Nanodiamond Growth Using MW-linear Antenna Plasma Sources," *Mater. Res. Soc. Symp. Proc.*, vol. 1203, 2010.
- [101] Š. Potocký, O. Babchenko, K. Hruška, and A. Kromka, "Linear antenna microwave plasma CVD diamond deposition at the edge of

- no-growth region of C-H-O ternary diagram," *Phys. status solidi*, vol. 249, no. 12, pp. 2612–2615, 2012.
- [102] T. Izak, O. Babchenko, M. Varga, S. Potocky, and A. Kromka, "Low temperature diamond growth by linear antenna plasma CVD over large area," *Phys. status solidi*, vol. 249, no. 12, pp. 2600–2603, 2012.
- [103] S. Ashida, "Spatially averaged (global) model of time modulated high density argon plasmas," *J. Vac. Sci. Technol. A Vacuum, Surfaces, Film.*, vol. 13, no. 5, p. 2498, 1995.
- [104] J. Vlcek, F. Fendrych, A. Taylor, M. Novotny, and M. Liehr, "Pulsed plasmas study of linear antennas microwave CVD system for nanocrystalline diamond film growth," *J. Mater. Res.*, vol. 27, no. 05, pp. 863–867, 2011.
- [105] A. Taylor, F. Fendrych, L. Fekete, J. Vlček, V. Āžezáčová, V. Petrák, J. Krucký, M. Nesládek, and M. Liehr, "Novel high frequency pulsed MW-linear antenna plasma-chemistry: Routes towards large area, low pressure nanodiamond growth," *Diam. Relat. Mater.*, vol. 20, no. 4, pp. 613–615, 2011.
- [106] J. Laimer and S. Matsumoto, "Atomic hydrogen concentrations in pulsed microwave discharges used for diamond synthesis," *Plasma Chem. Plasma Process.*, vol. 14, no. 2, pp. 117–130, 1994.
- [107] Z. Ring, T. D. Mantei, S. Tlali, and H. E. Jackson, "Low-temperature diamond growth in a pulsed microwave plasma," *J. Vac. Sci. Technol. A Vacuum, Surfaces, Film.*, vol. 13, no. 3, p. 1617, 1995.
- [108] A. Hatta, H. Suzuki, K. Kadota, H. Makita, T. Ito, and A. Hiraki, "Fabrication of diamond films at low temperature by pulse-modulated magneto-active microwave plasma CVD," *Plasma Sources Sci. Technol.*, vol. 5, no. 2, pp. 235–240, 1996.

- [109] H. Chatei, J. Bougdira, M. Remy, P. Alnot, C. Bruch, and J. K. Krüger, "Combined effect of nitrogen and pulsed microwave plasma on diamond growth," *Diam. Relat. Mater.*, vol. 6, no. 2, pp. 505–510, 1997.
- [110] K. Hassouni, X. Duten, A. Rousseau, and A. Gicquel, "Investigation of chemical kinetics and energy transfer in a pulsed microwave H<sub>2</sub>/CH<sub>4</sub> plasma," *Plasma Sources Sci. Technol.*, vol. 10, p. 61, 2001.
- [111] A. Gicquel, K. Hassouni, and G. Lombardi, "New driving Parameters for Diamond Deposition Reactors : Pulsed Mode versus Continuous Mode," *Mater. Res.*, vol. 6, pp. 25–37, 2002.
- [112] F. Fendrych, A. Taylor, L. Peksa, I. Kratochvilova, J. Vlcek, V. Rezacova, V. Petrak, Z. Kluiber, L. Fekete, M. Liehr, and M. Nesládek, "Growth and characterization of nanodiamond layers prepared using the plasma-enhanced linear antennas microwave CVD system," *J. Phys. D. Appl. Phys.*, vol. 43, no. 37, p. 374018, 2010.
- [113] J. Mistrik, P. Janicek, A. Taylor, F. Fendrych, L. Fekete, A. Jager, and M. Nesladek, "Spectroscopic ellipsometry characterization of nanocrystalline diamond films prepared at various substrate temperatures and pulsed plasma frequencies using microwave plasma enhanced chemical vapor deposition apparatus with linear antenna delivery," *Thin Solid Films*, vol. 571, pp. 230–237, 2014.
- [114] H.-A. Mehedi, J. Achard, D. Rats, O. Brinza, A. Tallaire, V. Mille, F. Silva, C. Provent, and A. Gicquel, "Low temperature and large area deposition of nanocrystalline diamond films with distributed antenna array microwave-plasma reactor," *Diam. Relat. Mater.*, vol. 47, pp. 58–65, 2014.
- [115] L. A. J. Garvie, A. J. Craven, and R. Brydson, "Use of electron-energy loss near-edge fine structure in the study of minerals," *Am. Mineral.*, vol. 79, no. 5-6, 1994.

- [116] D. S. Knight and W. B. White, "Characterization of diamond films by Raman spectroscopy," *J. Mater. Res.*, vol. 4, no. 02, pp. 385–393, 1989.
- [117] F. Silva, A. Gicquel, A. Tardieu, P. Cledat, and T. Chauveau, "Control of an MPACVD reactor for polycrystalline textured diamond films synthesis: role of microwave power density," *Diam. Relat. Mater.*, vol. 5, no. 3, pp. 338–344, 1996.
- [118] S. Leeds, T. Davis, P. May, C. Pickard, and M. Ashfold, "Use of different excitation wavelengths for the analysis of CVD diamond by laser Raman spectroscopy," *Diam. Relat. Mater.*, vol. 7, no. 2-5, pp. 233–237, 1998.
- [119] S. R. Sails, D. J. Gardiner, M. Bowden, J. Savage, and D. Rodway, "Monitoring the quality of diamond films using Raman spectra excited at 514.5 nm and 633 nm," *Diam. Relat. Mater.*, vol. 5, no. 6-8, pp. 589–591, 1996.
- [120] A. C. Ferrari and J. Robertson, "Raman spectroscopy of amorphous, nanostructured, diamond-like carbon, and nanodiamond," *Philos. Trans. A. Math. Phys. Eng. Sci.*, vol. 362, no. 1824, pp. 2477–512, 2004.
- [121] G. Gouadec and P. Colomban, "Raman Spectroscopy of nanomaterials: How spectra relate to disorder, particle size and mechanical properties," *Prog. Cryst. Growth Charact. Mater.*, vol. 53, no. 1, pp. 1–56, 2007.
- [122] W. Wang, M. Polo, and G. Sanchez, "Internal stress and strain in heavily boron-doped diamond films grown by microwave plasma and hot filament chemical vapor deposition," *J. Appl. Phys.*, vol. 80, no. 3, 1996.
- [123] M. Bernard, A. Deneuve, and P. Muret, "Non-destructive determination of the boron concentration of heavily doped metallic diamond



## BIBLIOGRAPHY

---

- thin films from Raman spectroscopy," *Diam. Relat. Mater.*, vol. 13, no. 2, pp. 282–286, 2004.
- [124] G. G. Stoney, "The Tension of Metallic Films Deposited by Electrolysis," *Proc. R. Soc. A Math. Phys. Eng. Sci.*, vol. 82, no. 553, pp. 172–175, 1909.
- [125] C. A. Klein and G. F. Cardinale, "Young's modulus and Poisson's ratio of CVD diamond," *Diam. Relat. Mater.*, vol. 2, no. 5-7, pp. 918–923, 1993.
- [126] M. D. Drory, R. H. Dauskardt, A. Kant, and R. O. Ritchie, "Fracture of synthetic diamond," *J. Appl. Phys.*, vol. 78, no. 5, p. 3083, 1995.
- [127] H. Masuda, T. Yanagishita, K. Yasui, K. Nishio, I. Yagi, T. N. Rao, and A. Fujishima, "Synthesis of Well-Aligned Diamond Nanocylinders," *Adv. Mater.*, vol. 13, no. 4, pp. 247–249, 2001.
- [128] N. Shang, P. Papakonstantinou, P. Wang, A. Zakharov, U. Palnitkar, I.-N. Lin, M. Chu, and A. Stamboulis, "Self-Assembled Growth, Microstructure, and Field-Emission High-Performance of Ultrathin Diamond Nanorods," *ACS Nano*, vol. 3, no. 4, pp. 1032–1038, 2009.
- [129] J. C. Angus, M. Sunkara, S. R. Sahaida, and J. T. Glass, "Twinning and faceting in early stages of diamond growth by chemical vapor deposition," *J. Mater. Res.*, vol. 7, no. 11, pp. 3001–3009, 1992.
- [130] C.-A. Lu and L. Chang, "Synthesis of diamond hexagonal nanoplatelets by microwave plasma chemical vapor deposition," *Diam. Relat. Mater.*, vol. 13, no. 11-12, pp. 2056–2062, 2004.
- [131] C.-A. Lu and L. Chang, "Microstructural investigation of hexagonal-shaped diamond nanoplatelets grown by microwave plasma chemical vapor deposition," *Mater. Chem. Phys.*, vol. 92, no. 1, pp. 48–53, 2005.

- [132] H.-G. Chen and L. Chang, "Structural investigation of diamond nanoplatelets grown by microwave plasma-enhanced chemical vapor deposition," *J. Mater. Res.*, vol. 20, no. 03, pp. 703–711, 2005.
- [133] A. M. Alexeev, R. R. Ismagilov, E. E. Ashkinazi, A. S. Orekhov, S. A. Malykhin, and A. N. Obraztsov, "Diamond platelets produced by chemical vapor deposition," *Diam. Relat. Mater.*, vol. 65, pp. 13–16, 2016.
- [134] A. R. Lang, "A proposed structure for nitrogen impurity platelets in diamond," *Proc. Phys. Soc.*, vol. 84, no. 6, pp. 871–876, 1964.
- [135] C. Wild, R. Kohl, N. Herres, W. Müller-Sebert, and P. Koidl, "Oriented CVD diamond films: twin formation, structure and morphology," *Diam. Relat. Mater.*, vol. 3, no. 4-6, pp. 373–381, 1994.
- [136] D. R. Hamilton and R. G. Seidensticker, "Propagation Mechanism of Germanium Dendrites," *J. Appl. Phys.*, vol. 31, no. 7, p. 1165, 1960.
- [137] N.-b. Ming and I. Sunagawa, "Twin lamellae as possible self-perpetuating step sources," *J. Cryst. Growth*, vol. 87, no. 1, pp. 13–17, 1988.
- [138] A. I. Kirkland, D. A. Jefferson, D. G. Duff, P. P. Edwards, I. Gameston, B. F. G. Johnson, and D. J. Smith, "Structural Studies of Trigonal Lamellar Particles of Gold and Silver," *Proc. R. Soc. A Math. Phys. Eng. Sci.*, vol. 440, no. 1910, pp. 589–609, 1993.
- [139] G. Bögels, T. M. Pot, H. Meekes, P. Bennema, and D. Bollen, "Side-Face Structure and Growth Mechanism of Tabular Silver Bromide Crystals," *Acta Crystallogr. Sect. A Found. Crystallogr.*, vol. 53, no. 1, pp. 84–94, 1997.
- [140] H.-G. Chen and L. Chang, "Characterization of diamond nanoplatelets," *Diam. Relat. Mater.*, vol. 13, pp. 590–594, 2004.

- [141] H.-G. Chen, L. Chang, S.-Y. Cho, J.-K. Yan, and C.-A. Lu, "Growth of Diamond Nanoplatelets by CVD," *Chem. Vap. Depos.*, vol. 14, no. 7-8, pp. 247–255, 2008.
- [142] M. Sunkara, *Monte-Carlo Simulation of Diamond Nucleation and Growth*. PhD thesis, Case Western Reserve University, 1993.
- [143] E. Ringe, R. P. Van Duyne, and L. D. Marks, "Kinetic and Thermodynamic Modified Wulff Constructions for Twinned Nanoparticles," *J. Phys. Chem. C*, vol. 117, no. 31, pp. 15859–15870, 2013.
- [144] J. E. Butler and I. Oleynik, "A mechanism for crystal twinning in the growth of diamond by chemical vapour deposition," *Philos. Trans. A. Math. Phys. Eng. Sci.*, vol. 366, no. 1863, pp. 295–311; discussion 311, 2008.
- [145] K. Kummer, A. Fondacaro, F. Yakhou-Harris, V. Sessi, P. Pobedinskas, S. D. Janssens, K. Haenen, O. A. Williams, J. Hees, and N. B. Brookes, "Thin conductive diamond films as beam intensity monitors for soft X-ray beamlines," *Rev. Sci. Instrum.*, vol. 84, no. 3, p. 035105, 2013.
- [146] A. Kriele, O. Williams, M. Wolfer, D. Brink, W. Müller-Sebert, and C. E. Nebel, "Tuneable optical lenses from diamond thin films," *Appl. Phys. Lett.*, vol. 95, no. 3, p. 031905, 2009.
- [147] J. Riedrich-Möller, L. Kipfstuhl, C. Hepp, E. Neu, C. Pauly, F. Mücklich, A. Baur, M. Wandt, S. Wolff, M. Fischer, S. Gsell, M. Schreck, and C. Becher, "One- and two-dimensional photonic crystal microcavities in single crystal diamond," *Nat. Nanotechnol.*, vol. 7, no. 1, pp. 69–74, 2012.
- [148] G. Fragiaco, K. Reck, L. Lorenzen, and E. V. Thomsen, "Novel designs for application specific MEMS pressure sensors," *Sensors (Basel)*, vol. 10, no. 11, pp. 9541–63, 2010.
- [149] C. Pramanik, H. Saha, and U. Gangopadhyay, "Design optimization of a high performance silicon MEMS piezoresistive pressure sensor

- for biomedical applications," *J. Micromechanics Microengineering*, vol. 16, no. 10, pp. 2060–2066, 2006.
- [150] A. Yamamoto and T. Tsutsumoto, "Piezoresistive effect of CVD polycrystalline diamond films," *Diam. Relat. Mater.*, vol. 13, no. 4-8, pp. 863–866, 2004.
- [151] S. D. Janssens, S. Drijkoningen, and K. Haenen, "Ultra-thin nanocrystalline diamond membranes as pressure sensors for harsh environments," *Appl. Phys. Lett.*, vol. 104, no. 7, p. 073107, 2014.
- [152] M. Imboden, O. A. Williams, and P. Mohanty, "Observation of non-linear dissipation in piezoresistive diamond nanomechanical resonators by heterodyne down-mixing," *Nano Lett.*, vol. 13, no. 9, pp. 4014–9, 2013.
- [153] M. Liao and K. Yasuo, "Current Progress of Pressure Sensors for Harsh Environments Based on Wide-Bandgap Semiconductors," *Recent Patents Mater. Sci.*, vol. 3, no. 2, 2015.
- [154] M. Werner, O. Dorsch, and E. Obermeier, "High-temperature pressure sensor using p-type diamond piezoresistors," *Diam. Relat. Mater.*, vol. 4, no. 5-6, pp. 873–876, 1995.
- [155] A. Yamamoto, N. Nawachi, T. Tsutsumoto, and A. Terayama, "Pressure sensor using p-type polycrystalline diamond piezoresistors," *Diam. Relat. Mater.*, vol. 14, no. 3-7, pp. 657–660, 2005.
- [156] W. K. Schomburg, *Introduction to Microsystem Design*. Springer, 2015.
- [157] O. Williams, A. Kriele, J. Hees, M. Wolfer, W. Müller-Sebert, and C. Nebel, "High Young's modulus in ultra thin nanocrystalline diamond," *Chem. Phys. Lett.*, vol. 495, no. 1-3, pp. 84–89, 2010.
- [158] P. Hubík, J. Mareš, H. Kozak, A. Kromka, B. Rezek, J. Krištofik, and D. Kindl, "Transport properties of hydrogen-terminated nano-

- crystalline diamond films," *Diam. Relat. Mater.*, vol. 24, pp. 63–68, 2012.
- [159] I. Y. Koenka, Y. Kauffmann, and A. Hoffman, "Direct visualization and characterization of chemical bonding and phase composition of grain boundaries in polycrystalline diamond films by transmission electron microscopy and high resolution electron energy loss spectroscopy," *Appl. Phys. Lett.*, vol. 99, no. 20, p. 201907, 2011.
- [160] Y.-G. Lu, S. Turner, J. Verbeeck, S. D. Janssens, P. Wagner, K. Haenen, and G. Van Tendeloo, "Direct visualization of boron dopant distribution and coordination in individual chemical vapor deposition nanocrystalline B-doped diamond grains," *Appl. Phys. Lett.*, vol. 101, no. 4, p. 041907, 2012.
- [161] A. Tibrewala, E. Peiner, R. Bandorf, S. Biehl, and H. Lüthje, "Longitudinal and transversal piezoresistive effect in hydrogenated amorphous carbon films," *Thin Solid Films*, vol. 515, no. 20-21, pp. 8028–8033, 2007.
- [162] J. Y. W. Seto, "The electrical properties of polycrystalline silicon films," *J. Appl. Phys.*, vol. 46, no. 12, p. 5247, 1975.
- [163] N.-C. Lu, L. Gerzberg, and J. Meindl, "Modeling and optimization of monolithic polycrystalline silicon resistors," *IEEE Trans. Electron Devices*, vol. 28, no. 7, pp. 818–830, 1981.
- [164] X. Jiang, J. Zhao, and X. Jiang, "Mechanical and electronic properties of diamond nanowires under tensile strain from first principles," *Nanotechnology*, vol. 22, no. 40, p. 405705, 2011.
- [165] C. Nebel, B. Rezek, and A. Zrenner, "Electronic properties of the 2D-hole accumulation layer on hydrogen terminated diamond," *Diam. Relat. Mater.*, vol. 13, no. 11, pp. 2031–2036, 2004.

- [166] T. Tsakalakos, "The bulge test: A comparison of the theory and experiment for isotropic and anisotropic films," *Thin Solid Films*, vol. 75, no. 3, pp. 293–305, 1981.
- [167] M. K. Small and W. Nix, "Analysis of the accuracy of the bulge test in determining the mechanical properties of thin films," *J. Mater. Res.*, vol. 7, no. 06, pp. 1553–1563, 1992.
- [168] S. D. Janssens, S. Drijkoningen, and K. Haenen, "Large piezoresistive effect in surface conductive nanocrystalline diamond," *Appl. Phys. Lett.*, vol. 105, no. 10, p. 101601, 2014.
- [169] A. D. Smith, F. Niklaus, A. Paussa, S. Vaziri, A. C. Fischer, M. Sterner, F. Forsberg, A. Delin, D. Esseni, P. Palestri, M. Östling, and M. C. Lemme, "Electromechanical piezoresistive sensing in suspended graphene membranes," *Nano Lett.*, vol. 13, no. 7, pp. 3237–42, 2013.
- [170] W. Gajewski, P. Achatz, O. Williams, K. Haenen, E. Bustarret, M. Stutzmann, and J. Garrido, "Electronic and optical properties of boron-doped nanocrystalline diamond films," *Phys. Rev. B*, vol. 79, no. 4, pp. 1–14, 2009.
- [171] J. Davidson, D. Wur, W. Kang, D. Kinser, and D. Kerns, "Polycrystalline diamond pressure microsensor," *Diam. Relat. Mater.*, vol. 5, no. 1, pp. 86–92, 1996.
- [172] J. E. Shelby, "Viscosity and thermal expansion of lithium aluminosilicate glasses," *J. Appl. Phys.*, vol. 49, no. 12, p. 5885, 1978.
- [173] V. Nayyar, K. Ravi-Chandar, and R. Huang, "Stretch-induced stress patterns and wrinkles in hyperelastic thin sheets," *Int. J. Solids Struct.*, vol. 48, no. 25-26, pp. 3471–3483, 2011.
- [174] Y. Zhu and G. Koley, "Highly sensitive pressure sensor using Au patterned polydimethylsiloxane membrane for biosensing applications:

- Correlation of sensitivity and effective sensing range with membrane thickness," in *2013 Proc. IEEE Southeastcon*, pp. 1–6, IEEE, 2013.
- [175] T. Yoshikawa, F. Gao, V. Zuerbig, C. Giese, C. E. Nebel, O. Ambacher, and V. Lebedev, "Pinhole-free ultra-thin nanocrystalline diamond film growth via electrostatic self-assembly seeding with increased salt concentration of nanodiamond colloids," *Diam. Relat. Mater.*, vol. 63, pp. 103–107, 2016.
- [176] "APPLICATION NOTE 871, Demystifying Piezoresistive Pressure Sensors. <https://www.maximintegrated.com/en/app-notes/index.mvp/id/871>. [Accessed on: 2016-06-24]."
- [177] S. N. Demlow, R. Rechenberg, and T. Grotjohn, "The effect of substrate temperature and growth rate on the doping efficiency of single crystal boron doped diamond," *Diam. Relat. Mater.*, vol. 49, pp. 19–24, 2014.
- [178] P. Kulha, O. Babchenko, A. Kromka, M. Husak, and K. Haenen, "Design and fabrication of piezoresistive strain gauges based on nanocrystalline diamond layers," *Vacuum*, vol. 86, no. 6, pp. 689–692, 2012.
- [179] B. Abdelaziz, K. Fouad, and S. Kemouche, "The Effect of Temperature and Doping Level on the Characteristics of Piezoresistive Pressure Sensor," *J. Sens. Technol.*, vol. 04, no. 02, pp. 59–65, 2014.
- [180] D. Krishnamurti, "The Raman spectrum of diamond," *Proc. Indian Acad. Sci. - Sect. A*, vol. 40, no. 5, pp. 211–216, 1954.
- [181] "Specialty Glass Products Technical Reference Document, Borosilicate SCHOTTAF45 Alkali free Thin Glass. [https://abrisatechnologies.com/specs/SCHOTT\\_AF45\\_Spec\\_Sheet\\_072102.pdf](https://abrisatechnologies.com/specs/SCHOTT_AF45_Spec_Sheet_072102.pdf). [Accessed on: 2016-04-01]."

## BIBLIOGRAPHY

---

- [182] “Specialty Glass Products Technical Reference Document, Borosilicate Corning® Eagle2000 Thin Glass. [https://abrisatechnologies.com/specs/Corning Eagle 2000 Spec Sheet.pdf](https://abrisatechnologies.com/specs/Corning_Eagle_2000_Spec_Sheet.pdf). [Accessed on: 2016-04-01].”
- [183] “Silicon wafers. <https://www.neyco.fr/uploads/media/category/0001/03/Materials-J-Wafers-Silicium.pdf>. [Accessed on: 2016-04-01].”
- [184] L. S. Pan and D. R. Kania, eds., *Diamond: Electronic Properties and Applications*, vol. 27. Springer Science & Business Media, 2013.
- [185] Y. von Kaenel, J. Stiegler, J. Michler, and E. Blank, “Stress distribution in heteroepitaxial chemical vapor deposited diamond films,” *J. Appl. Phys.*, vol. 81, no. 1997, p. 1726, 1997.
- [186] H. Windischmann, G. F. Epps, Y. Cong, and R. W. Collins, “Intrinsic stress in diamond films prepared by microwave plasma CVD,” *J. Appl. Phys.*, vol. 69, no. 1991, pp. 2231–2237, 1991.
- [187] V. Ralchenko, A. Smolin, V. Pereverzev, E. Obraztsova, K. Korotoushenko, V. Konov, Y. Lakhotkin, and E. Loubnin, “Diamond deposition on steel with CVD tungsten intermediate layer,” *Diam. Relat. Mater.*, vol. 4, no. 5-6, pp. 754–758, 1995.
- [188] J. W. Ager and M. D. Drory, “Quantitative measurement of residual biaxial stress by Raman spectroscopy in diamond grown on a Ti alloy by chemical vapor deposition,” *Phys. Rev. B*, vol. 48, no. 4, pp. 2601–2607, 1993.
- [189] H. Vandeparre, M. Piñeirua, F. Brau, B. Roman, J. Bico, C. Gay, W. Bao, C. N. Lau, P. M. Reis, and P. Damman, “Wrinkling Hierarchy in Constrained Thin Sheets from Suspended Graphene to Curtains,” *Phys. Rev. Lett.*, vol. 106, no. 22, p. 224301, 2011.
- [190] A. Argon, V. Gupta, H. Landis, and J. Cornie, “Intrinsic toughness of interfaces,” *Mater. Sci. Eng. A*, vol. 107, pp. 41–47, 1989.



- [191] K. Lee, S. Lee, D.-Y. Khang, and T. Lee, "Wrinkling evolution of a growing bubble: the wonders of petal-like patterns in amorphous silicon membranes," *Soft Matter*, vol. 6, no. 14, p. 3249, 2010.
- [192] D. Vella, A. Ajdari, A. Vaziri, and A. Boudaoud, "Wrinkling of Pressurized Elastic Shells," *Phys. Rev. Lett.*, vol. 107, no. 17, p. 174301, 2011.
- [193] P. Bella and R. V. Kohn, "Wrinkles as the Result of Compressive Stresses in an Annular Thin Film," *Commun. Pure Appl. Math.*, vol. 67, no. 5, pp. 693–747, 2014.
- [194] Y. Yan, B. Wang, J. Yin, T. Wang, and X. Chen, "Spontaneous wrinkling pattern of a constrained thin film membrane," *Appl. Phys. A*, vol. 107, no. 4, pp. 761–767, 2012.
- [195] A. T. Collins, "Synthetic diamond: Emerging CVD science and technology. Edited by Karl E. Spear and John P. Dismukes," *Chem. Vap. Depos.*, vol. 1, no. 1, pp. 33–33, 1995.
- [196] D. Halliday, R. Resnick, and J. Walker, *Fundamentals of physics 9th edition*. John Wiley & Sons, Ltd, 2010.
- [197] G. Lombardi, X. Duten, K. Hassouni, A. Rousseau, and A. Gicquel, "Effects of Pulsed Microwave Plasmas on Diamond Deposition," *J. Electrochem. Soc.*, vol. 150, no. 5, p. C311, 2003.
- [198] P. May, J. Smith, and Y. A. Mankelevich, "Deposition of NCD films using hot filament CVD and Ar/CH<sub>4</sub>/H<sub>2</sub> gas mixtures," *Diam. Relat. Mater.*, vol. 15, no. 2-3, pp. 345–352, 2006.
- [199] M. Varga, Z. Remes, O. Babchenko, and A. Kromka, "Optical study of defects in nano-diamond films grown in linear antenna microwave plasma CVD from H<sub>2</sub>/CH<sub>4</sub>/CO<sub>2</sub> gas mixture," *Phys. Status Solidi*, vol. 249, no. 12, pp. 2635–2639, 2012.

## BIBLIOGRAPHY

---

- [200] R. Brunsteiner, R. Haubner, and B. Lux, "Hot-filament chemical vapour deposition of diamond on SiAlON at pressures up to 500 Torr," *Diam. Relat. Mater.*, vol. 2, no. 9, pp. 1263–1270, 1993.
- [201] Z. P. Lu, J. Heberlein, and E. Pfender, "Process study of thermal plasma chemical vapor deposition of diamond, part I: Substrate material, temperature, and methane concentration," *Plasma Chem. Plasma Process.*, vol. 12, no. 1, pp. 35–53, 1992.
- [202] I. Langmuir, "The dissociation of hydrogen into atoms," *J. Am. Chem. Soc.*, vol. 34, no. 7, pp. 860–877, 1912.
- [203] D. Monéger, F. Bénédic, R. Azouani, F. Chelibane, O. Syll, F. Silva, and A. Gicquel, "Deposition of nanocrystalline diamond films in pulsed Ar/H<sub>2</sub>/CH<sub>4</sub> microwave discharges," *Diam. Relat. Mater.*, vol. 16, no. 4-7, pp. 1295–1299, 2007.
- [204] W. H. Bragg and W. L. Bragg, "The Reflection of X-rays by Crystals," *Proc. R. Soc. A Math. Phys. Eng. Sci.*, vol. 88, no. 605, pp. 428–438, 1913.
- [205] W. Tang, K. Xu, P. Wang, and X. Li, "Residual stress and crystal orientation in magnetron sputtering Au films," *Mater. Lett.*, vol. 57, no. 20, pp. 3101–3106, 2003.
- [206] K. Haenen, A. Lazea, J. Barjon, J. D'Haen, N. Habka, T. Teraji, S. Koizumi, and V. Mortet, "P-doped diamond grown on (110)-textured microcrystalline diamond: growth, characterization and devices," *J. Phys. Condens. Matter*, vol. 21, no. 21, pp. 364204–10, 2009.
- [207] M. Nishitani-Gamo, K. P. Loh, I. Sakaguchi, T. Takami, I. Kusunoki, and T. Ando, "Surface morphology of homoepitaxially grown (111), (001), and (110) diamond studied by low energy electron diffraction and reflection high-energy electron diffraction," *J. Vac. Sci. Technol. A Vacuum, Surfaces, Film.*, vol. 17, no. 5, p. 2991, 1999.

- [208] P. Németh, L. A. J. Garvie, T. Aoki, N. Dubrovinskaia, L. Dubrovinsky, and P. R. Buseck, "Lonsdaleite is faulted and twinned cubic diamond and does not exist as a discrete material," *Nat. Commun.*, vol. 5, p. 5447, 2014.
- [209] K. Kang, Y. Jin, J. Kim, and P. K. Ajmera, "Study on low temperature growth and formation mechanism of hexagonal diamond," *Diam. Relat. Mater.*, vol. 27, pp. 76–81, 2012.
- [210] B. Xu and S.-I. Tanaka, "Formation of giant onion-like fullerenes under Al nanoparticles by electron irradiation," *Acta Mater.*, vol. 46, no. 15, pp. 5249–5257, 1998.
- [211] P. Badziag, W. Verwoerd, S., W. Ellis, P., N. Greiner, and R., "Nanometre-sized diamonds are more stable than graphite," *Nature*, vol. 343, no. 6255, pp. 244–245, 1990.
- [212] O. A. Shenderova, V. V. Zhirnov, and D. W. Brenner, "Carbon Nanostructures," *Crit. Rev. Solid State Mater. Sci.*, vol. 27, no. 3-4, pp. 227–356, 2002.
- [213] H. Xie, F. Yin, T. Yu, J.-T. Wang, and C. Liang, "Mechanism for direct graphite-to-diamond phase transition," *Sci. Rep.*, vol. 4, pp. 51–55, 2014.
- [214] F. Zhang, F. Ahmed, G. Holzhüter, and E. Burkel, "Growth of diamond from fullerene C60 by spark plasma sintering," *J. Cryst. Growth*, vol. 340, no. 1, pp. 1–5, 2012.
- [215] S. Bhargava, H. D. Bist, S. Sahli, M. Aslam, and H. B. Tripathi, "Diamond polytypes in the chemical vapor deposited diamond films," *Appl. Phys. Lett.*, vol. 67, no. 12, p. 1706, 1995.
- [216] M. Nishitani-Gamo, I. Sakaguchi, K. P. Loh, H. Kanda, and T. Ando, "Confocal Raman spectroscopic observation of hexagonal diamond formation from dissolved carbon in nickel under chemical vapor deposition conditions," *Appl. Phys. Lett.*, vol. 73, no. 6, p. 765, 1998.

- [217] R. Z. Khaliullin, H. Eshet, T. D. Kühne, J. Behler, and M. Parrinello, "Nucleation mechanism for the direct graphite-to-diamond phase transition," *Nat. Mater.*, vol. 10, no. 9, pp. 693–697, 2011.
- [218] J. E. Sansonetti and W. C. Martin, "Handbook of Basic Atomic Spectroscopic Data. <http://www.nist.gov/pml/data/handbook/index.cfm>. [Accessed on 2016-06-01]," 2009.
- [219] G. Suchaneck, J.-P. Mönch, K. Schade, and W. Paul, "Optical emission spectroscopy of silane/argon magnetron discharges," *J. Non. Cryst. Solids*, vol. 90, no. 1-3, pp. 323–326, 1987.
- [220] B. Strahm, A. A. Howling, and C. Hollenstein, "Plasma diagnostics as a tool for process optimization: the case of microcrystalline silicon deposition," *Plasma Phys. Control. Fusion*, vol. 49, no. 12B, pp. B411–B418, 2007.
- [221] A. Taylor, P. Ashcheulov, M. Čada, L. Fekete, P. Hubík, L. Klimša, J. Olejníček, Z. Remeš, I. Jirka, P. Janíček, E. Bedel-Pereira, J. Kopeček, J. Mistrík, and V. Mortet, "Effect of plasma composition on nanocrystalline diamond layers deposited by a microwave linear antenna plasma-enhanced chemical vapour deposition system," *Phys. status solidi*, vol. 212, no. 11, pp. 2418–2423, 2015.
- [222] A. Taylor, J. Drahokoupil, L. Fekete, L. Klimša, J. Kopeček, A. Purkrt, Z. Remeš, R. Čtvrtlík, J. Tomáščík, O. Frank, P. Janíček, J. Mistrík, and V. Mortet, "Structural, optical and mechanical properties of thin diamond and silicon carbide layers grown by low pressure microwave linear antenna plasma enhanced chemical vapour deposition," *Diam. Relat. Mater.*, vol. 69, pp. 13–18, 2016.
- [223] H. C. Barshilia, B. R. Mehta, and V. D. Vankar, "Optical emission spectroscopy during the bias-enhanced nucleation of diamond microcrystals by microwave plasma chemical vapor deposition process," *J. Mater. Res.*, vol. 11, no. 11, pp. 2852–2860, 1996.

- [224] P. Pobedinskas, G. Degutis, W. Dexters, A. Hardy, M. K. Van Bael, and K. Haenen, "Influence of hydrogen and hydrogen/methane plasmas on AlN thin films," *Appl. Phys. Lett.*, vol. 104, no. 8, p. 081917, 2014.
- [225] Y. Zhang, F. Zhang, and G. Chen, "A study on surface morphologies of diamond films," *Mater. Lett.*, vol. 20, no. 1-2, pp. 39-42, 1994.
- [226] A. Schenk, A. Tadich, M. Sear, K. M. O'Donnell, L. Ley, A. Stacey, and C. Pakes, "Formation of a silicon terminated (100) diamond surface," *Appl. Phys. Lett.*, vol. 106, no. 19, p. 191603, 2015.
- [227] M. S. Bakshi, "How Surfactants Control Crystal Growth of Nanomaterials," *Cryst. Growth Des.*, vol. 16, no. 2, pp. 1104-1133, 2016.
- [228] C. Q. Sun, H. Xie, W. Zhang, H. Ye, and P. Hing, "Preferential oxidation of diamond {111}," *J. Phys. D: Appl. Phys.*, vol. 33, no. 17, pp. 2196-2199, 2000.
- [229] Y. Tao and C. Degen, "Facile fabrication of single-crystal-diamond nanostructures with ultrahigh aspect ratio," *Adv. Mater.*, vol. 25, no. 29, pp. 3962-7, 2013.
- [230] M. Liao, S. Hishita, E. Watanabe, S. Koizumi, and Y. Koide, "Suspended single-crystal diamond nanowires for high-performance nanoelectromechanical switches," *Adv. Mater.*, vol. 22, no. 47, pp. 5393-7, 2010.